Impact of High Fidelity Battery Models for Vehicle Applications

by

William Scott

A thesis
presented to the University of Waterloo
in fulfilment of the
thesis requirement for the degree of
Master of Applied Science
in
Chemical Engineering

Waterloo, Ontario, Canada, 2015

Author's Declaration

I hereby declare that I am the sole author of this thesis. This is a true copy of the thesis, including any required final revisions, as accepted by my examiners. I understand that my thesis may be made electronically available to the public.

Abstract

Automotive battery models, compared with personal electronics, are more complex as they experience a larger range of current discharge/charge rates. Electronics have a constant power demand, and thus a constant current is demanded from the battery. Vehicles have fluctuating power demands, dependent on the acceleration rate, and thus a non-constant current is demanded. There are many different classifications of automotive battery models depending on the fidelity required.

Most automotive battery models can be attributed to one of two classifications: electrochemical and equivalent circuit, although there are some exceptions (e.g. neural network, linear, etc.). Electrochemical models incorporate individual particle interactions with great detail, resulting in high accuracy and simulation time. It follows that electrochemical models are frequently used in the design of new battery technologies. In a contrast equivalent circuit models (ECMs) simplify complex chemical interactions as circuit components consisting of limited parameters, trading model accuracy for speed and computational simplicity. Equivalent circuit models are frequently used when the battery is a component of a larger comprehensive model or when real-time convergence is essential. For this reason, equivalent circuit models are the preferred model for vehicle simulation, design, and control systems.

The internal resistance (Rint) equivalent circuit model is currently dominant within the literature. Consisting of a single parameter (R_{int}), the Rint model is easy to characterize and implement. This model is often expanded by expressing the resistance as a function of temperature and relative capacity (i.e. state of charge or SOC), as well as current direction. This model can be found in industrial vehicle modeling software such as Autonomie. However the Rint model does not capture the nature of the battery voltage response which displays a hysteresis, or time lagged, effect. This effect includes, but is not limited to, faradic charge-transfer resistance (SEI interface), double-layer capacitance, lithium-ion diffusion, or kinetic faradic impedance.

The Thevenin equivalent circuit model accounts for this effect by introducing two additional parameters, a resistor and capacitor (R_2 and C_1) in parallel, in series with the internal resistance (R_{int}). This adaptation allows the model to capture the hysteresis effect, as the voltage across the secondary resistor (R_2) is a function of the energy stored within the capacitor (C_1). It has been shown that, despite its simplicity, the Thevenin model displays a large improvement in prediction accuracy relative to the Rint model.

In this work the impact of the hysteresis effect, and need for higher fidelity battery models, is investigated. To this end, the Rint and Thevenin models are characterized with the hybrid pulse power characterization (HPPC) test scaled to the current demands exhibited in the UDDS and US06 drive cycles using a $LiFePO_4$ battery. The characterized models are then validated with the measured battery voltage response to simulated UDDS and US06 drive cycle representative current profiles. The two models are then compared across the US06, HWFET, and UDDS drive

cycles in Autonomie software. The model simulation results, expressed in terms of electrical consumption (Wh mi^{-1}), are given context with reference to 2014 commercial electrified vehicles.

Acknowledgements

I would like to thank not only those who contributed to the creation of this work, but also those who contributed to me. The first belongs to my mother Sheridan and father Chris, to whom I owe more than words can express. The second belongs to my brother Alex, to whose debt can, but I know better than to try. The third belongs to my girlfriend Keyi, where I will continue to look for words that express my devotion and support.

I would like to thank my childhood friends, Reilly, Matthew, and Eli. Know that although we may have not spoken in many years, and that we are separated by a great distance, that you will never be forgotten.

I would like to thank my distant friends, Daxter, Shion, Medeia, Domé, Atlas, and Haruka. Know that you are a constant reminder of the importance of an individual, and the person I can aspire to be.

I would like to thank my mentors, specifically Mrs. Kelly Robinson, Mr. Ferdowsian, Dr. Prilliman, and Dr. Ramsey. You taught me how to help others with what I know, which I consider the most important lesson of all.

I would like to thank my co-workers, Dylan, Caixia, Ehsan, Zhiyu, Mohammad, Momo, Manoj, and the University of Waterloo Alternative Fuels Team. This was a difficult journey, and if not for you, I would have been alone.

I would like to thank my supervisors, Dr. Fowler and Dr. Fraser. It is thanks to them that I was provided the opportunity for this work, and it would not have been possible without them.

Dedication

This work is dedicated to Dr. Rob Whitely. You will forever be a role model for me.

Contents

List of Figures

List of Tables

List of Abbreviations

AER	All Electric Range
ANOVA	Analysis of Variance
BEV	Battery Electric Vehicle
BMU/S	Battery Management Unit/System
CID	Charge Interrupt Device
CPE	Constant Phase Element
DOD	Depth of Discharge, %
DOE	Department of Energy
DP	Dual Polarization
DPW	Dual Polarization with Warburg
ECM	Equivalent Circuit Model
EIS	Electrochemical Impedance Spectroscopy
EPA	Environmental Protection Agency
EREV	Extended Range Electric Vehicle
ESMAT	Electronically Shifted Manual Transmission
ESS	Energy Storage System
EV	Electrified Vehicle
FCEV	Fuel Cell Electric Vehicle
FCP	Fuel Consumption Program
FCVT	Freedom Car and Vehicle Technologies
FTP	Federal Test Procedure
GUI	Graphical User Interface
GM	General/Government Motors
GRG	Generalized Reduced Gradient
HEV	Hybrid Electric Vehicle
HPPC	Hybrid Pulse Power Characterization
HWFET	Highway Fuel Economy Test
ICE	Internal Combustion Engine
IEC	International Electrochemical Commission
Li-ion	Lithium-Ion
LFP	Lithium Iron Phosphate
MPG	Miles per Gallon
MPG_e	Miles per Gallon Equivalent
NASA	National Aeronautics and Space Administration
NSF	National Science Foundation
NYCC	New York City Cycle
OEM	Original Equipment Manufacturers
PHEV	Plug-in Hybrid Electric Vehicle
PNGV	Partnership for a New Generation of Vehicles
PSAT	Powertrain Systems Analysis Toolkit
PTC	Positive Temperature Coefficient
R|C	Resistor and Capacitor in parallel
SAFT	Société des Accumulateurs Fixes et de Traction
SC03	SFTP representing engine load and emissions associated with the use of air conditioning
SEI	Solid Electrolyte Interface
SFTP	Supplemental Federal Test Procedure
SLI	Starting Lighting and Ignition
SOC	State of Charge, %
SOH	State of Health, %
UDDS	Urban Dynamometer/Domestic Driving Schedule
US06	SFTP representing engine load and emissions associated with high acceleration
VPC	Vehicle Propulsion Controller

Nomenclature

i	Current, Amps
i_0	Initial current, Amps
i_1	Total current entering the equivalent circuit, Amps
i_2	Current across the resistor in the R|C element, Amps
i_3	Current across the capacitor in the R|C element, Amps
i_3’	i_3 at the previous reference state, Amps
Measured	Time relative measured voltage, Volts
Modeled	Time relative modeled voltage, Volts
SOC	Relative capacity, %
ΔSOC	Change in relative capacity, %
t	Time, seconds
t_0	Initial time, seconds
t_1	Time at the present reference state, seconds
t_2	Time at the previous reference state, seconds
Δt	Difference in time between two referenced states, seconds
V_1	Voltage across the equivalent circuit model initial resistor element, Volts
V_2	Voltage across the equivalent circuit model resistor within the R|C element, Volts
V_3	Voltage across the equivalent circuit model capacitor within the R|C element, Volts
V_3’	V_3 at the previous time reference state, Volts
V_{circ}	Voltage across the equivalent circuit, Volts
V_{OC}	Open circuit voltage, Volts
$V_{measured}$	Measured voltage of the lithium-ion battery, Volts
V_{model}	Model predicted voltage of the lithium-ion battery, Volts

1 Introduction

This work discusses the importance of modeling the hysteresis effect within equivalent circuit models (ECM) for lithium-ion batteries used within electrified vehicles. This section details governmental influence (s. 1.1.1), fuel economy and energy loss (s. 1.1.2), lithium ion batteries (s. 1.2), types of battery models (s. 1.3), and vehicle simulation software (s. 1.4). A significant portion of this section simply provides "background" information prevalent to those interested in the industry, and while not required to implement this research, it is necessary to understand the implications, scope, and methodology.

The experimental procedure (s. 2) includes: measuring battery voltage response (s. 2.1) which details equipment and the HPPC and drive cycle test procedures; parameter characterization (s. 2.2), which details the parameterizing or "fitting" methods of the Rint or Thevenin equivalent circuit models to the HPPC test measured voltage response; and model validation (s. 2.3), which details the validation of the fitted models by reproduction of simulated drive cycle voltage responses. The remaining sections, which discuss vehicle simulation results (s. 3), electrical efficiency of 2014 commercial vehicles (s. 4), impact on vehicle design (s. 5), and concluding remarks (s. 6) detail the importance of modeling the hysteresis effect when designing an electrified vehicle. Additionally there are recommendations (s. 7) for researchers who wish to continue this work to a broader scope.

The objective of this work is to determine the impact of high accuracy battery models within the scope of vehicle modeling software. It focuses on battery voltage drop and varying resistance profiles, which influence effective range and discharge/charge efficiency. To quantify these effects the Thevenin equivalent circuit model, a high fidelity model, and the Rint equivalent circuit model, a low fidelity model, were characterized using a lithium iron phosphate (LFP) cell. These models were then imported into comprehensive vehicle modeling software to determine the impact of improved battery model accuracy.

1.1 The Next Generation of Vehicles

Increasing economic, environmental, and political pressures drive the development for more efficient vehicles. Whereas reduced fuel cost is inherently desirable to the consumer (s. 1.1.2), localized pollution and energy security are predominately governmental concerns (s. 1.1.1). Automotive manufacturers have developed battery electric (BEV), hybrid electric (HEV), and plug-in hybrid electric (PHEV) vehicles to improve fuel economy and curb greenhouse gas emissions by reallocating a portion of the petroleum energy demand to the electrical grid.

1.1.1 Governmental Influence

Governments are promoting more efficient vehicle development to reduce pollution and dependence on foreign oil. Local governments tend to offer rebates, vouchers, or perks to

consumers with the purchase of an electric or hybrid vehicle (e.g. Ontario, CA [1]; Quebec, CA [2]; British Columbia, CA [3]; California, USA [4]) however this can also extend to federal governments (e.g. China [5], UK [6]). These subsidies are in the range of 3,500 to 7,500 U.S. dollars and benefits may include free electrical charging and priority access to parking and roads. Some federal governments (e.g. Germany [7]) prioritize research over subsidies. The United States, the largest adopter of electric vehicles, has been a leader in the new generation of vehicle design [8].

1.1.1.1 Partnership for the New Generation of Vehicles

In 1993, eight U.S. government agencies and three major automotive corporations launched The Partnership for the New Generation of Vehicles (PNGV), a cooperative research program concerning the advancement of the automotive industry. The program end goal was "to conceive, develop, and implement new technologies of significantly reducing the fuel consumption and carbon dioxide emissions of the U.S. automobile fleet" which is often referenced as "increasing the fuel efficiency of existing vehicles to 80 mpg, without sacrificing size, utility, cost of ownership, or customer appeal" by 2003 [9]. The agencies and corporations involved in PNGV were the U.S. Department of Commerce, Energy, Defense, Interior, Transportation, the National Science Foundation (NSF), the National Aeronautics and Space Administration (NASA), the Environmental Protection Agency (EPA), General Motors (GM), Ford Motor Company (Ford), and Daimler Chrysler (Chrysler) respectively [10]. The program was cancelled in 2001 at the request of automakers, where it was replaced by the FreedomCAR program.

The program is considered a success with the production of three vehicles which demonstrated the technical feasibility of the efficiency requirement: the Chrysler Dodge ESX3 (72 mpg), Ford Prodigy (72 mpg), and the General Motors Precept (80 mpg). Program engineering developments include, decreasing drag coefficients and vehicle weight, incorporating regenerative breaking technology, improving engine efficiency, utilizing diesel engines, improving automatic transmission efficiency, and fuel cell production cost reduction [10] [11].

1.1.1.2 FreedomCAR and Vehicle Technologies

After PNGV was decommissioned in 2001, it was replaced by with the FreedomCAR and Vehicle Technologies (FCVT) program which focused on hydrogen based fuel alternatives and plug-in hybrid electric vehicles (PHEV). FCVT was met with opposition, as it was funded by allocating resources from other energy minded programs [12]. In 2010, the Department of Energy (DOE) reduced funding for FCVT emphasizing that it will allocate funds "to technologies with more immediate promise," suggesting that adoption of lithium-ion batteries should predate fuel cell research [13].

1.1.1.3 Vehicle Comparison and Drive Cycles

It is desired by manufactures and consumers to compare vehicle performance. Because vehicle performance is not constant (e.g. engine efficiency, transient effects, etc.), it is impossible to

relate data between vehicles without predetermined standards. These standards, often referred to as “drive schedules” or “drive cycles,” are vehicle speed vs. time relationships that represent expected driver behavior.

The dominate standards within the United States and Canada are the UDDS (Urban Dynamometer Driving Schedule) and HWFET (Highway Fuel Economy Test) drive cycles. These tests are used to determine the effective gas efficiency recorded on the EPA label (Figure 1, Table 1 [14]) which is required on all new vehicles as of May 2011 [15]. Test results may also be reviewed online at fueleconomy.gov [16].

The EPA produces these ratings based on a weighted average of two drive schedules (UDDS and HWFET) performed at a regulated facility in Ann Arbor, Detroit USA. The EPA performs the tests using 48” single roll dynamometers for light duty vehicles and trucks. The dynamometers are set to the equivalent test weight, defined as the curb weight plus 300 lbs. which represents the weight of the driver and one passenger [17]. The dynamometer simulates wind and rolling resistance through drag coefficients reported by the production company determined by SAE practices Road Load Measurement Using Onboard Anemometry and Coastdown Techniques (J1263 & J2263) and Chassis Dynamometer Simulation of Road Load Using Coastdown Techniques (J2264) with the addition of a guidance letter [18]. In addition to the vehicle performance, other parameters of interest such as battery size, curb weight, and all electric range are also included in the EPA report.

Transport Canada’s Fuel Consumption Program (FCP) independently verifies Canadian automotive manufacturer vehicles using the US federal test procedures (FTP). The tests are functionally similar to those of the EPA, and involve mounting the automobile on a weighted dynamometer with reference to vehicle aerodynamic drag, curb weight, and rolling resistance. A trained driver then runs the vehicle through driving cycles that simulate trips within the city and highway [19].

Figure 1: Example of EPA label [14]

Table 1: EPA label details [14]

#	Name	Description
1	Vehicle Technology and Fuel	Describes vehicle type and fuel options • Diesel • Compressed Natural Gas • Hydrogen Fuel Cell • Flexible Fuel: Gasoline-Ethanol (E85) • Plug-in Hybrid: Electricity-Gasoline • Electric
2	Fuel Economy	Combined fuel economy is a weighted average of the city (UDDS, 55%) and highway (HWFET, 45%) drive schezdules
3	Comparative Fuel Economy	Compares this vehicles fuel economy with others in its class (e.g. SUV, lightweight truck, station wagon, etc.)
4	Estimated Savings Compared to Avg.	Estimated fuel cost savings when compared to the average vehicle of the same make for that year, calculated on a 15,000 miles/year and $3.70/gal of gasoline basis
5	Fuel Consumption Rate	Fuel efficiency in terms of consumption (gal per 100 miles) rather than economy (miles per gallon)
6	Estimated Annual Fuel Cost	Projected annual fuel cost on a 15,000 miles/year and $3,70/gal of gasoline basis
7	Fuel Economy/Greenhouse Gas Rating	Gasoline vehicles share the same rating for fuel economy and greenhouse gas emissions (carbon dioxide emitted is directly linked to fuel consumed), on a metric of 1 to 10
8	CO_2 Emission Information	Amount of CO_2 emitted per mile (tailpipe only)
9	Smog Rating	Rating for tailpipe emissions related to the production of smog and other local air pollution (e.g. nitrogen oxide, carbon monoxide, formaldehyde, etc.), a metric of 1 to 10
10	Fine Print	Reminder that mpg is a factor of driving conditions and technique
11	QR Code	Smart phone integration for additional information
12	Website Link	Directs to a website with vehicle comparison information and energy saving techniques (e.g. local gas prices, driving strategies, etc.)

Care should be taken when comparing vehicles solely on their fuel economy (i.e. mpg) as, although a standardized and required metric, it can be misleading. For example, consider the fuel required for a 10 and a 15 mpg vehicle to travel 1,000 miles. The 10 and 15 mpg vehicles will require 100 and 66 gallons of fuel, respectively for a net difference of 33 gallons. However on the traditional mpg or "economy" scale, the difference is only 5 miles per gallon (Figure 2) [14]. The amount of fuel required to transverse a fixed distance increases exponentially as fuel economy decreases.

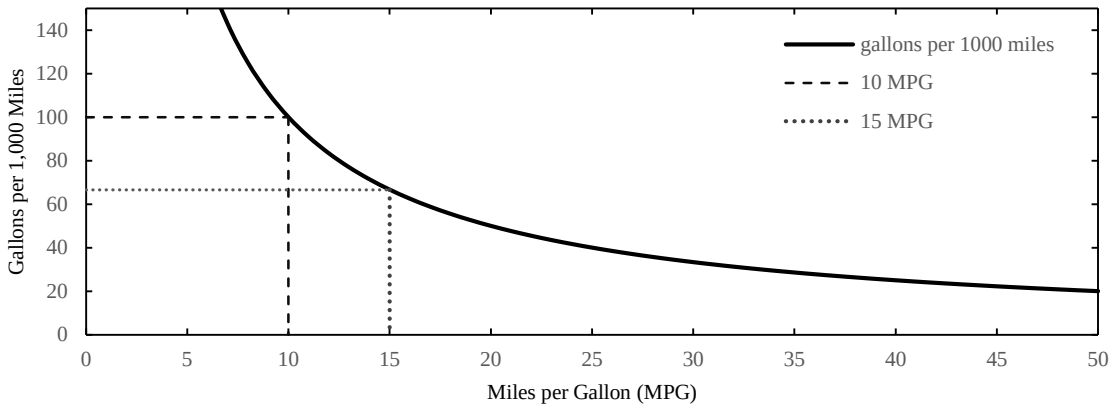

Figure 2: "MPG illusion," gallons/1000 miles vs. miles/gallon

While the EPA label mentions two drive cycles, there are many others. These cycles aim to compare other aspects of the vehicle, such as the efficiency while using accessories such as air conditioning (SC03) or during low speed stop-and-go traffic conditions (NYCC). UDDS and HWFET remain dominate with US06 as a possible addition, which is described as a "high acceleration and aggressive" driving schedule. The trace speed and time correlation for these cycles (UDDS, HWFET, and US06) are shown in Figure 3 through Figure 5 respectively [20].

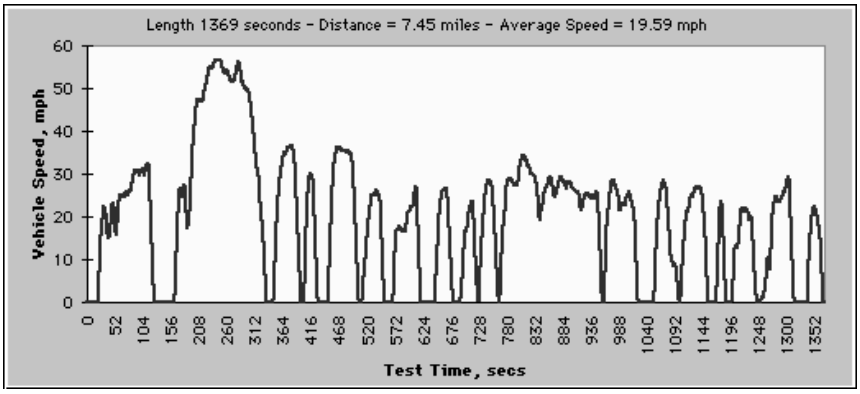

Figure 3: UDDS drive schedule [20]

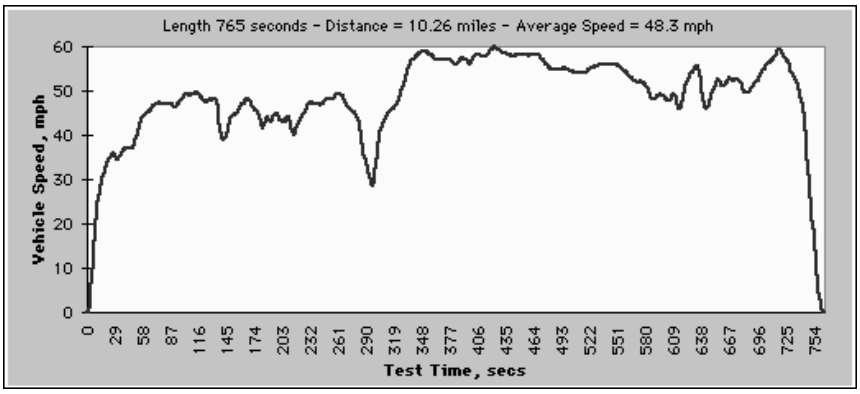

Figure 4: HWFET drive schedule [20]

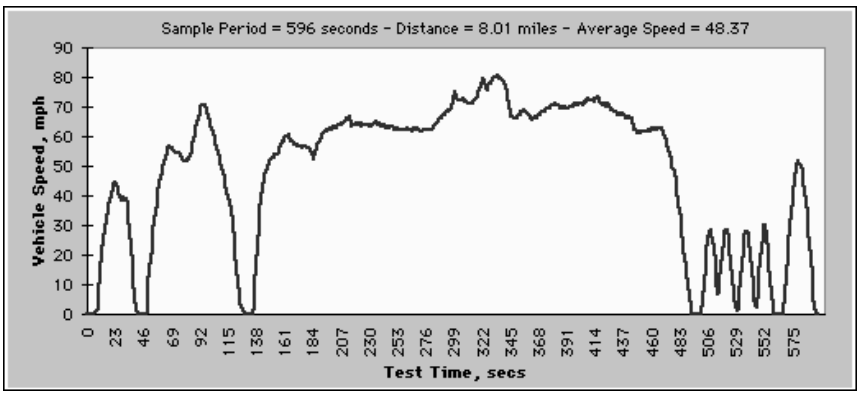

Figure 5: US06 drive schedule [20]

1.1.2 Fuel Economy and Energy Loss

Fuel economy and energy loss are directly correlated: as energy loss decreases, fuel economy increases. While there have been attempts of negating external losses, the majority of development involves improving the vehicle power train [10] [21] [22]. New technologies such as plug-in hybrid (PHEV), hybrid (HEV), battery (BEV), and fuel cell (FCEV) electric vehicles are capable of drastically increasing power train efficiencies, and consequently, vehicle fuel economy (Figure 6) [23].

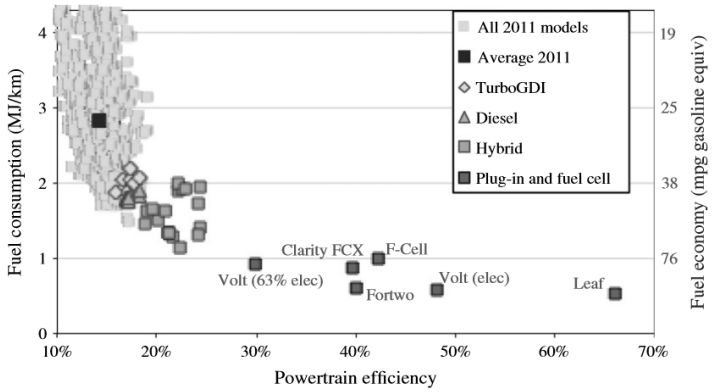

Figure 6: Vehicle fuel consumption, economy, and power train efficiency of 2011 models [23]

This increased efficiency is limited to domestic or city driving (Figure 7) [23], which can be attributed to *regenerative breaking* and *idle-off* technology (Vehicle Electrification, s. 1.1.2.3). Thus internal combustion engine (ICE) vehicles compete relatively well with electric architecture vehicles in highway applications, where these technologies see limited use.

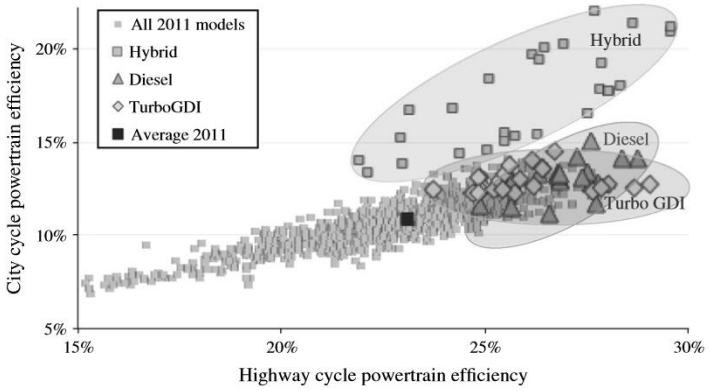

Figure 7: City and highway powertrain efficiency of 2011 models [23]

In an ICE vehicle used for urban driving, approximately 13% of the fuel is used for vehicle propulsion. Energy losses occur within the engine and drivetrain (e.g. waste heat, vibration, mechanical losses, etc.) are known as internal loads (Figure 8) [24]. Additional that losses occur when outside forces oppose vehicle motion (e.g. aerodynamic drag, rolling resistance, etc.) are known as external loads. These values can further decrease by using energy consuming accessories (e.g. air conditioning, heating, and lighting) which are known as parasitic loads [21].

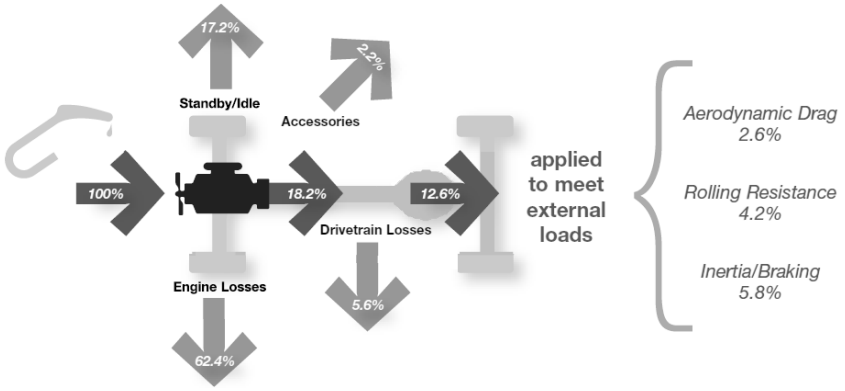

Figure 8: Expected internal combustion engine energy losses within urban driving [24]

Increasing energy efficiency can be viewed as removing these energy losses. In this mindset, the supplied fuel represents 100% of the total energy available with each conversion impairing this value. Therefore to increase energy efficiency it is imperative to remove, or recover, energy losses. Some of these losses can be reduced or recovered by vehicle electrification. These losses, specifically the engine and transmission, will be discussed before transitioning to vehicle electrification.

1.1.2.1 Engine Efficiency

ICEs are relatively inefficient at converting chemical potential energy into mechanical work, as most of the energy produced from fuel combustion is in the form of heat. Excess heat must be removed to protect the mechanical stability of the engine, and facilitates additional energy loss (e.g. engine cooling systems). This energy loss is approximately 63% on average for domestic driving [24], but net engine efficiency is speed and torque dependent (Figure 9) [25]. Traditionally, the highest yields are obtained in the 1,500 to 3,500 rpm range [26].

While a heat gradient is potentially a valuable energy resource, there are few options for capturing, storing, or recovering this energy in the form of useful work [21]. Waste heat can, however, be discharged to the cabin in cold environments alleviating the need to exert additional resources for passenger temperature control.

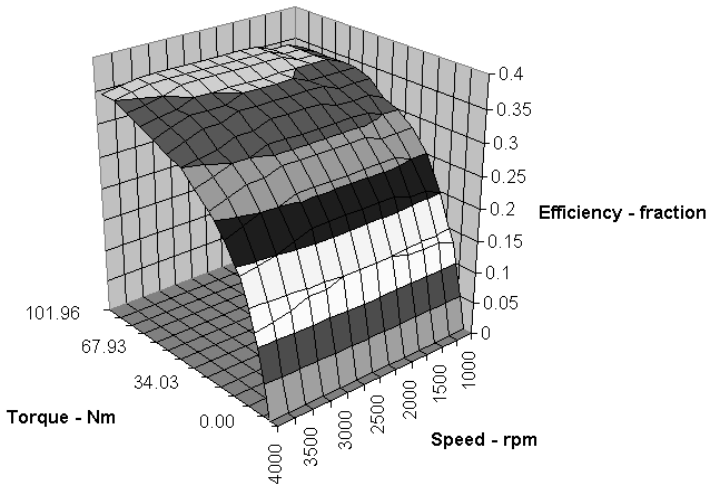

Figure 9: Example of a traditional engine efficiency map [25]

Idling, or engine standby, presents an additional energy loss. To clarify, while the vehicle remains stationary at an intersection or during congested traffic, the engine continues to consume fuel in order to sustain parasitic loads and to be able to meet post-standby energy demands. The necessity of standby, combined with heat generation, compose the majority of ICE energy losses [21].

1.1.2.2 Transmission Efficiency

As previously mentioned, engine efficiency is dependent on engine speed and torque (Figure 9). A transmission facilitates engine operation within its maximum efficiency range. To do this, it acts as a translator between the crankshaft (engine) and driveshaft (wheels) relating speed and power by a series of gears. Small and large gears are used for high (e.g. accelerating from rest, inclines) and low (e.g. cruising speed) power applications respectively. Although the transmission allows the engine to operate more efficiently, there are mechanical losses associated with its operation. These mechanical losses account for approximately 5.6% of energy produced in ICE vehicles [21].

There are two types of transmission systems, manual and automatic. Manual transmissions are controlled by the driver through a "stick shift," which is in direct contact with the transmission through a clutch. To shift between gears, the driver disengages the engine from the transmission via the clutch, makes the shift, then re-engages the transmission to bring power back to the driveshaft. Automatic transmissions shift gears without driver intervention through a fluid-coupling device known as a torque converter. Automatics tend to be less efficient than manual transmissions because they contain fewer gears (which allow the engine to operate in its most efficient region more frequently), are heavier, and produce an additional energy loss within the torque converter (fluid inertia).

Electronically shifted manual transmissions (ESMAT) are identical in operation to manual transmissions, with the exception that an onboard computer controls the instrumentation instead of the driver. Shift 'points' can be preprogrammed for power or fuel efficiency. ESMAT and other forms of computer aided transmission can approach the benefits of full manual, or approximately a 5% reduction in fuel consumption [21].

1.1.2.3 Vehicle Electrification

In conventional vehicles, many important subsystems are powered by the crankshaft. These include oil and coolant pumps, power steering and breaking, as well as air conditioning. Each of these parasitic subsystems is attached to the crankshaft, and consumes additional energy. However, even when not in use, their connection to the crankshaft is not 100% efficient which results in energy loss. This loss can be minimalized by connecting this load to the battery instead of the crankshaft as electrical devices utilize energy more efficiently (i.e. they require less energy to run and do not require energy while not in use). The amount of electrification, or electricity dependent loads, a vehicle can support is dependent on battery size. For example, 12 and 42 volt batteries can support power steering and air conditioning respectively [21].

Moving to higher power electric architecture provides more opportunities for fuel saving systems. Increased electric power can support technologies such as *idle-off* and *launch assist*, which provide increased fuel economy [27]. *Idle-off* suspends engine activity during breaking and standby, preserving fuel during otherwise idle operation. Increased electrical power can support a motor, which allows the vehicle to accelerate immediately from an idle position – without the need to wait for the engine to restart [21].

These features require electrical power to run, which must be supplied by the battery. The battery thus must be recharged when excess energy permits. This energy, provided in part by the engine, can also be acquired through *regenerative breaking* [27]. While in regenerative breaking mode, when the break is applied, the vehicle uses the electric motor in reverse to reduce speed. This functions as a generator, which produces energy allowing for the battery to be recharged. Electrification of vehicle architecture is the design principle of battery and hybrid electric vehicles [21].

1.1.2.3.1 Hybrid Vehicle Drivetrains

Hybrid electric vehicles (HEVs) are defined as vehicles that utilize an on board motor, powered by a battery, to aid the engine [28]. In a restrained definition, hybrids are limited to *regenerative breaking*, *idle-off*, *launch assist*, and reduction of parasitic loads. However, with an increased power supply (e.g. larger or more advanced battery pack) the electric motor can provide additional support to the engine. With the engine and motor working together in concert, the engine can operate within its efficient region more frequently (Figure 10) [29]. Additionally, the extra power provided by the motor allows the engine to be downsized, reducing vehicle weight and increasing fuel economy.

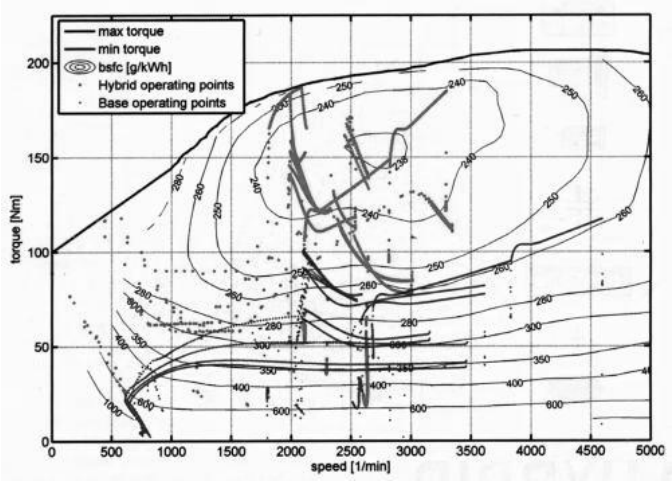

Figure 10: Hybrid and traditional engine efficiency map comparison [29]

Furthermore, with high motor efficiencies (80% or higher) [30], it becomes enticing to utilize engine to support the motor, rather than the opposite. This lends to a distinction regarding the "degree" of hybridization, ranging from mild to strong. A "mild" hybrid uses a motor for *regenerative breaking*, *idle-off*, and *launch assist* only, whereas a "strong" hybrid uses the motor to supplement or replace the engine powertrain in addition to these benefits. This observation lead to multiple vehicle architectures, or powertrains, with varying methods of supplying power to the crankshaft. Some of these architectures are discussed below, notably parallel, series, and power-split.

1.1.2.3.1.1 Parallel Architecture

In parallel architecture (Figure 11), the motor and engine can power the wheels independently or simultaneously through a coupled drive shaft. The location of this coupling varies, and can be located before or after the transmission, depending on the original equipment manufacturer (OEM) design. This architecture can be seen in the Honda Civic, GM Saturn Vue and Aura Green Line, and Volkswagen Golf [21].

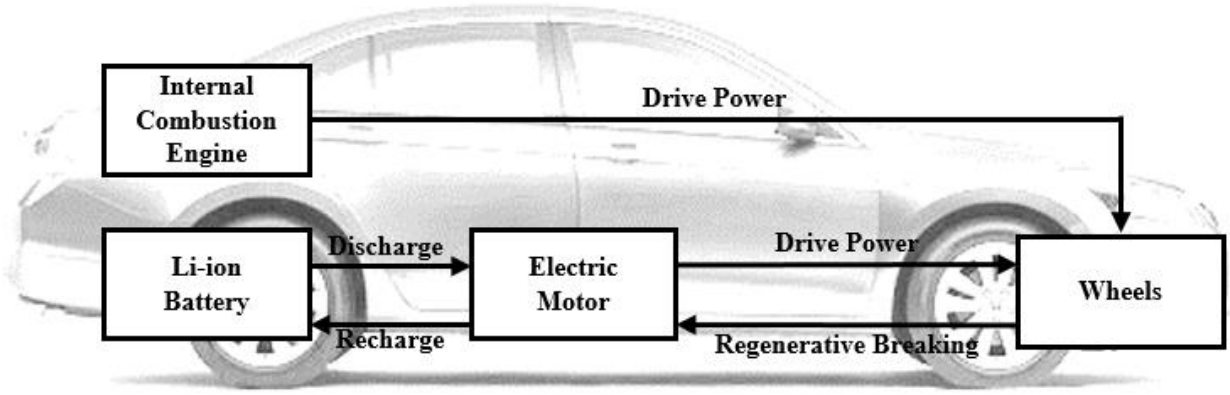

Figure 11: Parallel architecture

1.1.2.3.1.2 Series Architecture

In series architecture (Figure 12), the wheels are powered entirely by the electric motor. The engine exists solely to fuel an onboard generator to recharge the battery pack, and runs as needed independently of the drivetrain. This architecture can be seen in the GM EV1 or Fisker Karma [31].

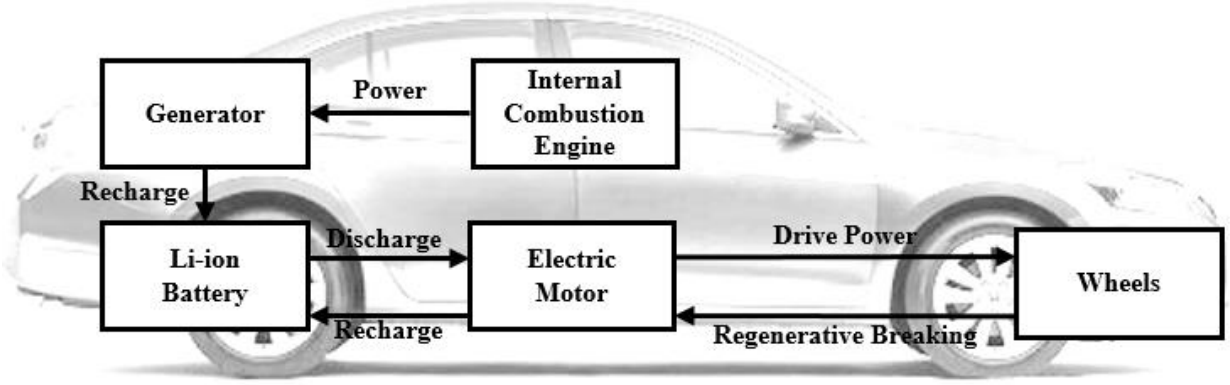

Figure 12: Series architecture

1.1.2.3.1.3 Series-Parallel Architecture

Series-parallel is a combination of the previous two architectures (Figure 13). As seen in the series architecture, the engine can power an onboard generator for recharging the battery pack. Additionally, as in the parallel architecture, the engine can power the wheels directly independently or with the electric motor. This architecture is permitted by the use of a planetary gear system, which connects the engine and motor(s). This architecture can be seen in the Ford C-Max Energi, Fusion, Escape, and Mariner; Toyota Prius and Camry; GM Chevrolet Tahoe, Volt, Cadillac ELR, and Sierra; Mitsubishi Outlander; BYD F3DM; Honda Accord; and Audi A3 E-Tron [21].

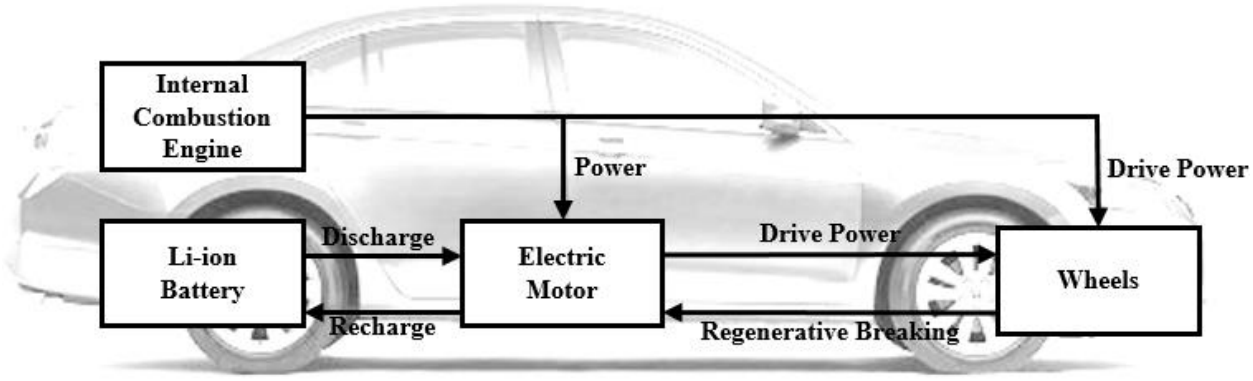

Figure 13: Series-parallel architecture

1.1.2.4 Origin of Plug-in Hybrid Electric Vehicles

As propulsion with a motor is considerably more efficient than the engine it is reasonable to operate in these conditions for as long as possible. Motor operation is limited by the battery pack capacity, therefore, increasing the size of the battery pack will increase motor use and improve vehicle efficiency. This is the logic that created plug-in hybrid electric vehicles (PHEV), vehicles with high capacity batteries that are recharged between journeys.

PHEVs utilize two different types of fuel, and capture benefits of each. They provide an efficiency rivaling that of an electric vehicle by use of the motor, although hampered by the weight of the engine and related components. However, once the battery capacity has been depleted, the vehicle functions identically to a traditional HEV using the engine to produce additional range. The battery pack capacity is sufficiently large such that the engine powertrain supplements motor operation. For this reason, PHEVs are sometimes referred to as extended range electric vehicles (EREV) placing additional emphasis on the battery and related components.

This emphasis extends to terminology involving engine and motor powertrain interactions. For example, *charge depleting* (CD) mode refers to depleting battery capacity by using the motor powertrain. Similarly, *charge sustaining* (CS) and mode refers to maintaining battery capacity at a set point with the assistance of the engine.

Additional terminology exists in the form of *all-electric* and *blended* modes. In *all-electric* mode, the battery is depleted exclusively by operation of the motor powertrain. *Blended* mode refers to operation of both the engine and motor powertrains.

1.1.2.5 Electrified Vehicle Electrical Efficiency

As electrified vehicles utilize different fuels than internal combustion engine vehicles, it is useful to introduce a metric for comparison. The Department of Energy in combination with the Environmental Protection Agency have produced such a metric, and equates one gallon of gasoline to 33.7 kWh of electricity. For electrified vehicles, the rating mpg_e, indicative of miles

per gallon equivalent, is substituted for mpg on required publications and references (Vehicle Comparison and Drive Cycles, s. 1.1.1.3).

The EPA provides an energy/distance metric which can be useful for vehicle comparison, e.g. 27 kWh 100 mi^{-1}. Alternative units are sometimes used, e.g. 3.7 mi kWh^{-1}, for their similarity with the conventional metric mpg.

1.1.2.6 All Electric Range

A concern regarding electrified vehicles is their all-electric range (AER), defined as the distance the vehicle can travel utilizing the on board battery. For BEVs, AER is synonymous with the effective range of the vehicle. For PHEVs, AER denotes the maximum distance the vehicle can travel before an alternative resource, typically gasoline, is required.

1.1.2.7 Energy Density

Although electrified power trains are more efficient in conversion of chemical to kinetic energy than their traditional counterparts, there are complications with energy storage. The medium for electric energy storage is non-standardized, Mercedes, BMW, Mitsubishi, Renault / Nissan, and Tesla are fully invested in batteries whereas Hyundai and Toyota are exploring fuel cell alternatives [32].

While batteries have been used in automobiles since their introduction in the form of lead-acid or starting-lighting-ignition (SLI) batteries, new material compositions can increase their energy density (i.e. energy stored per unit mass or volume). The first commercial electrified vehicles, such as the Toyota Prius, initially used nickel-metal hydride batteries. However most automakers have since adopted lithium-ion technology [33]. This appears to be the dominant chemistry for battery-type energy storage (Figure 14), and is a vast improvement over lead-acid batteries [34]. The referenced chemistries in Figure 14, left to right, are lead – hydro sulfuric acid, nickel – cadmium, nickel – metal hydride, lithium – ion, plastic lithium – ion, and lithium – metal.

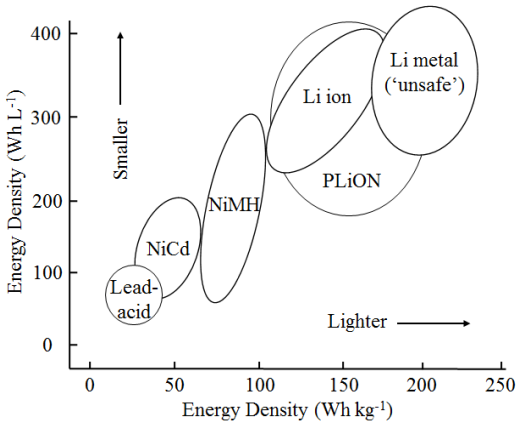

Figure 14: Energy density of competing battery technologies [34]

However, battery energy density is orders of magnitude smaller than conventional fuels: gasoline and diesel (Figure 15) [35]. While the majority of this energy cannot be converted into useful work (Engine Efficiency, s. 1.1.2.1), conventional vehicles stand to benefit from this energy density dissimilarity. In addition to a larger range, conventional vehicles can be smaller and lighter than their electrified equivalents due to their increased energy density.

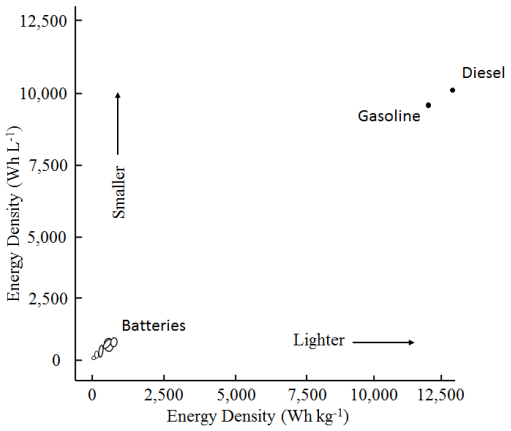

Figure 15: Energy density of batteries relative to gasoline and diesel

1.2 Batteries

The term lithium-ion (Li-ion) battery refers to an entire family of battery chemistries. However, these chemistries are an active area of research, and new materials are being constantly developed. This work aims to provide an overview, rather than a comprehensive report, of battery designs and components (s. 1.2.1), how lithium-ion cells operate (s. 1.2.2), and pack architecture (s. 1.2.3).

1.2.1 Cell Design

Cell architecture is determined by the internal electrode structure. If the anode and cathode are stacked in alternating layers, the cell structure is known as "prismatic" – typically used for machinery and hybrid/battery powered electric vehicles (Figure 17). Alternatively, if the electrodes are wound in a 'jelly roll' configuration it is known as "cylindrical" – typically used in laptops, cameras, and other commercial electronics (Figure 16) [36] [37].

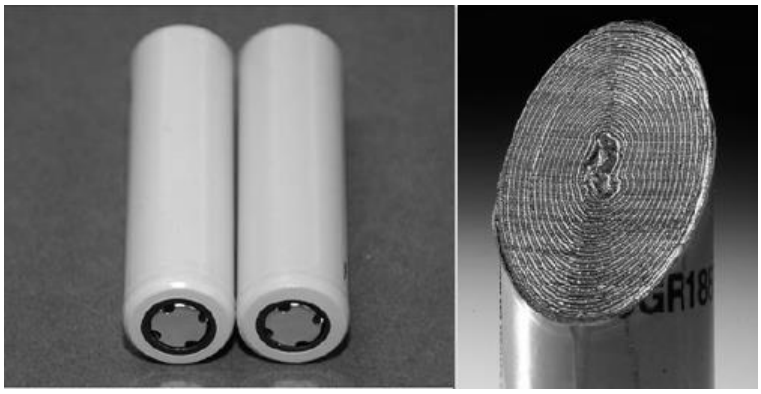

Figure 16: Example of 18650 cylindrical cells (left) and "jelly roll" winding (right) [36] [37]

The cells are enclosed in a protective casing to isolate and protect them from the working environment. Enclosures can be grouped into two sections, hard and soft. Hard enclosures employ laser-welded or gasket-fitted metal exteriors, whereas soft enclosures are heat-sealed foil pouches (Figure 17) [36]. Hard enclosures are used when the cell is directly exposed to the working environment (Casing, s. 1.2.1.3.1). Soft, or pouch, enclosures are used when the cell is protected by the installation device (e.g. cell phones, laptops), or when provided the protection of a battery pack enclosure (Battery Pack Architecture, s. 1.2.3).

Figure 17: Examples of prismatic cell hard case (left) and pouch (right) [36]

The International Electrochemical Commission (IEC) Standard 61960 designates nomenclature for most battery cells. For cylindrical cells, the first two digits define the cell diameter in millimeters and the next three define the length in tenths of millimeters (e.g. an 18650 cell is 18 mm in diameter and 65.0 mm in length). For prismatic cells, the six digit code is separated into 3 sections of 2 digits: the first representing height in tenths of millimeters and the following pair representing width and length in millimeters (e.g. a 305050 cell is 3.0 x 50 x 50 mm). It should be noted that the IEC nomenclature concerns only the external dimensions, not the chemistry, of a cell [38].

1.2.1.1 Components and Materials

A battery is composed of primary and secondary components. Primary components are necessary for the cell to function, and comprise of the basic electrical elements. Secondary components increase the durability and safety of a cell by enhancing the mechanical resilience of the battery or by providing protection against abnormal pressure, temperature, and abuse.

1.2.1.2 Primary Components

The three functional components of a lithium ion cell consist of the electrodes, electrolyte, and separator.

1.2.1.2.1 Electrodes

A cell contains two types of electrodes, positive and negative, which are referred to as the cathode and anode respectively. Both electrodes are composed of a metal current collector coated with a thin layer of a conductivity enhancing compound applied with a binder, although the materials of construction of the anode and cathode differ.

Electrode material of construction has a direct effect on battery characteristics. Electrode variation historically occurs within the cathode, whereas the anode is traditionally composed of graphite. Battery manufacturers weigh the benefits of cost, specific power, performance, lifespan, and safety during battery design (Figure 18) [39].

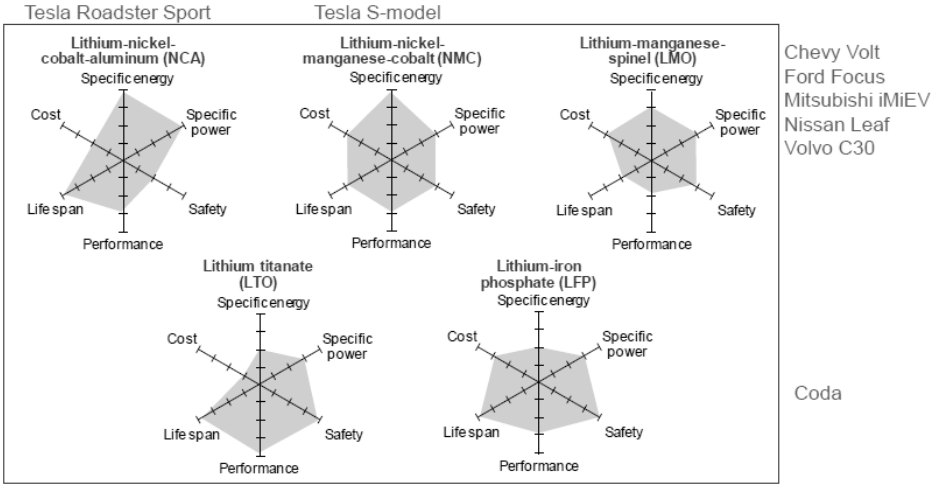

Figure 18: Comparison of lithium-ion battery chemistry performance parameters [39]

1.2.1.2.1.1 Anode

The most common material is carbon, usually graphite. The carbon can vary considerably: source (natural or synthetic), purity, particle size and distribution, particle shape and porosity, degree of compaction, etc. Although non-graphite have been produced and tested, they are rarely implemented [36]. Tests regarding anode material specific capacity and energy density are shown in Figure 19 [40]. Besenhard et al. discusses the expectations and shortcomings of these anode materials with respect to particle size [41].

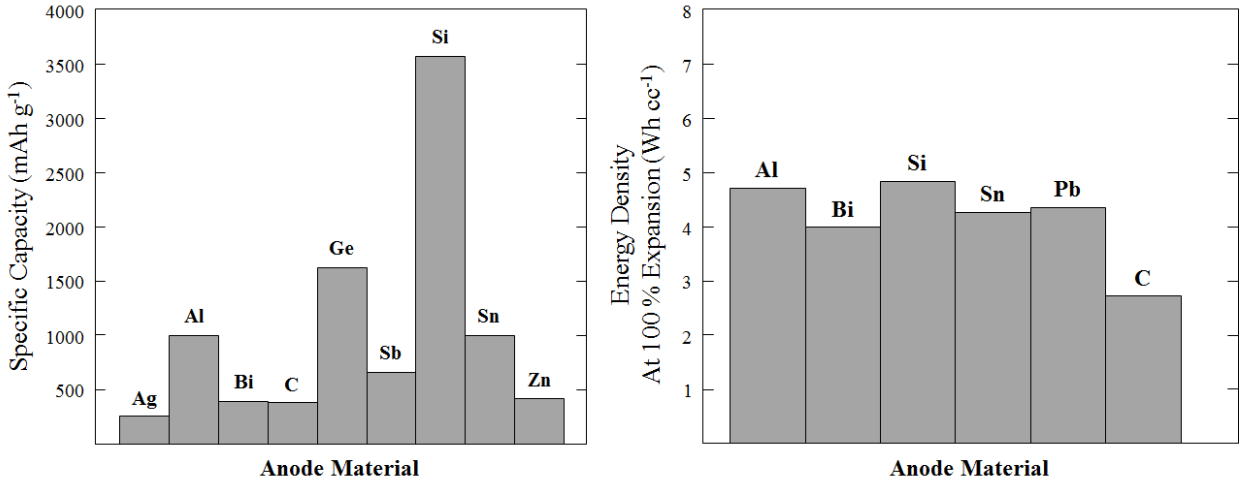

Figure 19: Anode material vs. specific capacity (left) and energy density (right) [40]

1.2.1.2.1.2 Cathode

The most common cathode material is lithium cobalt oxide, or "cobalt oxide". Additionally, other materials include $LiFePO_4$, $LiMn_2O_4$, and mixed metal oxides including Co, Ni, and Al (e.g. $LiNi_{1/3}Mn_{1/3}Co_{1/3}O_2$). Like the anode, the purity, particles, shape, etc. can vary [36].

1.2.1.2.1.3 Current Collectors

Current collectors transfer current to the active material, provide mechanical support, and provide a point of connection for leads into the cell. The most common current collectors are copper (anode) and aluminum (cathode).

Copper current collectors pose a safety concern at low cell voltages. At a voltage of approximately 1 V, the copper begins to oxidize creating copper ions which diffuse into the electrolyte. Upon charging, the ions react with the electrode surface to form a sheet of copper metal – reducing permeability, making the cell susceptible to lithium plating, and capacity loss [36].

1.2.1.2.2 Electrolyte

The electrolyte is typically a mixture of organic carbonates, lithium salts, and additives. The organic carbonate mixture composition can be varied to provide different cell properties (e.g. viscosity, thermal stability, etc.). Lithium salts provide solvated lithium-ions, most commonly lithium hexafluorophosphate ($LiPF_6$). Additives may be added to improve performance characteristics (e.g. overcharge resistance, cycle life, calendar life, etc.) and may include gelling agents which can increase cell stability (e.g. mitigate effects of pouch puncture, physically bind the electrodes together). The influence of electrolyte additives with regards to cell capacity and lifetime is discussed by Dahn et al. [42].

1.2.1.2.3 Solid Electrolyte Interface

An important observation is the addition of the solid electrolyte interface, or SEI, layer produced by an undesirable side reaction between the electrolyte and anode (Figure 20). The mixture of organic carbonates (electrolyte) and lithiated carbon (electrodes) is exothermic and produces the SEI layer (C-H, C-O, CH_2, C=O, CO_3, CF_2), CO_2 and gas (Table 2) [43]. The formation of the SEI layer is temperature dependent, and follows Arrhenius behavior.

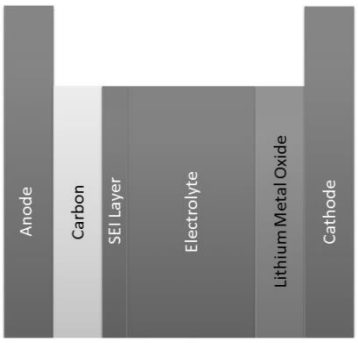

Figure 20: SEI layer formation

The SEI layer inhibits ionic transfer. Cell performance decreases with SEI formation, which acts as internal impedance (diminishing capacity and increased heat generation). Although the SEI layer inhibits performance, it disables layer expansion by blocking the electrolyte – electrode interface. For this reason, in addition to prevent potentially flammable gas emissions, producers cycle the cells to create a stable and uniform SEI layer after assembly. This significantly reduces SEI formation during commercial operation.

Table 2: Gas composition of punctured cells [44]

Cell Type	**Fresh Cell at 100% SOC**	**Aged Cell at 100% SOC**
Max Sample Temperature	25 °C	45 °C
Gas Species	**Volume Percent**	
H_2	8.2%	0.3%
Argon	44.0%	27.8%
N_2	6.2%	9.6%
O_2	0.1%	1.7%
CO	4.2%	11.3%
CO_2	12.6%	26.3%
CH_4	13.5%	11.5%
C_2H_4	3.1%	None Detected
Propane	None Detected	0.06%
Electrolyte Solvent (EC/EMC mixture)	11.2%	11.5%

1.2.1.2.4 Separator

The separator inhibits contact between the positive and negative electrodes, preventing a short circuit. Separators are porous to ionic transfer, through which the electrolyte is free flowing. Separators are typically 20 µm thick (10 – 40 µm range) and are commonly composed of polyethylene and/or polypropylene films [36].

Separators are a necessary component of battery cells because of their safety characteristics; however they do not contribute to cell performance. One method of increasing battery capacity is to select a smaller separator, allowing for more electrode material. However, safety is endangered by this method as thinner separators are more susceptible to damage and prone to failure.

Separators may also function as a safety mechanism in the event of cell failure; including shutdown and local separators. A shutdown separator decreases porosity at elevated temperatures (130 – 150 °C), impeding ionic transport and preventing charge/discharge of the cell (Figure 21, left). Upon cooling, the pores reopen allowing ionic transport to resume. A local separator selectively disables a cell in the event of an internal short by melting the pores (Figure 21, right & Figure 22) in the event of abnormal temperature increase (130 °C). This control method is irreversible, and will destroy the cell to prevent thermal runaway [36].

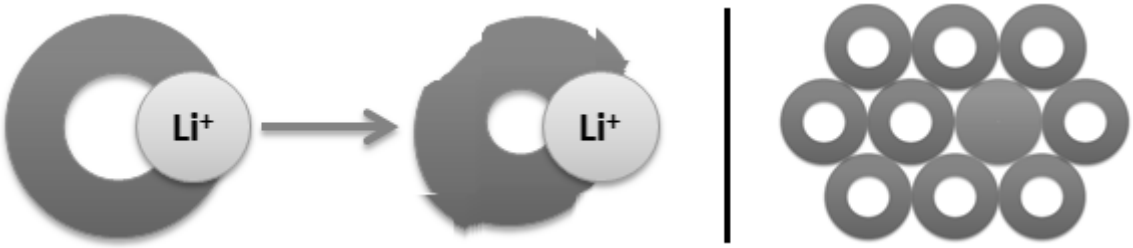

Figure 21: Shutdown separator (left) and local separator (right) mechanics

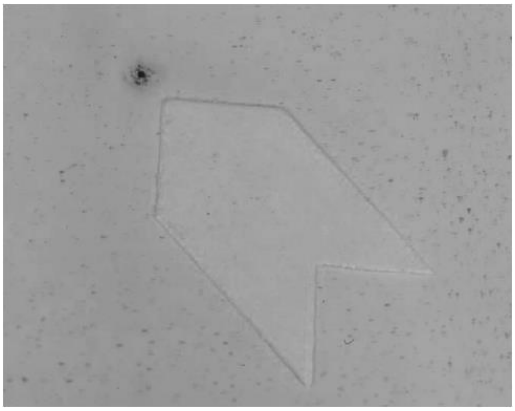

Figure 22: Photograph of a local separator operation [36]

1.2.1.3 Secondary Components

The secondary components which protect the cell from abuse consist of: casing, which impede mechanical damage; pressure controls, which inhibit overpressure; temperature controls, which prevent high excess heat; and battery monitoring circuitry, which avert overcharge/discharge.

1.2.1.3.1 Casing

Hard case cells are composed of metal (e.g. nickel coated – steel or aluminum). Generally the case functions as one of the electrodes: the anode for nickel coated – steel (18650 cells) and cathode for aluminum (many prismatic cells) casing respectively. Because the case is polarized, shrink wrap is used to provide electrical isolation. To maximize mechanical stability, designers use a single seam to contain the cell. Cylindrical cells are often sealed with a gasket, whereas prismatic cells utilize laser welding (Figure 23) [36].

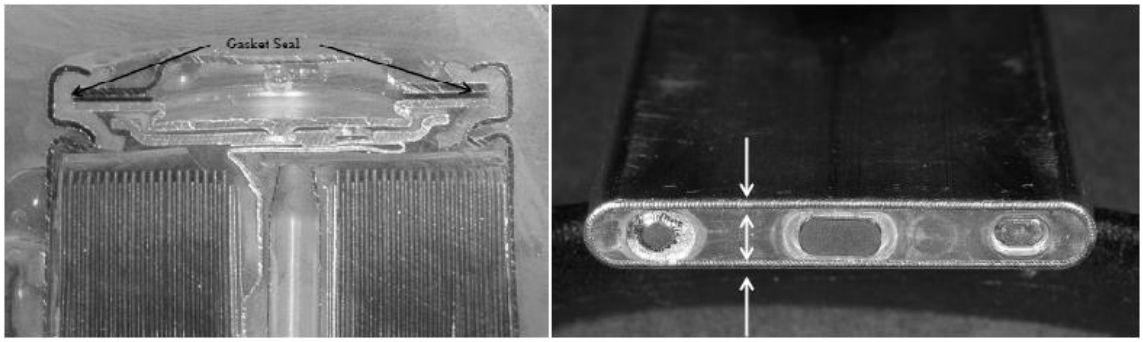

Figure 23: Gasket seal (left) and laser weld (right) [36]

Soft pouch cells (also referred to as pouch, polymer, and Li-Po cells) are enclosed in polymer coated aluminum foil. Pouches are not as durable as their hard case counterparts, but are smaller and lighter in comparison and rely on the host device for protection. The casing is electrically neutral, and all connections must attach to leads protruding outside the pouch.

1.2.1.3.2 Pressure Relief Devices

Pressure relief devices provide a safety mechanism in the event a cell becomes over pressurized (e.g. during thermal runaway). Relief devices vary, including rupture disks (common in cylindrical cells), score marks (common in prismatic cells), or weld strength. These devices provide a predetermined 'weak point' for controlled pressure relief, a safer alternative to pressure buildup and involuntary release. Soft cells do not utilize relief devices, as the seams are prone to fail at relatively low temperatures and pressures.

1.2.1.3.3 Pressure Equalizing Tubing

Under normal operation, pressure along the cell is normalized by the open core. However, during thermal runaway, high temperature and pressure can cause the core to collapse – isolating sections of the cell. These isolated sections are unable to relieve their excess pressure through venting, and pressure will continue to build until gasket seal failure. Upon gasket failure, the cell contents are ejected from the cell as the pressure is relieved (Figure 24, left).

However, stiff tubing may be implemented which preserves the open core. This prevents pressure build up by providing a pressure equalizing pathway to the relief vents, averting ejection of cell components into the environment (Figure 24, right).

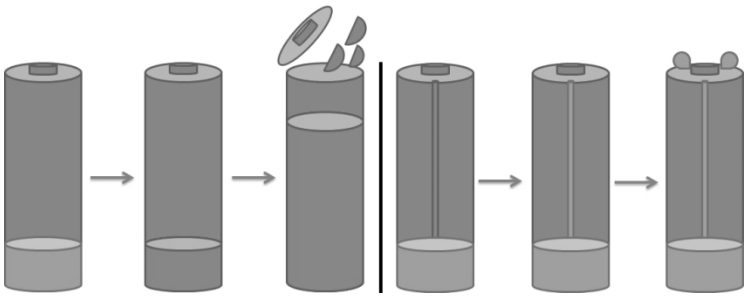

Figure 24: Overpressure of cylindrical cell (left), over pressure of cylindrical cell with relief tubing (right)

1.2.1.3.4 Positive Temperature Coefficient Devices

Positive temperature coefficient (PTC) devices, resettable thermistor devices, or "polyswitches" consist of an electrical material that becomes very resistive above a threshold temperature (Figure 25). Unlike charge interrupt devices (CIDs), PTC devices are reversible, and the resistance will decrease when the temperature resumes normal operating range.

1.2.1.3.5 Charge Interrupt Devices

Charge interrupt devices (CIDs) physically and irreversibly sever the cell from the electrical circuit when the cell pressure exceeds a threshold value (Figure 25). Although CIDs are described as overcharge protection devices, activation could be caused by overcharge, over discharge, overheating, electrolyte breakdown, or internal short-circuit. CIDs are not recommended for large parallel arrays of cells as it is unlikely that they will activate simultaneously, rather a cascade will disable individual cells, causing high current to be applied to cells where the CID has not yet activated. This application of high current may drive a cell to thermal runaway before CID activation [36] [45].

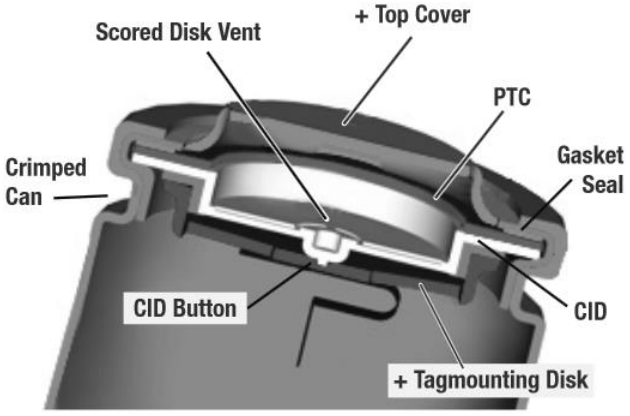

Figure 25: Location of CID and PTC on cylindrical cell [45]

1.2.1.3.6 Pack Protection Electronics

Battery management units (BMUs) monitor the battery and provide additional protection from voltage/current overcharge, external short circuit, charging/discharging outside a given

temperature range, and imbalance protection (Table 3). In electric vehicles, the battery pack electronics are often referred to as the battery management system (BMS) [36].

Table 3: Abuse scenarios prevented by BMU

Abuse scenario	Result	Prevention Technique
Over voltage overcharge Over current overcharge	Excess heat generation of cells	Disable charge
Over discharge	Damage current collectors and electrodes, increased risk of thermal runaway	Disable discharge, "low power sleep mode"
External short circuit	Massive heat generation, possible thermal runaway	Disable battery
Operation outside temperature range	Increased risk of gas generation, swelling, trigger of CID or thermal runaway	Disable battery
Battery pack imbalance (non-uniform aging)	Divergent cell capacities, which can lead to overcharge/discharge	Internally short cells to maintain constant capacity. Permanently disable pack if severe imbalance

1.2.2 Cell Operation

The fundamental lithium-ion battery is a battery where the negative (anode) and positive (cathode) materials serve as hosts for lithium-ion transport. During discharge, ions move from the anode, through the electrolyte, before being intercalated into the cathode (Figure 26). Electrons, in the form of current, unable to travel through the electrolyte are discharged from the battery and return through the positive terminal. The reverse actions (ion and electron movement) occur during charging.

In a lithium-ion cell, alternating cathode/anode layers are separated by a porous film (separator). An electrolyte composed of an organic solvent and dissolved lithium salt provides the media for lithium transport.

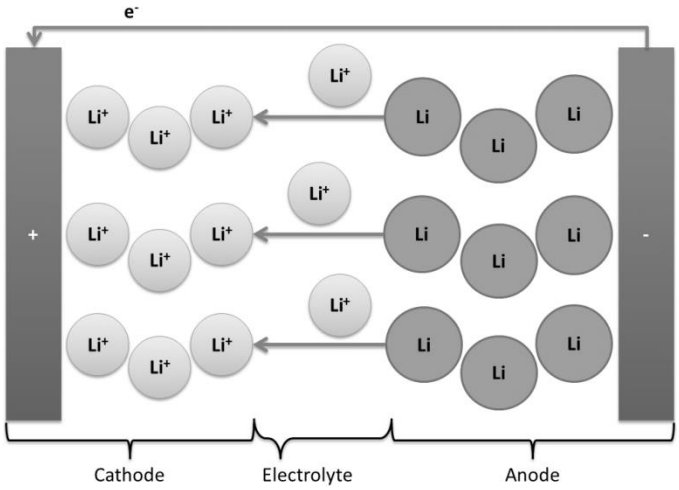

Figure 26: Lithium ion cell operation during discharge

The cell operational voltage range is determined by the cell chemistry. Most commercial lithium-ion cells have voltage ranges of 2.8 V (discharged) to 4.2 V (charged) [36]. Because of a "flat" discharge profile, the nominal voltage of a Li-ion cell is relatively constant (typically 3.6 – 3.7 V) (Figure 27) [36] [46]. Over charging or discharging (charge/discharge above/below the manufacturer's limits) can cause degradation of the electrodes, which can potentially lead to cell

failure and thermal runaway. For this reason, overcharge/discharge prevention devices are included in electronic protection packages for battery packs (Pack Protection Electronics, s. 1.2.1.3.6).

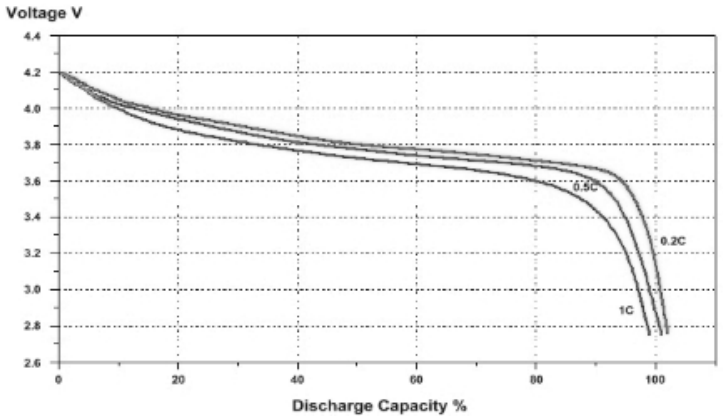

Figure 27: Discharge profile of a typical Li-ion cell [46]

1.2.3 Battery Pack Architecture

A lithium-ion battery is composed of one or more individual cells packaged with protection electronics (Figure 28) [36]. Battery pack designers can increase battery capacity and voltage by connecting cells in parallel and series respectively (Figure 29). Most battery packs are labeled with a nominal voltage (V) and capacity (Ah) that can be used to infer the number of series and parallel elements. United Nations regulations require that a battery pack be labeled in terms of Watt hours (Wh), defined as the cell nominal voltage multiplied by the rated capacity.

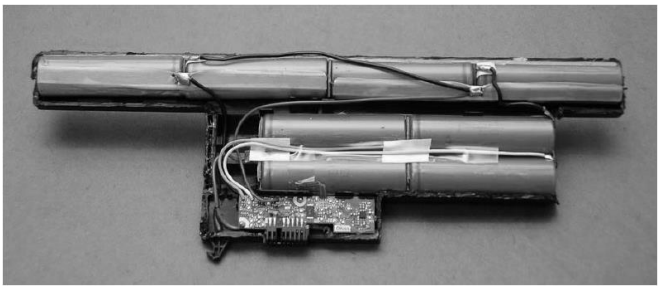

Figure 28: Example of laptop Li-ion battery pack packaged with protection electronics [36]

For example, the battery pack above (Figure 28) contains two series of four cells in parallel. The inferred voltage and capacity of the battery pack are 14.4 V (3.6 V x 4) and 4.4 Ah (2.2 Ah x 2) respectively. Alternatively, the battery pack is rated for 63.4 Wh (14.4 V x 4.4 Ah).

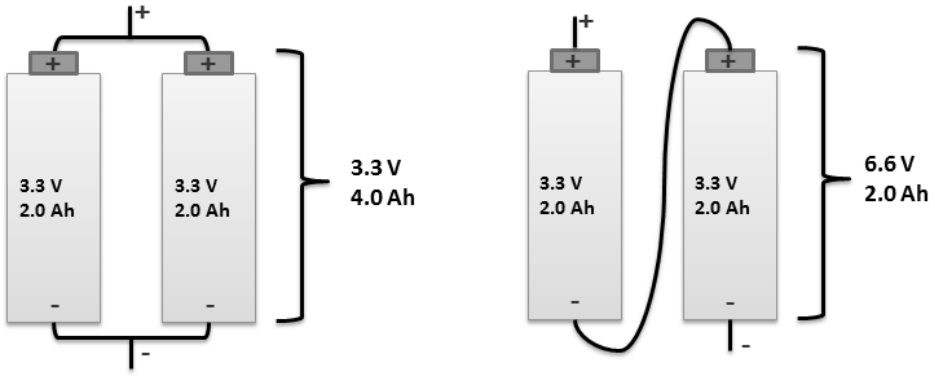

Figure 29: Schemes of cells connected in parallel (left) and series (right)

1.3 Battery Models

The main opposition to widespread adoption of electrified vehicle architecture is a financial one. The addition of an electrical drivetrain adds four to sixteen thousand U.S. dollars to the final vehicle price [47] [48]. Up to 81% of this expenditure originates from the battery pack [48]. Intuitively, in order to increase the adoption of electrified vehicles, battery costs must become smaller.

As with other vehicle components, models are a great asset in hardware selection and design [49]. Most battery models can be classified into two groups, electrochemical and equivalent circuit [50]. Equivalent circuit models (ECM) are relatively simple empirical models which represent the battery as electrical components [51] and require limited processing power [52]. For this reason, ECMs are used for battery simulation within vehicle models [49]. Electrochemical models are rigorous mathematical models which account for multiple physics-based phenomena. These high fidelity, but complex, models are limited to battery design applications due to processing power and simulation time requirements. The battery models discussed here are predominantly ECMs, however an overview of competing models is included for context.

1.3.1 Equivalent Circuit Models

ECMs estimate the battery voltage (V_{model}) as the difference between the open circuit (V_{OC}) and equivalent circuit (V_{circ}) voltages (Eq. 1), where V_{OC} is a function of SOC and temperature and V_{circ} is determined by the equivalent circuit. For a given battery, circuit parameters are functions of SOC, State of Health (SOH), and temperature [53].

$$V_{model} = V_{oc} - V_{circ} \quad \text{(Eq. 1)}$$

The simplest ECM is the internal resistance, or "Rint," model (Figure 30). This model consists of a single parameter R_1, from which V_{circ} is linearly defined with reference to the applied current (i_1) (Eq. 2) [54]. In this fashion, the model estimates the battery voltage response as the open circuit voltage with a current dependent offset.

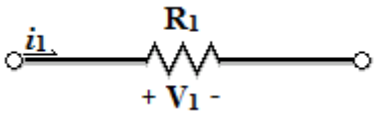

Figure 30: Internal resistance ("Rint") model

$$V_{circ\ (Rint)} = V_1 = i_1 R_1 \quad \text{(Eq. 2)}$$

The Department of Energy (DOE) utilizes a modified Rint model for plug-in hybrid electric vehicle (PHEV) battery testing (Figure 31) [54]. This modification uses a different resistance for charge and discharge currents by use of perfect diodes.

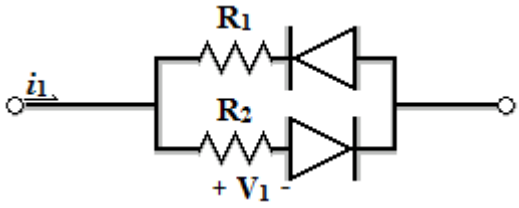

Figure 31: Expanded Rint model

The DOE proposes the hybrid pulse power characterization (HPPC) test for parameterization of the Rint model (i.e. R_1 & R_2). This test consists of three components: a 10 s constant current discharge pulse, a 40 s rest period, and a 10 s constant current charge pulse. The typical measured voltage response, Rint model prediction, and HPPC applied current is shown in Figure 32. Additional information regarding the HPPC test can be found in HPPC Test Procedure, s. 2.1.2.

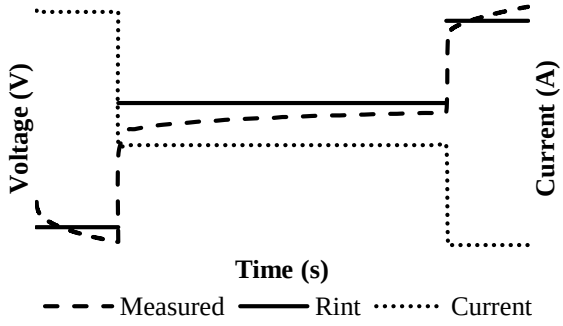

Figure 32: HPPC Rint model linear voltage response

The voltage response is shown to have a hysteresis effect [55], or time lagged response, at constant current (Figure 32). The Rint model cannot capture this phenomenon and minimizes error by assuming an average value during discharge/charge. During the rest period, error gradually decreases as the battery voltage resumes V_{OC}.

Other equivalent circuit models build upon the Rint model by adding additional circuit components, attempting to capture the hysteresis effect. A common component is the "R|C pair"

or a resistor and capacitor in parallel, as seen in the Thevenin model (Figure 33). Similar to the Rint model, V_1 is defined by R_1 and the applied current. Dissimilar to the Rint model, the current across R_2 is dependent on the applied current and the energy stored within the capacitor, C_1 (Eq. 3). The charging/discharging of the capacitor provides a time dependent voltage response.

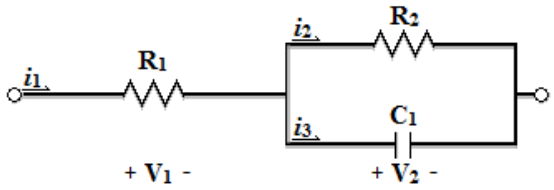

Figure 33: Thevenin equivalent circuit model

$$V_{circ\ (Thevenin)} = V_1 + V_2 = i_1R_1 + i_2R_2 \quad \text{(Eq. 3)}$$

While a single R|C component is capable of modeling the hysteresis effect, the hysteresis effect appears to be induced by multiple independent phenomena [53]. The Dual Polarization (DP) model (Figure 34), isolates "fast" and "slow" hysteresis with an additional R|C element, resulting in increased accuracy. Additional R|C elements may be added in series to further separate speeds, but provides limited improvement [56].

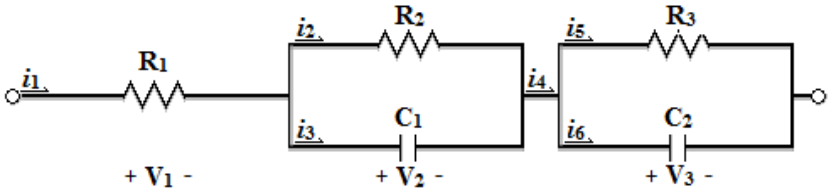

Figure 34: Dual Polarization equivalent circuit model

$$V_{circ\ (DP)} = V_1 + V_2 + V_3 = i_1R_1 + i_2R_2 + i_3R_3 \quad \text{(Eq. 4)}$$

The "true" equivalent circuit of the cell is often considered to be the Dual Polarization with Warburg (DPW) model (Figure 35), although its presented form is inconsistent in literature. The capacitors are interchangeable with constant phase elements (CPE) [57], additionally the location of the Warburg element may shift from replacing C_2 in the DP model (shown [58]) to in series with existing components [59]. Regardless of its position, ECMs which include a resistor in series with at least one R|C pair and include a Warburg element are collectively referred to as "DPW" models.

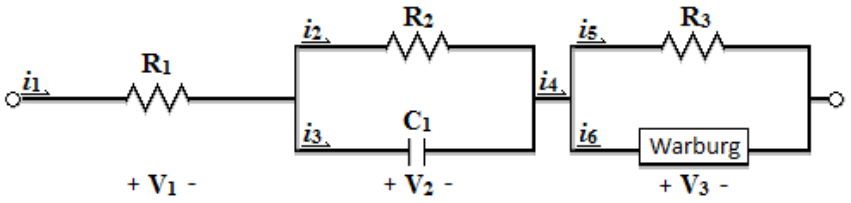

Figure 35: Dual Polarization with Warburg equivalent circuit model

$$V_{circ\ (DPW)} = V_1 + V_2 + V_3 = i_1R_1 + i_2R_2 + i_3R_3 \quad \text{(Eq. 5)}$$

Other models include the SAFT and PNGV circuits. The SAFT battery model, often referred to as the RC model, has seen results through Advisor software and is composed of three resistors and two capacitors (i.e. R_1-[R_2-C_2]|[R_3|C_3]) [60]. The Partnership for the New Generation of Vehicles (PNGV) model adds a capacitor in series to the Thevenin model (i.e. R_1-C_1-R_2|C_2) [53].

Equivalent circuit model parameters may also be characterized by alternating current through electrochemical impedance spectroscopy (EIS) tests. Circuit components derived through EIS are often attributed to electrochemical phenomena. Within the DPW model: R_1 corresponds to the bulk resistance, or conductivity of the electrolyte, separator, and electrode; R_2|C_1 corresponds to faradic charge-transfer resistance (SEI interface) and double-layer capacitance; and R_4|Warburg element corresponds to lithium ion diffusion, or faradic impedance relating to kinetics [61] [62] [63] [64] [65]. These relationships are often accompanied by a Nyquist plot (Figure 36): where R_1, R_2, R_3, and W relate to the initial gap, first semi-circle, second semi-circle, and "tail" respectively [61].

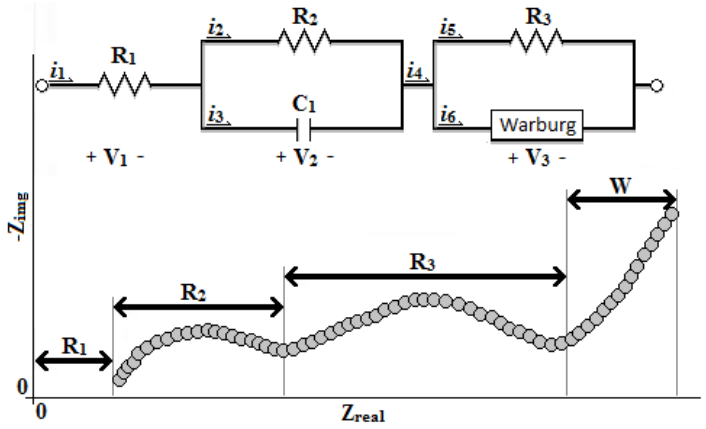

Figure 36: DPW model components correlated with EIS results [61]

1.3.2 Electrochemical Models

The first electrochemical modeling approach to porous electrodes with battery applications was presented by Newman and Tiedemann in 1975 [66]. In the porous electrode theory, the electrode is treated as a superposition between the electrolytic solution and solid matrix, the matrix itself is modeled as microscopic spherical particles where lithium ions diffuse and react on the sphere

surface. This approach was expanded to include two composite models and a separator by Fuller et al. in 1994 [67]. In order to account for electrode porosity, a micro-macroscopic model was presented by Wang et al. in 1998 [68]. This model was later adapted for Ni-MH batteries [69], and then lithium-ion batteries [70]. Further expansions include accounting for capacity decay [71] and porosity changes [72] in 2004.

Recently, there has been increased effort to use electrochemical models to estimate lithium-ion battery SOC [73]. These attempts evolve from the model introduced by Smith et al. [74], or a simplified model introduced by Haran et al. [75], and typically include a Kahman filter to estimate an average value of the bulk solid concentration. The primary application of electrochemical models is to predict physical phenomena, such as cell degradation [76] [77] [78] [79]. Due to model complexity, and thus simulation time, electrochemical models are limited to research rather than real-time applications.

Recent contributions of the University of Waterloo electrochemical modeling group include: Mathematical Modeling of Commercial LiFePO4 Electrodes Based on Variable Solid-State Diffusivity [80], a mathematical physics based model with respect to variable solid state diffusivity, particle simulation, and diffusion; Full-Range Simulation of a Commercial LiFePO4 Electrode Accounting for Bulk and Surface Effects: A Comparative Analysis [81]; which added porous electrode theory, diffusion limitation, and particle contact resistance to the previous work; Simulations of lithium iron phosphate lithiation/delithiation: Limitations of the core-shell model [82], examines the core shell model and exposes inconsistency with observed physical effects and unnecessary mathematical complexity; Simplified electrochemical multi-particle model for LiFePO4 cathodes in lithium-ion batteries [83], introduces a simplified multi-particle model; Mesoscopic modeling of Li insertion in phase-separating electrode materials: application to lithium iron phosphate [84], introduces mesoscopic or many-unit modeling which highlights interaction between lithiating units; and Model-Based Prediction of Composition of an Unknown Blended Lithium-Ion Battery Cathode [85], which relates cell characteristics to cathode composition.

1.3.3 Other Models

Other battery models include neural networks and linear models. Neural networks are complex computer generated and operated models which are limited to a ‘trained’ data set. Linear models are applicable to limited applications but are computationally simple.

1.3.3.1 Artificial Neural Network

Neural networks establish relationships between input and output data of any kind and have been developed for lithium-ion batteries [86] [87]. While neural networks are historically accurate, their accuracy is burdened by a large number of required parameters, complex formulae, and calculation time. Additionally, neural networks are estimation limited within the trained data range, severely limiting immediate applications.

1.3.3.2 Linear Models

A linear relationship has been established relating the previous SOC value, intermediate electrical measurements, and SOC variation for lead acid batteries [88] and is imposed that a similar relationship may be applied to other battery chemistries [89]. These models were developed for photovoltaic applications (i.e. low current and small SOC gradients), and are not suited for vehicles (i.e. high current and large SOC gradients).

SOC is often determined by ampere, or coulomb, counting. Remaining capacity directly corresponds to the amount of current withdrawn or supplied. Thus if an initial starting point and maximum capacity are known, and a reliable method of measuring current into/out of the cell exists, then the SOC of the cell can be estimated. As batteries are non-ideal, another term accounting for inefficiencies or losses is frequently included. An example of an ampere counting technique is detailed in Eq. 6.

$$SOC = SOC_0 + \frac{1}{C_N}\int_{t_0}^{t}(I_{batt} - I_{loss})dt \quad \text{(Eq. 6)}$$

Where C_N is the cell capacity, I_{batt} is the battery current, and I_{loss} is the current consumed by loss reactions. Error is associated with lost or 'missing' current, thus precise current measurement and inefficiency accountability are essential for model accuracy. While precise measurements can be achieved with enhanced equipment, there are multiple approaches for approximating energy losses [89]. An example of using ampere counting for vehicle battery SOC estimation is presented by Alzieu et al. [90].

1.4 Vehicle Models

With the increasing importance, demand, and advancement of hybrid architecture, vehicle design is becoming more complex and demands additional hardware testing before passing products to the consumer. Unfortunately, vehicle hardware is costly in both manufacturing capital and production time. For this reason, automotive engineers are incorporating model based design in the fabrication of the next generation of vehicles.

1.4.1 Feasibility of Vehicle Models

Two criteria must be met for vehicle models to be feasible: the computer model must accurately portray the physical world and the model must be economically justifiable. Autonomie, vehicle simulation software developed by Argonne National Laboratory, was able to precisely model a Toyota Prius and obtain an estimated gas efficiency within 5% of the accepted value (Figure 37) [91]. Other software such as the Powertrain System Analysis Toolkit (PSAT), a precursor program to Autonomie, has been used to simulate and validate other vehicles [92].

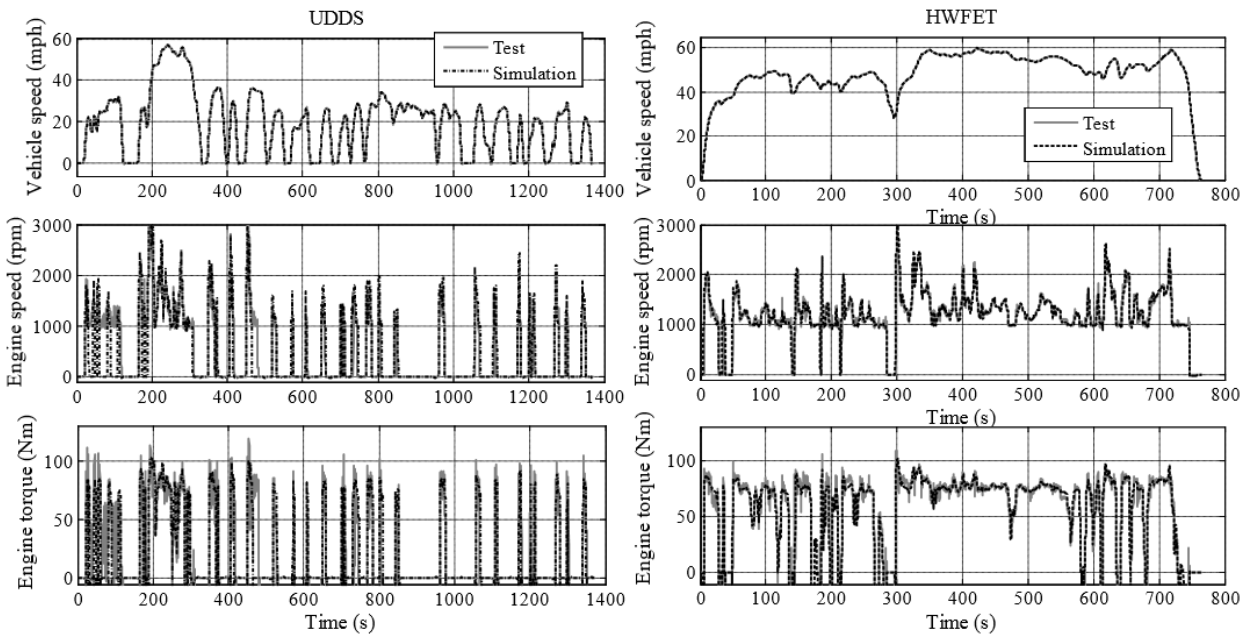

Figure 37: UDDS and HWFET cycles, test and simulation [91]

It is estimated that production costs can be reduced by up to 40 and 60% in the development and validation phases respectively by using model based design [93]. Although the largest benefit of simulation development that cannot be directly correlated with costs, is development time. It is significantly faster to test vehicles through simulation than to construct and test physical prototypes. Therefore, companies that adopt and implement testing through simulation have a competitive edge.

1.4.2 Types of Vehicle Models

There are two approaches to vehicle models, forward and backward design. In a forward model (Figure 38), the driver desires a predetermined speed and will adjust the accelerator or brake pedals which affect the powertrain and component controllers (e.g. throttle, displacement, gear number, mechanical breaking) in an attempt to meet that requirement. The driver will then modify this command depending on how closely the requirement was met. Because the model simulates what occurs in reality, it can be used to implement advanced components, account for transient effects (e.g. engine starting, shifting, clutch engage/disengagement), or develop control strategies [94].

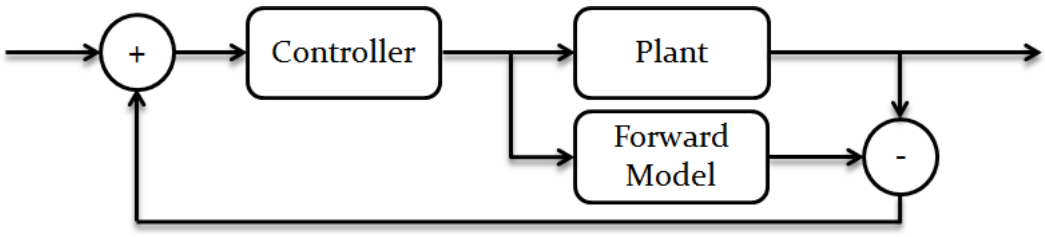

Figure 38: Forward vehicle model

By contrast, a backward model (Figure 39) initially adjusts the powertrain and component controllers to meet the desired speed. After the speed has been reached, it backward calculates the accelerator/brake pedal position required. Because of the model architecture, transient effects and control systems cannot be implemented. However, backward working models are less computationally intensive than their forward looking counterparts and can quickly identify and define vehicle trends which may be useful in vehicle design (e.g. powertrain configuration).

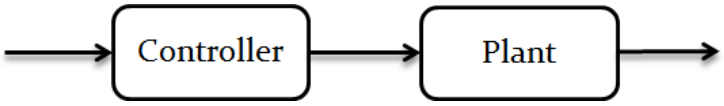

Figure 39: Backward vehicle model

1.4.3 Multiple Models

As vehicles become more complex, individual components are designed by a specialist team. Each team is responsible for developing that component and the associated models. A team may have different versions of the same model as the component progresses through development. Additionally, the team may have simple and complex models for differing levels of computational time and accuracy (Figure 40).

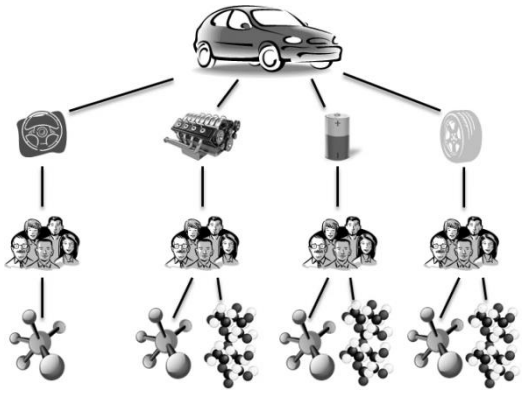

Figure 40: Tree diagram showing the branching of models

1.4.4 System Analysis Using Multiple Tools

A fundamental requirement for enterprise-wide simulation is a framework for integrating models that are developed in different languages/tools. Because different tools excel at modeling specific phenomena, numerous tools are used within a single company, such as original equipment manufacturers (OEMs). However, the task to relate these models into a single environment is often time consuming and difficult. Thus, it is rare that models associate with each other, and a comprehensive model often assumes components work at a steady state or utilizes look up tables.

While lookup tables are easy to use and develop, they cannot replace component simulation for control system development or component physical interaction within the vehicle model. Thus, it is important to maintain these more detailed models in order to evaluate new technology.

While it is possible to rebuild each model in a common language (e.g. Simulink), it is more practical to develop an architecture that supports communication between individual models in their native environment.

Because most models are created within the Matlab domain, it is the inferred common architecture. However, input and output functions are hardly uniform, as each model utilizes syntax most convenient to their subject matter (e.g. units, significant parameters, etc.). Therefore, the implied solution is to develop a "wrapper" which acts as a translator that filters information as it enters/leaves individual models allowing them to combine and form a complete simulation. This "wrapper" solution is possible within the Matlab domain, and is the predominating advantage of Autonomie modeling software. An illustration detailing the "wrapper" method is shown in Figure 41.

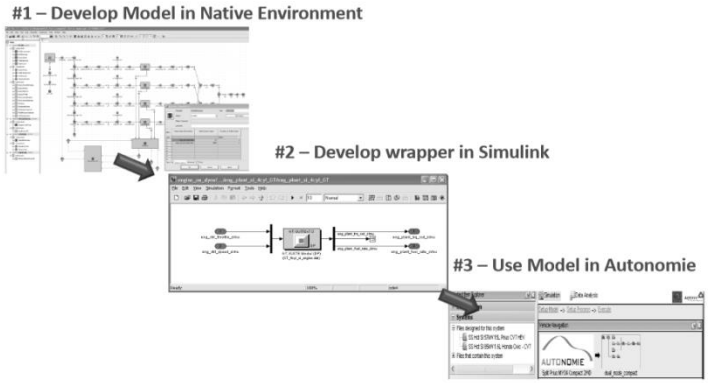

Figure 41: Model import into Autonomie from native environment [94]

Autonomie, which supports quick integration of foreign models, is an example of "plug and play" architecture. Plug and play systems allow tools to be linked together in order to form more detailed vehicle models. Autonomie has been shown to be able to link multiple tools together such as the GT-Power engine model, AMESim transmission model, and the CARSim vehicle dynamics model into a single vehicle simulation (Figure 42) [22].

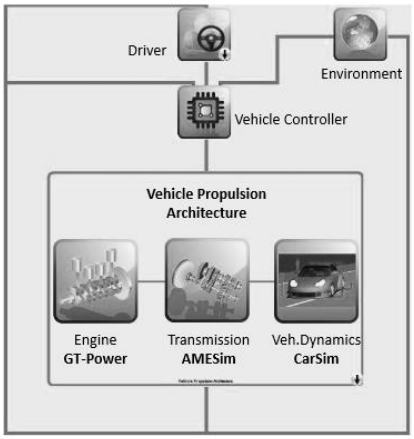

Figure 42: Multiple models related through Autonomie "plug and play" architecture [22]

Through this method, multiple models may be combined. This negates the limitations produced by using simplified models or lookup tables for external components to determining the net result of component testing. Additionally, it allows for a broader range of simulation scenarios while preserving the integrity of the original models.

2 Experimental

This section details the process of parameterizing equivalent circuit models from measured cell voltage response generated with the assistance of a time vs. current profile. Necessary equipment includes: a battery cycler, for applying current profiles; a host computer, for data logging and supervising the battery cycler; and a thermo chamber, for monitoring cell temperature. An overview of the model parameter fitting process is shown in Figure 43.

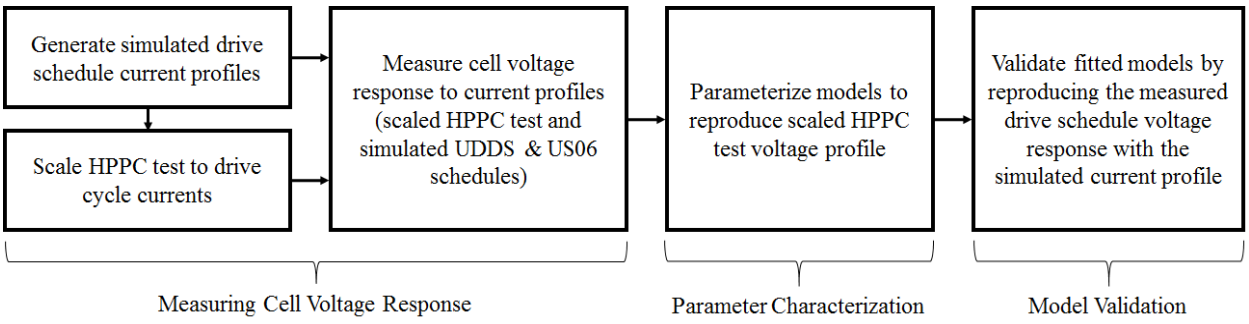

Figure 43: Overview of model parameter fitting process

Simulated current profiles were generated representative of the UDDS and US06 drive schedules by Autonomie software. These current profiles were then used to scale the HPPC test current. The cell voltage response was then measured with respect to these current profiles (Measuring Cell Voltage Response, s. 2.1). The measured HPPC voltage response was used to characterize the Rint and Thevenin models (Parameter Characterization, s. 2.2). The characterized models were then validated by the UDDS and US06 drive cycle voltage response profiles (Model Validation and Comparison, s. 2.3) before integration into Autonomie vehicle simulation software to estimate the importance of modeling the hysteresis effect (Simulation Results, s. 3).

2.1 Measuring Cell Voltage Response

The initial data provided within this work was collected by Joshua Lo and Leonardo Gimenez Paez, and is presented with their permission. Lo provided vehicle modeling services for the University of Waterloo Alternative Fuels Team (UWAFT) during the EcoCAR2 competition and generated simulated current profiles for the UDDS and US06 drive cycles [95]. Paez continued Lo's work and used the simulated current profiles, including a scaled hybrid pulse power characterization test [58], to measure the voltage response of a lithium-ion battery. Because of the origin of the data, the current profiles are representative of the EcoCAR2 Malibu model.

The experimental setup and procedures are written with reference to Paez's methods and descriptions [96]. Additional, simulated, current profiles are original work and were generated by Autonomie vehicle modeling software.

2.1.1 Test Bench Equipment & Configuration

The test bench schematic and test bench used to supply the current profile and measure the voltage response are shown in Figure 44 and Figure 45 respectively. The pictured battery cycler is the Maccor 4200^{TM}, which has 16 channels and a current control range of 0.1 – 15 A and a voltage control of 0.0 – 5.0 V per channel [97]. Eight channels are combined in parallel to achieve a maximum current of 120 A using a 4-wire parallel connection, where two low gauge wires deliver current and two high gauge wires measure voltage. The accuracy of the eight combined channels for each battery is ±0.1 A and ±1.0 mV. The current-voltage data is logged each second and every change equal to or exceeding 1 mV.

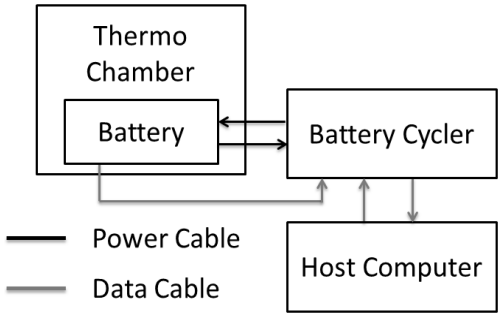

Figure 44: Test bench schematic

The pictured thermo chamber is the SubZero MicroClimate® 1.2 (Figure 45), which maintained the ambient temperature within ±0.5 K of the set point (23.75 °C) [98]. While inside the thermo chamber, the battery is enclosed in a vice that simulates a pack enclosure (two 4 mm thick inner aluminum plates, which simulate pack fins that distribute heat across the battery surface, inserted between two 5 mm thick acrylic plates, which simulate battery casing).

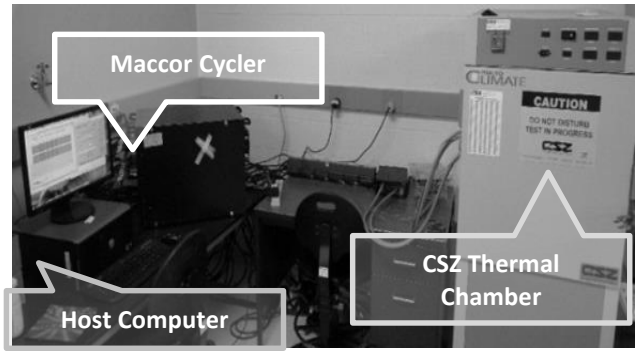

Figure 45: HPPC test bench

The pictured host computer (Figure 45) communicates with the battery cycler via LabView software [99]. All interactions between the test battery and battery cycler are orchestrated through this interface. The thermo chamber is not controlled by the host computer, and is externally monitored. Details of the test battery, designed for EREVs, are given in Table 4.

Table 4: Battery specifications

Parameter	Entry
Cathode Material	$LiFePO_4$ (LFP)
Anode Material	Graphite
Electrolyte	Liquid organic
Capacity range	18-21 Ah
Nominal Voltage	3.3 V
Dimensions	7.25×160×227 mm^3
Weight	496 g

2.1.2 HPPC Test Procedure

The hybrid pulse power characterization (HPPC) test normally consists of a 10 s discharge pulse at 1 C, a 40 s rest period, and a regenerative pulse at ¾C. The discharge and charge pulses represent the battery current profiles during normal operation and regenerative breaking respectively, with a smaller charge pulse depicting energy losses. Additional information regarding the standardized HPPC test procedure recommended by the Department of Energy can be found in their battery test manual [54].

The standardized test procedure was modified to represent for the current profiles experienced by the EcoCAR2 Malibu model within Autonomie software, scaling the discharge pulse to 5C and the regenerative pulse to 3 ¾ C. The Malibu US06 drive cycle current demand is overlaid with the scaled HPPC test current profile in Figure 46. The current magnitude exhibited by the US06 drive cycle greatly exceed 1C and ¾C recommended by the test, and were deemed unrealistic of drive cycle behavior. For this reason, the modified test procedure was used.

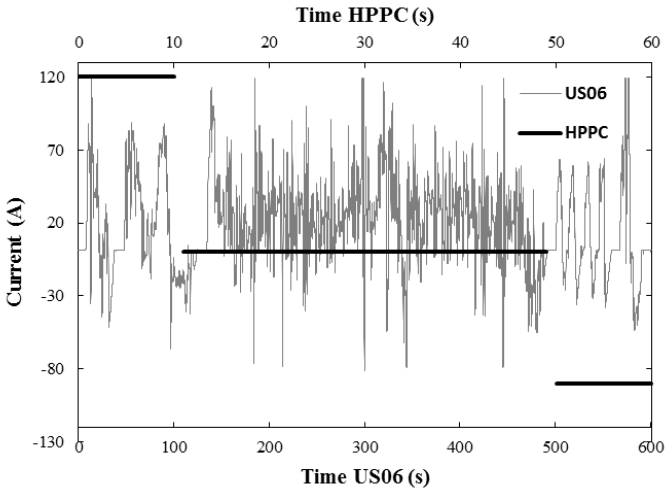

Figure 46: Modified HPPC test overlaid with Autonomie generated US06 current profile

The battery is initially characterized by a full charge/discharge cycle. The battery is charged at 1C constant current, followed by a constant voltage charge until the current decreases to C/20. The battery is then rested until equilibrium is reached, defined as a change in voltage smaller than 5 mV over a ½ hour period or a rest period exceeding two hours. The battery is then discharged at 1C constant current until the cut-off voltage is reached, then at constant voltage until the current reaches C/20.

The modified HPPC current profile (10 s discharge pulse at 5C, followed by a 40 s rest period, and then a 10 s 3.75C charge pulse) is performed at 10% SOC intervals, where the voltage response is recorded by the host computer. To reach the desired SOC between tests, the battery is discharged to the cutoff voltage (i.e. manufacturer defined 0% SOC) by the above method, and then charged to the desired SOC by coulomb counting at constant current (1.25C).

2.1.3 Drive Schedule Procedure

Simulated drive schedule current profiles were generated through Autonomie software using the EcoCAR2 Malibu model. These current profiles were modified in the event that a regenerative pulse would result in cell overcharge, defined as a voltage exceeding the maximum rated battery voltage. This is assumed to be similar operation to an automotive battery controller, which would avoid self-inflicted harm to the on-board battery pack. Therefore, these profiles are expected to be representative of a real-world hybridized vehicle.

Before applying the simulated current profile to the cell, the battery is initially characterized by a full charge/discharge cycle (see previous section). As capacity is expected to change during discharge, the drive schedule is repeated until the cutoff voltage is reached. Upon completion of the drive schedule, the cell is rested until equilibrium, and re-characterized before application of the next drive schedule (UDDS, US06, etc.). Battery current and voltage throughout the UDDS profile is displayed in Figure 47.

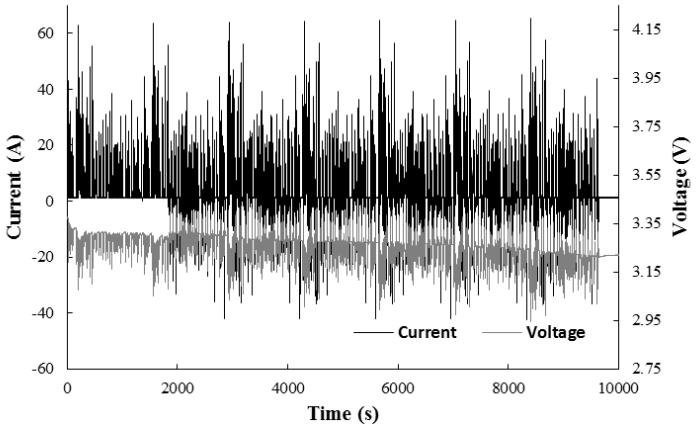

Figure 47: UDDS profile current and voltage

2.2 Parameter Characterization

The Rint and Thevenin equivalent circuit model parameters were characterized with reference to the aforementioned voltage response and current profiles. The characterization was performed by changing the circuit parameters to minimize the sum of time-weighted voltage response deviations with a generalized reduced gradient (GRG) non-linear solver. Equivalent circuit model equations are reintroduced and detailed before presenting the time-weighted solver objective function.

2.2.1 Model Equations

ECMs estimate the battery voltage (V_{model}) as the difference between the open circuit (V_{OC}) and equivalent circuit (V_{circ}) voltages (Eq. 1). V_{OC} is influenced by SOC and temperature. V_{circ} is determined by model parameters, and may be externally influenced depending on equivalent circuit complexity [53].

$$V_{model} = V_{oc} - V_{circ} \quad \text{(Eq. 1)}$$

2.2.1.1 Rint Model

The Rint model is composed of a single resistor (Figure 30), and V_{circ} is defined by a single term V_1 (Eq. 2). The model predicted voltage is the open circuit voltage with an offset (V_1) that is defined as the internal resistance (R_1) scaled by current (i_1). The internal resistance is often abbreviated as R_{int}, from which the name is derived [54]. Because of the lack of capacitors (or inductors), the Rint model cannot capture hysteresis, or transient, effects.

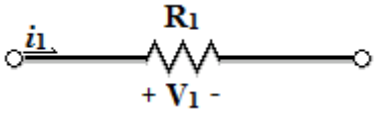

Figure 48: Internal resistance ("Rint") model

$$V_{circ\,(Rint)} = V_1 = i_1 R_1 \quad \text{(Eq. 2)}$$

2.2.1.2 Thevenin Model

The Thevenin model is composed of a resistor and a resistor and capacitor in parallel (Figure 33), and V_{circ} is defined by two terms V_1 and V_2 (Eq. 3). Similar to the Rint model, current is linearly scaled with a resistance to determine V_1. V_2 is determined by the current across R_2 (i_2), which is influenced by the energy stored within the capacitor (C_1) and creates a time dependent voltage response. In order to characterize the model parameters, it is of interest to express the i_3, in terms of i_1. Details of this substitution are provided in Eq. 7 – 12.

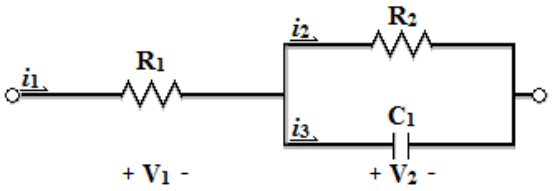

Figure 49: Thevenin circuit model

$$V_{circ\ (Thevenin)} = V_1 + V_2 = i_1 R_1 + i_2 R_2 \quad \text{(Eq. 3)}$$

As R_2 and C_1 are in parallel, their respective voltages are identical (Eq. 7).

$$V_2 = i_2 R_2 = \frac{1}{C_1}\int_{t_1}^{t_2} i_3\, dt + V_2(t_1) \quad \text{(Eq. 7)}$$

By Kirchhoff's laws, Eq. 7 can be transformed to express the current across C_1 as a function of the initial current (i_1), circuit elements R_2 & C_1, and preceding voltage (Eq. 8 – 9).

$$i_1 = i_2 + i_3 \quad \text{(Eq. 8)}$$

$$i_3 = i_1 - \frac{1}{R_2 C_1}\int_{t_1}^{t_2} i_3\, dt - \frac{V_2(t_1)}{R_2} \quad \text{(Eq. 9)}$$

The integral term in Eq. 9 can be expressed by trapezoidal approximation with sufficiently small time steps. The capacitor current can be simplified by defining the limits of integration, t_2 and t_1, as the present and previous time steps respectively (i.e. $i_{3(t2)} = i_3$) (Eq. 10).

$$i_3 = i_1 - \frac{(t_2 - t_1)}{R_2 C_1}\left[\frac{i_3}{2} + \frac{i_{3(t_1)}}{2}\right] - \frac{V_2(t_1)}{R_2} \quad \text{(Eq. 10)}$$

Collection and isolation of i_3 (Eq. 11) produces the Thevenin model with i_1 as the sole input (Eq. 12).

$$i_3 = \frac{\left[i_1 - \frac{t_2 - t_1}{2R_2C_1} i_{3(t_1)} - \frac{V_2(t_1)}{R_2}\right]}{1 + \frac{t_2 - t_1}{2R_2 C_1}} \quad \text{(Eq. 11)}$$

$$V_{model} = V_{OC} - i_1 R_1 - (i_1 - i_3) R_2 \quad \text{(Eq. 12)}$$

Alternatively i_2, instead of i_3, can be isolated by substitution in Eq. 3. This approach requires two integral approximations (i.e. $\int i_1 - i_3\, dt$), but provides alternative initial conditions (i.e. $i_2 = 0$ vs. $i_3 = i_1$). This form is useful in situations where the initial condition $i_3 = i_1$ cannot be met as it defines an initial value with a variable.

$$i_2 = \frac{\left[\frac{t_2 - t_1}{2R_2C_1}(i_1 + i_{1(t_1)} - i_{2(t_1)}) - \frac{V_2(t_1)}{R_2}\right]}{1 + \frac{t_2 - t_1}{2R_2 C_1}} \quad \text{(Eq. 13)}$$

2.2.2 Circuit Parameter Characterization

Model parameters (i.e. R_{int}, R_1, R_2, and C_1) are characterized to set the objective function, defined as the difference between the measured and modeled sum of deviations, to a minimum

value (Eq. 14) using a GRG non-linear solver within Microsoft Excel software. Because the measurement intervals are inconsistently spaced, the measured and modeled values are weighted to provide an equal representation with respect to time (Eq. 15-16).

$$\sum |Measured - Modeled| = Objective \quad \text{(Eq. 14)}$$

$$Measured_{t1} = V_{measure}(t_2 - t_1) \quad \text{(Eq. 15)}$$

$$Modeled_{t1} = V_{model}(t_2 - t_1) \quad \text{(Eq. 16)}$$

Alternative methods of calculating model deviations were considered, such as the common statistical "least squares" technique (Eq. 17). While the least squares method avoids theoretical complications for further statistical analysis (i.e. it is difficult to integrate an absolute value) [100], it propagates model error. By squaring the differences, a single large deviation is more impactful than multiple smaller deviations – which yields a net increase in model deviations relative to Eq. 14. Improved model accuracy was deemed paramount to simplified statistical analysis, and thus Eq. 14 selected over Eq. 17.

$$\sum (Measured - Modeled)^2 = Objective \quad \text{(Eq. 17)}$$

The following subsections detail solver constraints, characterization intervals, assumptions, and parameter influence.

2.2.2.1 Solver Constraints, Characterization Intervals, and Assumptions

The GRG non-linear solver constraints chosen for characterization of the model parameters were: a constraint precision of $1x10^{-13}$, a forward convergence of $1x10^{-17}$, and a multi-start population size of $1x10^{4}$ with 0 random seeds. The required boundaries on the solver parameters were $0 < R_1 < 4.0x10^{-2}$ Ω, $0 < R_2 < 4.0x10^{-2}$ Ω, and $0 < C_1 < 2.5x10^{3}$ F. The Rint and Thevenin model parameters were characterized in 10% SOC intervals.

Cell relative capacity (SOC) was assumed constant throughout each HPPC test. Linear interpolation of circuit parameters (R_1, R_2, and C_1) and open circuit voltage (V_{OC}) was assumed sufficiently accurate with the characterization intervals.

2.2.2.2 Parameter Influence

It is beneficial to interpret the parameter influence with reference to their respective models. With respect to the Rint model, R_1 represents the deviation from the open circuit voltage (Figure 50). With constant current, increasing or decreasing R_1 provides a larger or smaller deviation respectively.

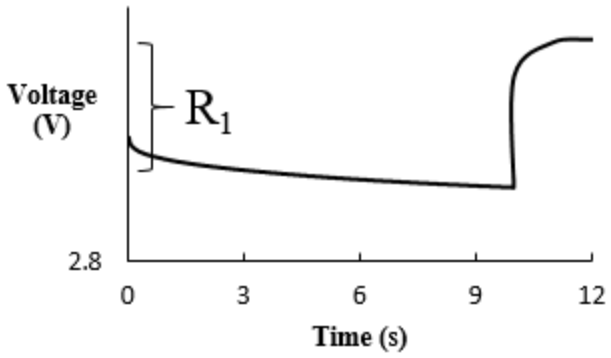

Figure 50: Rint model parameter correlation

As the deviation is non-constant with respect to time, model error can be minimized by characterizing R_1 with reference to the average deviation. A representative Rint model fit, which emphasizes estimation limitations for transient effects, is shown in Figure 51.

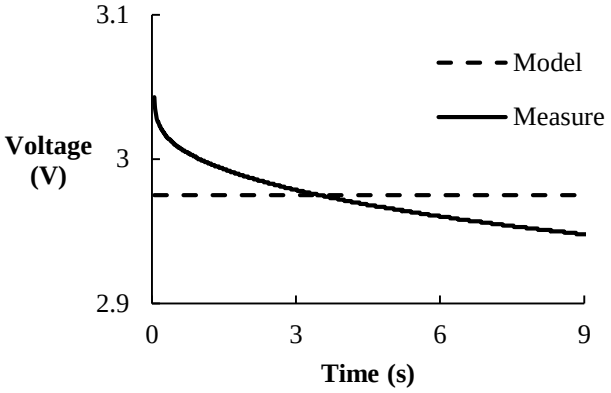

Figure 51: Rint model error originates from hysteresis effect

With respect to the Thevenin model, R_1 influences the initial deviation from the open circuit voltage identically to the Rint model, and $R_2|C_1$ influence the magnitude and rate of the final deviation respectively (Figure 52). Additionally, provided the absence of current, R_2 and C_1 determine how quickly the cell resumes open circuit voltage from rest.

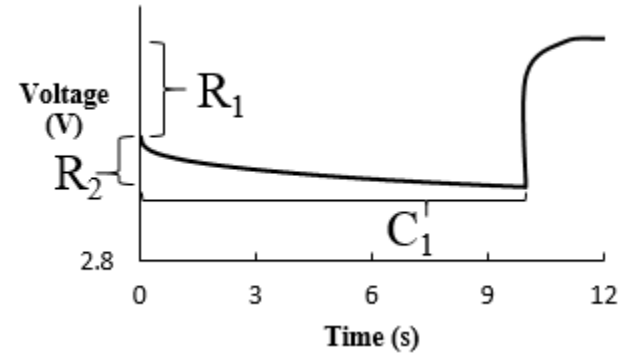

Figure 52: Thevenin model parameter correlation

In both models, error originates from the inability to perfectly capture the hysteresis effect. However, while the Thevenin model predicts this effect with limited curvature, error is significantly decreased compared to the Rint model (Figure 53). The Thevenin model can be further improved by additional R|C parameters in series (Equivalent Circuit Models, s. 1.3.1). The significance of the Thevenin to Rint model improvements, with commentary regarding higher fidelity models, is provided in Model Validation, s. 2.3.

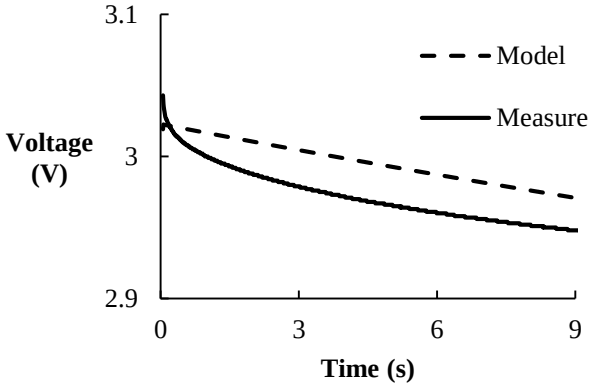

Figure 53: Thevenin model error originates from imperfect capture of the hysteresis effect

2.2.3 Fitted Circuit Parameters

The Rint and Thevenin model parameters were characterized by minimizing the objective function, defined as the sum of the absolute voltage difference between the modeled and measured values, by varying the circuit parameters (Circuit Parameter Characterization, s. 2.2.2). The fitted parameters and relevant discussion are provided within this section.

The characterized Rint model resistor values are shown in Figure 54. The resistance is shown to have an inverse relationship with capacity, and decreases with increasing SOC. The resistance increases drastically at SOC < 10% as the cell approaches full discharge. This sudden resistance increase indicates that the cell exhibits new, or more pronounced, electrochemical phenomena at low SOC.

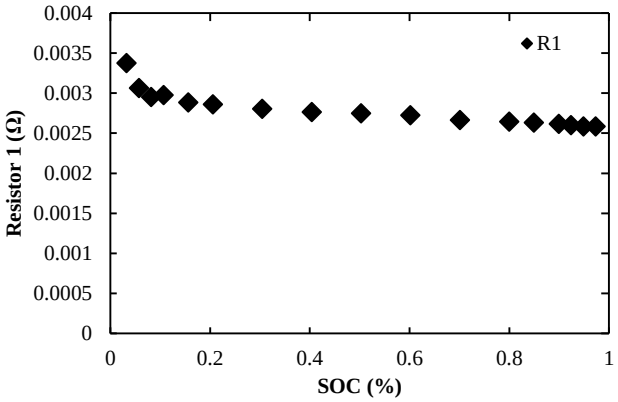

Figure 54: Fitted Rint model resistor values

The Rint model error encapsulated by the objective function (Eq. 14, s. 2.2.2) is shown in Figure 55. Similar to the resistor values, the error follows an inverse relationship with capacity, and decreases with increasing SOC. Additionally, the error drastically increases at SOC < 10%, suggesting that the Rint model is a poor choice for estimating cell voltage in this region.

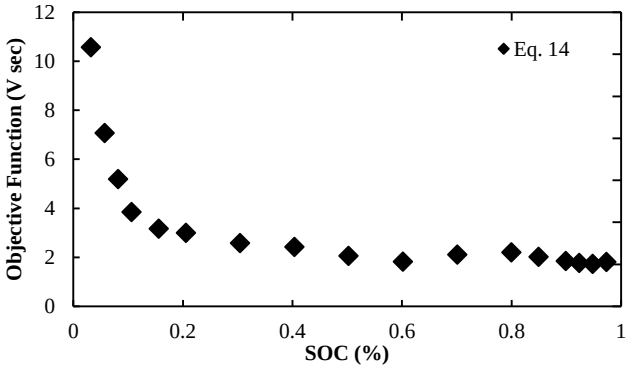

Figure 55: Rint model objective value w.r.t. increasing SOC

The characterized Thevenin model resistor and capacitor values are shown in Figure 56. Thevenin resistor R_1 exhibits trends similar to the Rint model, and exhibits an inverse relationship with SOC. From a theoretical perspective, R_1 characterizes the "cell bulk resistance" and should be a constant value where R_2 captures SOC dependent chemical interaction. This does not match the empirical results, and it is implied that some of the chemical interaction is "masked" in R_1, implying that model accuracy may be improved with additional R|C components. The resistor (R_2) and capacitor (C_1) exhibit an inverse and direct relationship with SOC respectively. This indicates that not only does the hysteresis effect increase in magnitude at lower SOCs, but it applies at a faster rate.

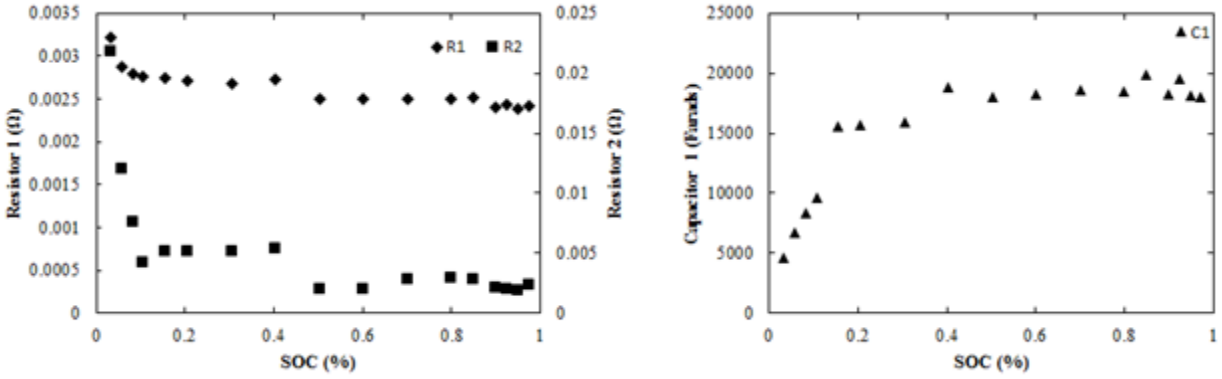

Figure 56: HPPC fitted parameters R_1 & R_2 (left) and C_1 (right)

The Thevenin model error encapsulated by the objective function (Eq. 14, s. 2.2.2) is shown in Figure 57. Figure 57 experiences similar trends to Figure 55, suggesting that the Thevenin model also has difficulty predicting low SOC phenomena. Figure 57 is also "steadily

increasing" in sections (i.e. < 10% and < 60%) rather than distinct curvature, again suggesting that additional R|C elements may further increase model accuracy. An overlooked distinction between the Figures is the ordinate units, the absolute sum of errors for the Thevenin model is an order of magnitude lower!

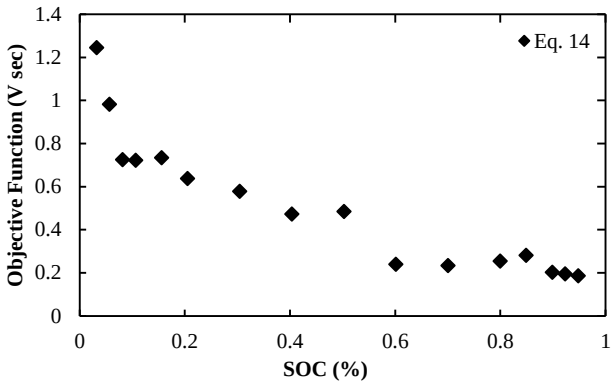

Figure 57: Decreasing objective value w.r.t. increasing SOC

The model objective functions displaying a similar curvature and difference in magnitude is convenient for determining hysteresis significance. As both models display similar curvature with reference to SOC it is intrinsically implied that both models will experience similar errors in these regions i.e. the error associated with each model originates from the same phenomena, therefore differences in the simulation results can be attributed to differences in model accuracy. Additionally, as the objective function for the Thevenin model is an order of magnitude less than the Rint model, the difference between the simulated results is expected to be significant.

It is important to emphasize the smooth curvature of both the Rint and Thevenin parameters, as this curvature allows for interpolation between points. This is necessary for implementation into vehicle simulation software, as interpolation is used to determine circuit parameters for unrecorded SOC values. Because of the smooth curvature of the plots, the interpolated values can be assumed to be accurate.

2.3 Model Validation and Comparison

The Rint and Thevenin characterized models were used to reproduce the voltage response of the aforementioned battery cycles: the HPPC test standardized current profile, and current profiles representative of the UDDS and US06 drive cycles (Experimental, s. 2). To illustrate the difference of the models, and their ability to capture the hysteresis effect, the Rint and Thevenin predictions are aligned with the measured voltages from the HPPC test in Figure 58. The model predictions are then compared with the measured voltage from the simulated drive cycles, the Rint and Thevenin UDDS and US06 comparisons are shown in Figure 59 & Figure 60 and

Figure 61 & Figure 62 respectively. Enlarged versions of these figures are available within Appendix G – Model Validation.

By inspection of the Rint HPPC test results (Figure 58, left), it is clear that model deviations originate from, and are proportional to, the hysteresis effect. Prediction error peaks with current shifts, notably at 10 and 50 s. There is also a comparably large deviation during the relaxation period (10 – 50 s), where the model assumes open circuit voltage and the battery slowly dissipates the hysteresis offset. During phases of constant current, 0-10 and 50-60 s, prediction error approaches and then deviates from zero. This error pattern again originates from the hysteresis effect, as the Rint model is characterized to predict the "average" voltage during this period as time dependent prediction is impossible with a simple resistance based model.

Inspection of the Thevenin HPPC test results (Figure 58, right) shows improvement in modeling the hysteresis effect. Model prediction error during constant current (0 – 10, 10 – 50, and 50 – 60 s), is greatly reduced with an offset less than 0.02 V. Similar to the Rint model, the Thevenin model exhibits error during current shifts notably at 10 and 50 s. However the magnitude of this error is greatly diminished when compared to the Rint model, with prediction errors of 1.5 vs. 0.8 V and 0.8 vs. 0.4 V respectively.

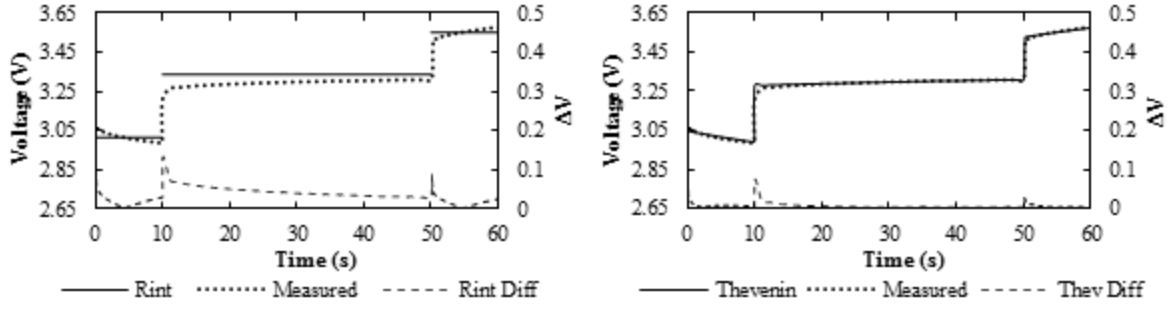

Figure 58: HPPC Rint vs. measured (left), HPPC Thevenin vs. measured (right)

The Rint model predicted voltage for the UDDS cycle, a smooth drive cycle with gradual current shifts, is shown in Figure 59. The UDDS modeled offset increased relative to the HPPC tests, 0.2 vs. 0.1 V respectively. This is expected as the HPPC test 40 s rest period allows the battery to resume open circuit voltage between current shifts, and the drive cycle "rest periods" are encountered less frequently and for shorter duration. Because of this, Rint model voltage prediction deviates from the measured values until 300 s where the hysteresis voltage drop terminates with a consistent offset of 0.2 V for the remainder of the cycle.

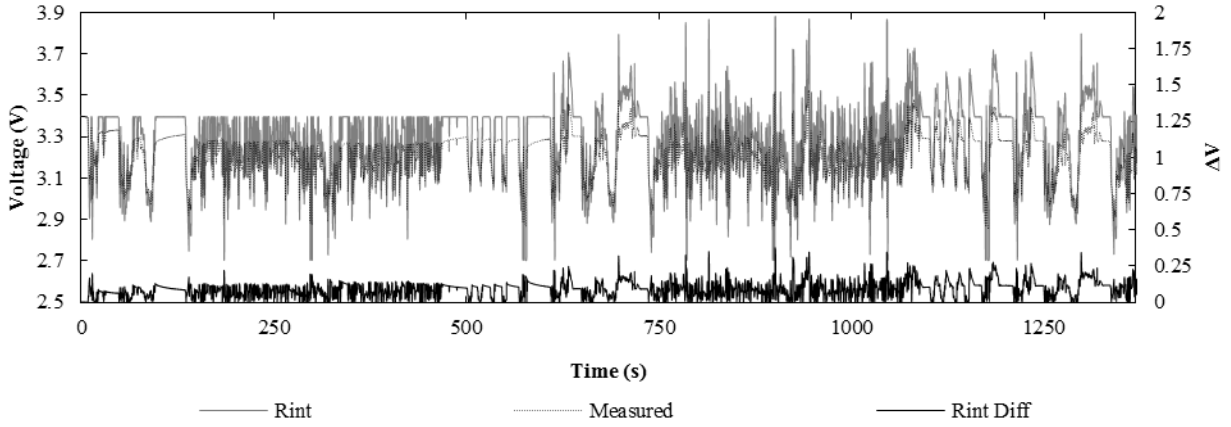

Figure 59: Rint predicted voltage vs. measured voltage for current profile representative of UDDS cycle

The Thevenin model captures this hysteresis effect, matching the measured voltage (Figure 60). The Thevenin model lacks a constant offset, and prediction error originates from current shifts similar to the HPPC test current profile.

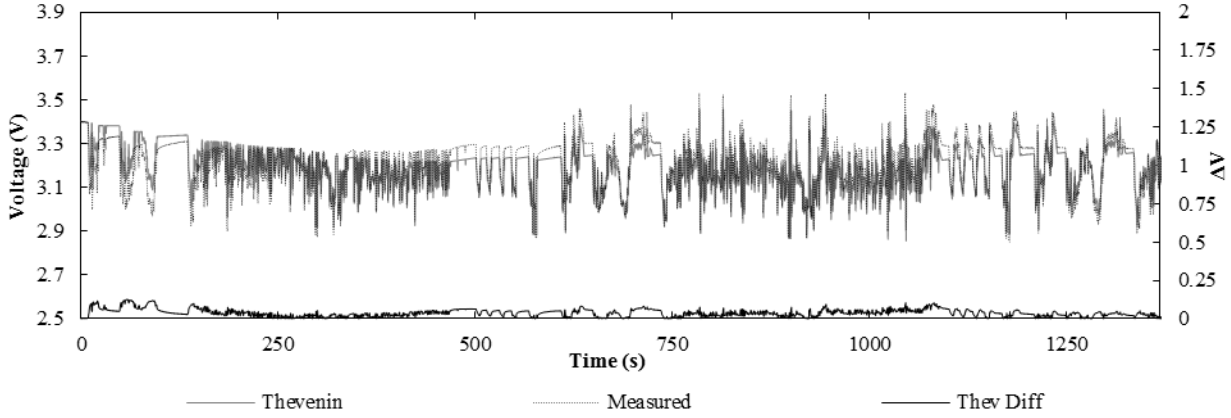

Figure 60: Thevenin predicted voltage vs. measured voltage for current profile representative of UDDS cycle

The Rint model predicted voltage for the US06 cycle, an aggressive drive cycle with large current shifts, is shown in Figure 61. Similar to the UDDS cycle, the Rint model accrues an offset from the measured voltage. Dissimilar to the UDDS cycle, the rate at which this offset is obtained is significantly increased reaching a terminal value at 100 s. The decreased number of rest periods, and increased current demands, both increase the rate of hysteresis – the cause of the offset.

The decreased magnitude of largest model error can be attributed to the vehicle controller monitoring the "aggressiveness" of the drive cycle. In rapid deceleration applications the controller does not take advantage of regenerative breaking for safety concerns, as it prioritizes stopping the vehicle over recharging the battery. For this reason the size of current shifts is diminished, i.e. discharge to charge becomes discharge to rest. As the largest model error occurs during current shifts, it is natural that error decreases when large current shifts become less prevalent.

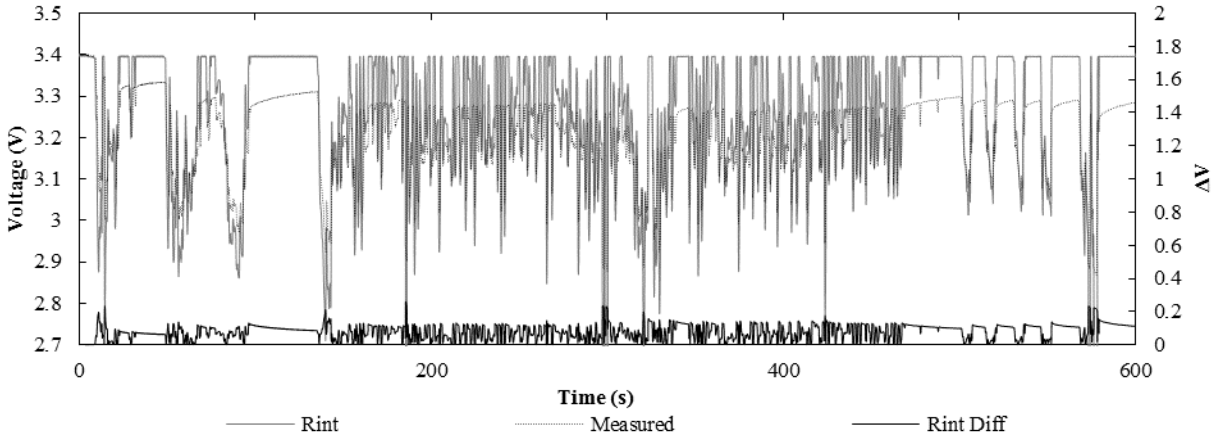

Figure 61: Rint predicted voltage vs. measured voltage for current profile representative of US06 cycle

The Thevenin model captures the hysteresis effect of the US06 cycle and shows improvement over the Rint model (Figure 62), but has difficulty with the increased frequency of current shifts. An interesting observation is the model predicted voltage decays relative to the measured voltage over the duration of the cycle, with an over/under prediction before/after 200 and 300 s respectively. This implies that the hysteresis effect is caused by multiple different phenomena that occur at different rates. This conclusion is supported by observations in Nyquist plots obtained through electrochemical impedance spectroscopy (EIS) tests [58] [101] and by the increased accuracy of dual capacitance models [53].

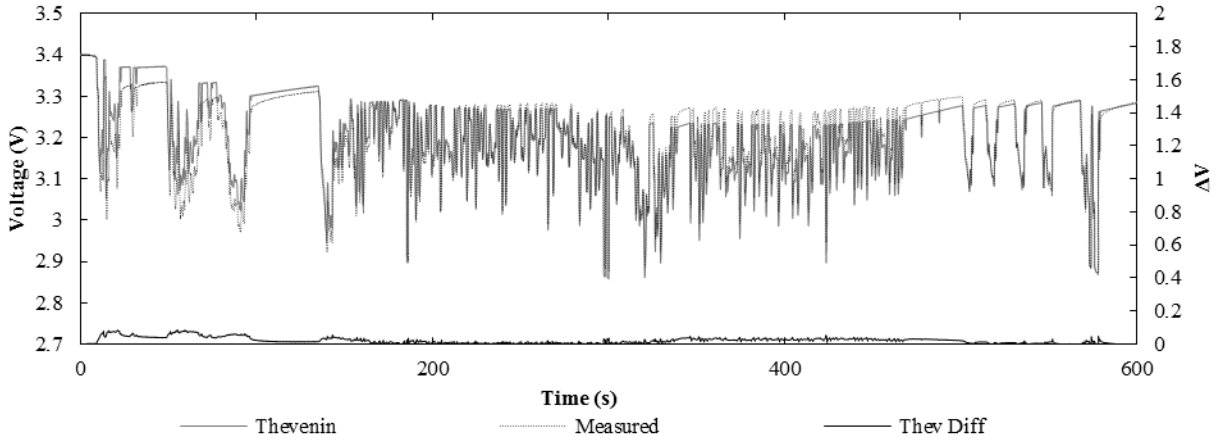

Figure 62: Thevenin predicted voltage vs. measured voltage for current profile representative of US06 cycle

3 Simulation Results

The following simulation results were obtained using Autonomie vehicle modeling software version Rev13SP1. The simulation vehicle was the "BEV FixedGear 2wd Midsize" vehicle utilizing the software defaults for all components excluding the energy storage system (ess). The energy storage system components were modified to the Rint and Thevenin control schemes (ctrl) and models (plant). This modification created two identical vehicles with the exception of their energy storage system (i.e. Rint vs. Thevenin). A simplified representation of the simulated vehicle powertrain is shown in Figure 63, a comprehensive representation including a list of all model related files, can be found in Appendix A – Simulated BEV Powertrain. Simulation results are presented in a style consistent with Autonomie software, i.e. table and figure formatting is retained, to assist in result replication.

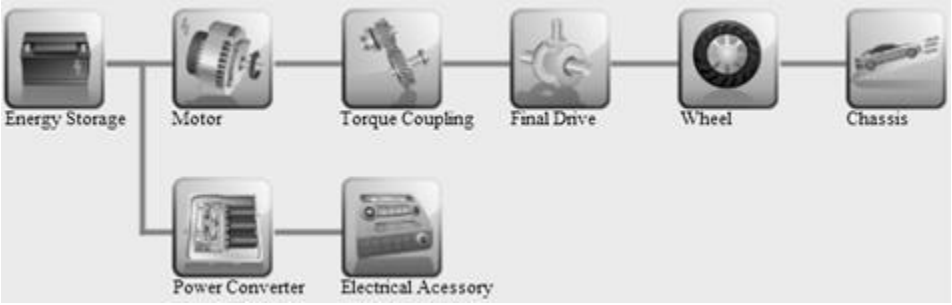

Figure 63: Autonomie high level view of Simulink simulated BEV powertrain

For each simulation, the vehicle propulsion controller (VPC) attempts to trace the drive cycle speed. Significant deviation from the trace, defined as a difference exceeding 2 mph for more than 2% of the total simulation time, can be indicative of simulation error. Upon reaching the end of the drive cycle simulation time, or all energy related resources (e.g. battery capacity, gas, etc.) are exhausted, the VPC will terminate the simulation. For battery electric vehicles (BEVs), the default terminal SOC is 10% and was used for these simulations. Additional information regarding vehicle models can be found in Vehicle Models, s. 1.4.

Simulation results are composed of these vehicles completing the US06, HWFET, and UDDS standardized drive cycles (Table 5). The deviations from the trace are sufficiently small (less than 2%) which indicates the simulation completed without error.

The Thevenin model predicts increased electrical consumption and decreased bidirectional energy storage efficiency across all simulated drive cycles. This relates to a decreased travel distance in the US06 and HWFET drive cycles and a decreased terminal SOC in the UDDS drive cycle. Deviations from the speed trace in the US06 drive cycle originate from the inability of the battery pack to meet the motor power demands. The marginally increased error within the Thevenin simulation (0.24 vs. 0.23%) suggests the Thevenin battery pack has a relatively diminished power output which hinders high acceleration and top speed applications.

Table 5: Rint & Thevenin Simulation Results

Drive Schedule		**US06**		**HWFET**		**UDDS**	
Model Type		Rint	Thevenin	Rint	Thevenin	Rint	Thevenin
%Time Trace Missed by More Than 2 mph	%	0.23	0.24	0	0	0	0
Distance Traveled	mi	5.81	5.52	10.25	9.74	7.44	7.44
Simulation Time	s	390.9	375.9	764.0	716.1	1369	1369
Electrical Consumption	Wh/mi	478.33	512.94	259.52	290.65	272.44	274.49
Initial SOC	%	70	70	70	70	70	70
Final SOC	%	10.01	10.01	13.67	10.01	27.21	26.89
Delta SOC	%	-59.99	-59.99	-56.33	-59.99	-42.79	-43.11
Bidirectional Energy Storage Efficiency	%	81.43	78.72	93.74	90.29	94.62	94.17

The results of Table 5 are illustrated by Figure 64 - Figure 69, which compare the model simulated drive cycle battery capacity (SOC) and voltage. When viewing the figures, remember that the Rint model assumes open circuit voltage (OCV) whenever there is an absence in current demand. This allows coasts (i.e. V = OCV during the coast to V > OCV during regenerative breaking) and stops (i.e. V = OCV during the stop to V < OCV during acceleration) to be easily identified. In both cases, the Thevenin model voltage gradually resumes OCV during the rest period due to the hysteresis effect. The remainder of the section is comprised of sections disserting the significance of simulation convergence or divergence.

The UDDS simulation Rint and Thevenin model SOC with respect to simulation time is illustrated in Figure 64. The two models begin to diverge at 100 s and the rate of divergence increases rapidly after 300 s. Prior to 150 s, SOC tends to increase after depletion from the effects of regenerative breaking. This behavior is absent in the later sections of the cycle, suggesting the rate of deceleration was too high to safely operate the generator and it was disabled by the VPC. The Rint and Thevenin vehicles reach terminal SOC at 390.9 and 375.9 s respectively.

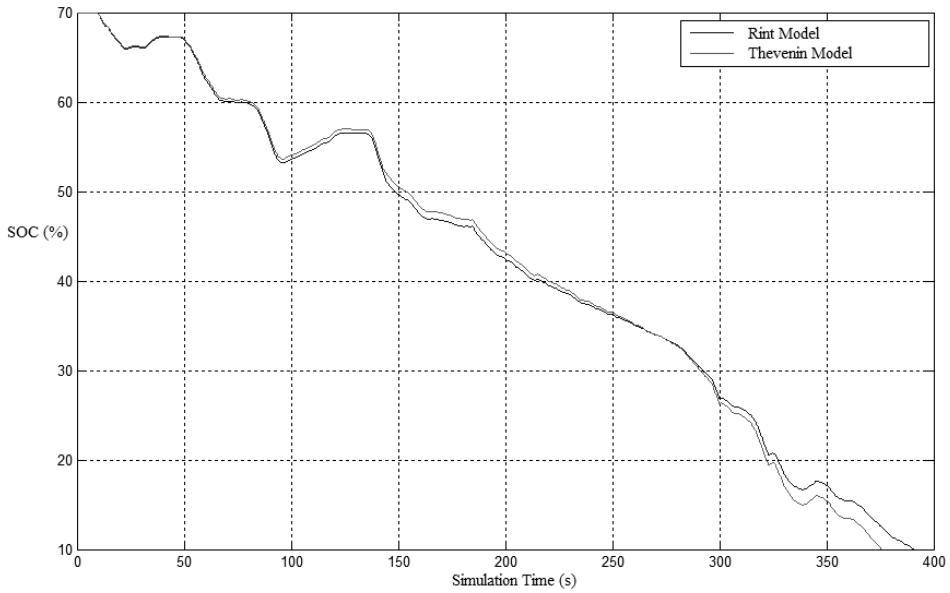

Figure 64: Simulated Rint and Thevenin ECM SOC for the US06 drive cycle

Inspection of the US06 drive cycle with respect to battery voltage explains these divergences (Figure 65). Before the 150 s mark the drive cycle is relatively relaxed, and consists of small voltage fluctuations. There are stops located at 42 and 142 s (indicated by a constant Rint model voltage) which align with the regenerative breaking observed in Figure 64. The drive cycle becomes more aggressive post 150 s as the voltage begins to fluctuate rapidly to accommodate the power demands. The vehicle decelerates too rapidly for the controller to enable regenerative breaking, and the energy is lost. With the battery in constant discharge, the hysteresis effect accumulates and the Rint and Thevenin voltage predictions diverge. The Thevenin model predicts decreased battery voltage which enables an increased current demand to meet the motor power requirements. This increased current draw, coupled with increased resistance, increases electrical consumption relative to the Rint model as displayed in Table 5.

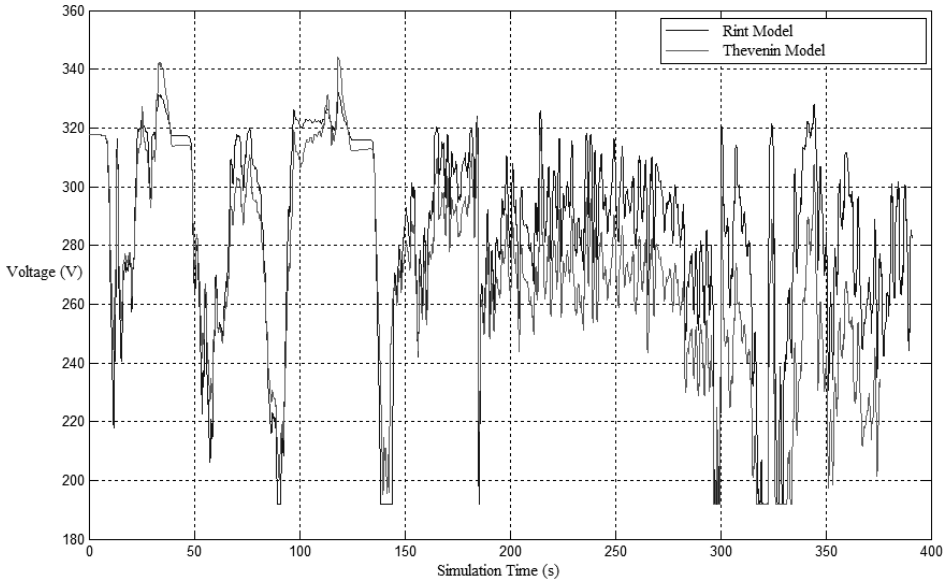

Figure 65: Simulated Rint and Thevenin ECM voltage for the US06 drive cycle

The HWFET simulation Rint and Thevenin model SOC with respect to simulation time is illustrated in Figure 66. The two models gradually deviate, especially after the 300 s. The magnitude of the regenerative periods, which occur at 120 and 280 s, are smaller than those observed in the US06 cycle suggesting the decrease in speed was lesser in magnitude. The Rint vehicle completes the cycle at 764 s with 13.67% SOC remaining, whereas the Thevenin vehicle reaches terminal SOC at 716 s and ends the cycle prematurely.

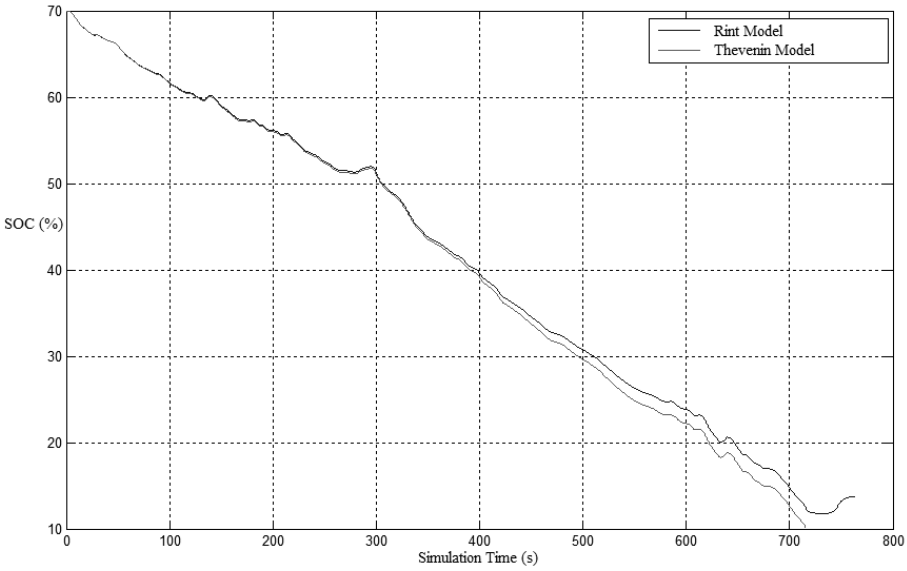

Figure 66: Simulated Rint and Thevenin ECM SOC for the HWFET drive cycle

Inspection of the HWFET drive cycle with respect to battery voltage explains this performance (Figure 67). The regenerative breaking, shown at 120 and 280 s, occur to a momentary decrease in speed, rather than a complete stop, and is supported by the voltage profile. The HWFET cycle voltage profile shows a consistent constant discharge that cannot easily be parsed into segments dissimilar to the US06 cycle. This is expected highway performance, and mirrors SOC behavior (Figure 66). Again, the Thevenin model predicts a lower battery voltage due to the hysteresis effect exalted by the sustained rate of discharge. This results in an increased current draw, faster capacity depletion, and decreased range.

It is of interest to note that this increase in electrical consumption prohibits the Thevenin vehicle from completing the drive cycle and ceases forward movement at 716 s. Because of this early termination, the Thevenin model does not benefit from the regenerative breaking displayed at the end of the cycle at 750 s.

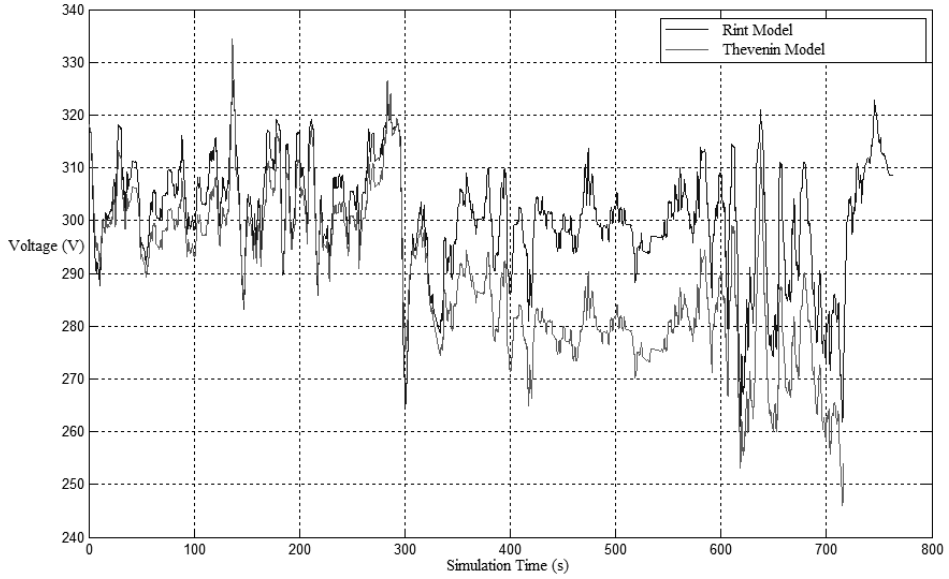

Figure 67: Simulated Rint and Thevenin ECM voltage for the HWFET drive cycle

The UDDS simulation Rint and Thevenin model SOC with respect to simulation time is illustrated Figure 68. The Rint and Thevenin model predictions are almost indistinguishable, with a gradual deviation occurring throughout the cycle. Across the 1369 s cycle, the relative capacity difference is 0.31%.

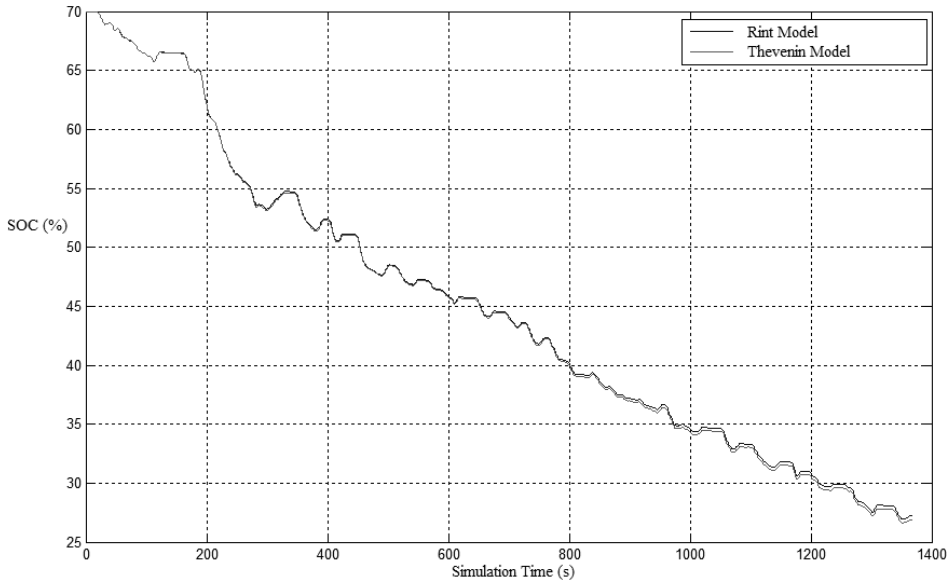

Figure 68: Simulated Rint and Thevenin ECM SOC for the UDDS drive cycle

Inspection of the UDDS drive cycle with respect to battery voltage reveals comparable convergence (Figure 69). There are many "stops" throughout the cycle that allow the hysteresis effect to dissipate similar to the first 150 s of the US06 cycle. During each "stop" the voltage

prediction converges, and the significance of modeling the hysteresis effect decreases. For this reason, a larger difference is shown in the US06 and HWFET cycles relative to the UDDS cycle.

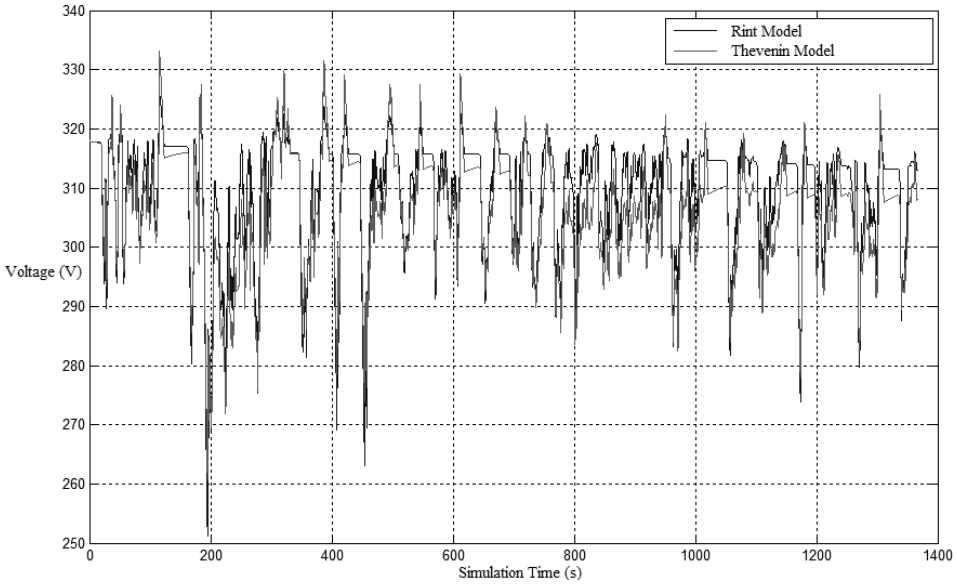

Figure 69: Simulated Rint and Thevenin ECM voltage for the UDDS drive cycle

The models contrast when the battery is provided aggressive or sustained current profiles. The UDDS drive cycle is representative of a leisurely drive in an urban environment, and exhibits the smallest model prediction difference of 2.05 Wh mi^{-1}. The HWFET drive cycle is representative of a highway scenario, and exhibits an increased prediction difference of 31.13 Wh mi^{-1}. The US06 drive cycle is representative of "aggressive" or high acceleration drive, and exhibits the largest prediction difference of 34.61 Wh mi^{-1}. This is expected as the hysteresis effect, which is captured by the Thevenin – but not the Rint – model, is more prevalent in the current profiles exhibited by the HWFET and US06 drive cycles.

4 Effect of Electrical Losses on Range

While an electrical consumption metric is readily applicable from a design perspective, it is useful to express the model differences in more tangible quantity – All Electric Range, s. 1.1.2.6. Similar to traditional internal combustion engine vehicles which transform stored chemical energy into mechanical movement, all electric range is limited by the amount of energy available and the ratio that energy is converted into useful work. Within the context of an electrified vehicle powertrain, *battery capacity* (kWh) is the amount of energy available and *electrical efficiency* (mi kWh^{-1}) is the work to energy ratio.

It is of interest to determine the electrical efficiency of modern vehicles to provide context to the simulation results. By using the 2014 fuel economy test results collected by the EPA (Vehicle Comparison and Drive Cycles, s. 1.1.1.3), it is possible to construct a plot of all-electric range (AER) vs. battery capacity (Figure 70). Within Figure 70, the grey and black markers indicate 2014 commercial PHEVs and BEVs respectively, and the average electrical efficiency is indicated by the slope. A larger version of Figure 70, which includes vehicle names, is included in Appendix E – AER for 2014 Vehicles.

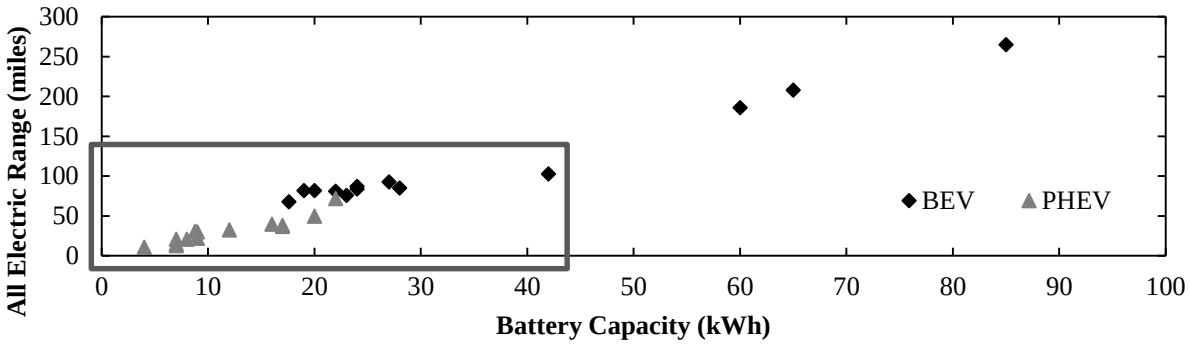

Figure 70: Increasing AER w.r.t. battery capacity for 2014 commercial electrified vehicles

An inspection of vehicles with a battery capacity of 0 to 35 kWh, the enclosed section within Figure 70, reveals an interesting observation – PHEVs display a lower electrical efficiency than BEVs. This enclosed section is enlarged Figure 71. The displayed electrical efficiencies for PHEVs and BEVs, 2.656 and 3.189 mi kWh^{-1} respectively, and differs by approximately 20%. An enlarged version of Figure 71, which includes vehicle names, is included in Appendix E – AER for 2014 Vehicles.

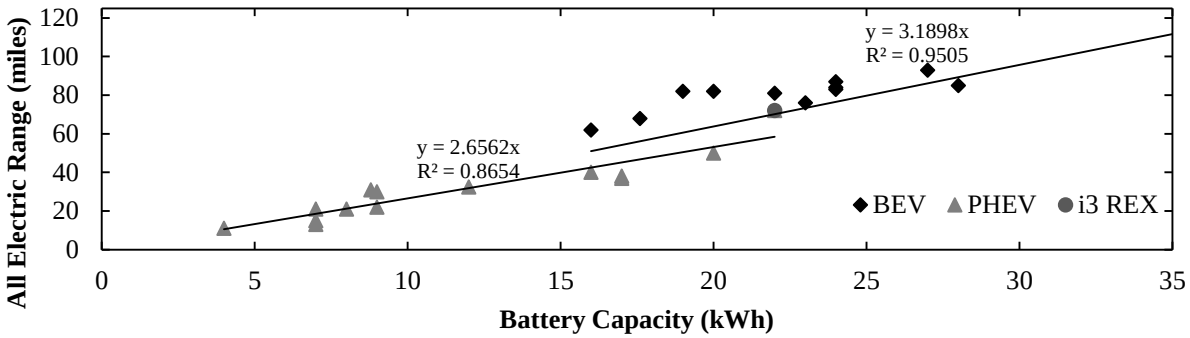

Figure 71: Implied PHEV electrical efficiency deficit

This offset is not caused by the added weight of the ICE powertrain, rather is produced by the PHEV battery controller. When the battery reaches a critical capacity, the vehicle enters charge sustaining (CS) mode to prevent irreparable degradation to the battery. In CS mode the vehicle utilizes the engine, instead of the motor, to avoid discharging the battery below the critical threshold. The critical capacity varies depending on the controller, and values between 10 and 20% maximum capacity are common, and exists to preserve the lifespan of the battery [102] [103] [104] [105] [106] [107]. This control is absent in BEVs, as it is preferable to degrade the battery when the alternative is a motionless vehicle without a secondary resource. Modifying effective battery capacity of PHEVs to account for this control scheme, with an estimated critical capacity of 20%, produces the new PHEV mi kWh^{-1} relationship shown in Figure 72. An enlarged version of Figure 72, which includes vehicle names, is included in Appendix E – AER for 2014 Vehicles.

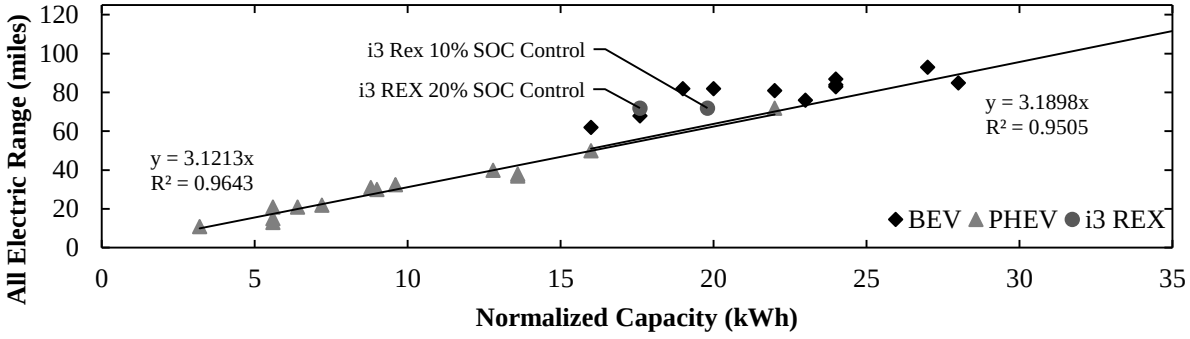

Figure 72: Normalized PHEV battery results in similar trend shown in BEVs

The BMW i3 REX is a PHEV modification of the i3 BEV, and shares the same frame, motor, battery, etc. as the original production car. However the PHEV AER decreases by 11%, instead of the suspected 25%, suggesting that the REX does not utilize the 20% SOC control assumed for the other hybrid vehicles. For this reason, a 10% threshold was assumed for the BMW i3 REX which is in alignment with the other commercial vehicles. It is of interest to clarify that the

i3 REX PHEV would exhibit a greater electrical efficiency than the i3 BEV if a 20% SOC cutoff was used (Table 6).

Table 6: Electrical efficiency of the BMW i3 BEV and i3 REX

Model	Make	Range	Capacity	Critical SOC	Effective Capacity,	Electrical Efficiency
BMW	i3 BEV	81 mi	22 kWh	0%	22.0 kWh	3.68 mi kWh^{-1}
	i3 REX	72 mi	22 kWh	20%	17.6 kWh	4.09 mi kWh^{-1}
				10%	19.8 kWh	3.63 mi kWh^{-1}

The Toyota RAV4 also requires modification. Although RAV4 is a BEV, the battery controller does not fully discharge the battery under normal operation and utilizes an effective capacity of 35 kWh. An average of the normal and full discharge modes was used to determine the reported value [108]. This modification is emphasized in Figure 73.

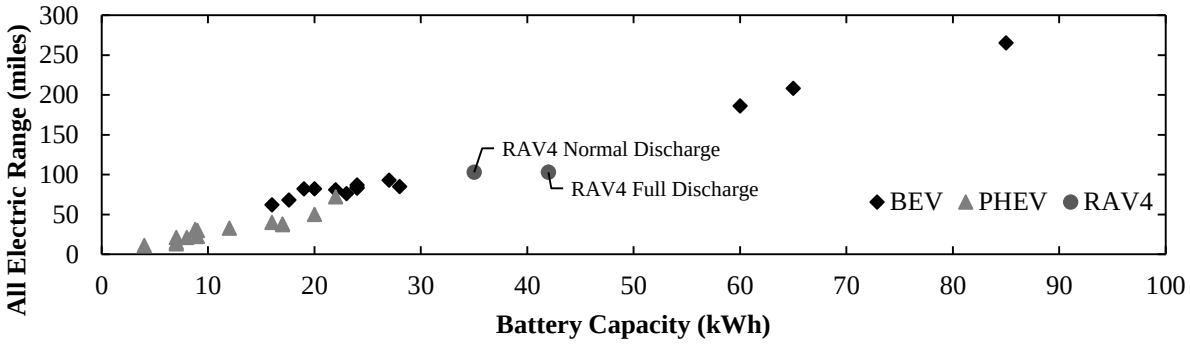

Figure 73: RAV4 effective battery capacity modification

The electrical efficiency of PHEV and BEV vehicle architectures can be shown to be equivalent through a confidence interval assuming a normal distribution. A normal probability plot which supports this assumption, shown by a linear relationship of observed vs. expected values, is included in Appendix E – AER for 2014 Vehicles.

The confidence interval for comparing two means of equal, but unknown, variance is shown in equations 18 – 20. Related values, BEV & PHEV electrical efficiency, standard deviation, variance, and sample population are provided in Table 7.

$$(x_1 - x_2) \pm t_{\frac{\alpha}{2},v} s_p \sqrt{\frac{1}{n_1} + \frac{1}{n_2}} \quad \text{(Eq. 18)}$$

$$s_p^2 = \frac{(n_1-1)s_1^2 + (n_2-1)s_2^2}{v} \quad \text{(Eq. 19)}$$

$$v = n_1 + n_2 - 2 \quad \text{(Eq. 20)}$$

Table 7: BEV and PHEV preliminary statistics

Architecture	Efficiency (x)	Standard Deviation (s)	Variance (s^2)	Population Size (n)
BEV	3.205	0.539	0.290	17
PHEV	3.121	0.385	0.148	14
Pooled	3.199	0.476	0.226	31

BEV and PHEV efficiency can be shown to have equivalent variance through an F-test, with the null and alternate hypotheses H_0: $s_1^2/s_2^2 = 1$ and H_1: $s_1^2/s_2^2 \neq 1$ respectively. The observed and critical F values are provided in Table 8. As $F_{observed}$ is less than $F_{critical}$, the variance between the samples is not statistically significant, and therefore the sample variances may be pooled.

Table 8: Pooled variance F values

Test Statistic	Value
$F_{observed}$	1.9592
$F_{critical}$ ($\alpha = 0.05$)	2.3973

By equation 18, the vehicle efficiencies are shown to be equal by residing within the 95% confidence interval (0.084 ± 0.168). A plot of normalized capacity for all sampled 2014 electrified vehicles is shown in Figure 74. An enlarged version of Figure 74, which includes vehicle names, is included in Appendix E – AER for 2014 Vehicles.

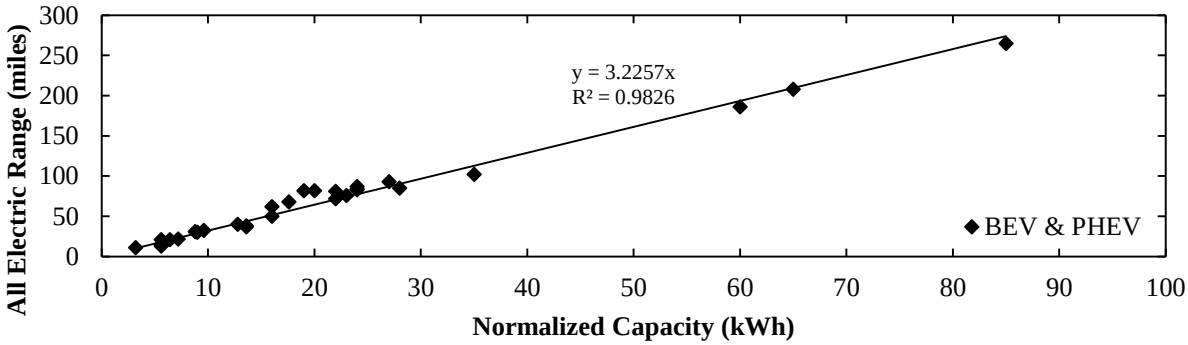

Figure 74: AER vs. normalized capacity for sampled 2014 electrified vehicles

As there are point deviations from the expected electrical efficiency, it is influenced by other factors. This is not surprising, as within the scope of traditional vehicles it is expected the energy required to move a SUV to be exceed that of a sports sedan. Similarly, there are factors that influence the energy required to move different makes of electric vehicles.

Regression analysis was performed to determine the statistical significance of the following vehicle characteristics on electrical efficiency, curb weight (lbs.), drive location (e.g. front),

motor size (kW), and manufacturer suggested retail price ($, USD). Analysis of variance and regression results are provided in Table 9 and Table 10 respectively.

Table 9: Efficiency analysis of variance table

Variable	Degrees of Freedom	Sum of Squares	Mean Square	F Test	Significance
	df	SS	MS	F	P
Regression	4	3.256	0.814	7.235	0.0004
Residual	26	2.925	0.112		
Total	30	6.182			

Table 10: Efficiency regression coefficients

Variable	Coefficient	Std. Error	t-Stat	P-Value
Intercept	4.74826	0.31517	15.06553	0.00000
Curb. Wt.	-0.00037	0.00013	-2.77036	0.01020
Drive	-0.11228	0.08161	-1.37569	0.18065
Motor	0.00144	0.00178	0.81036	0.42509
MSRP	-0.00001	0.00000	-1.97003	0.05957

The regression is significant with a p-value of 0.0004 (Table 9) with a significant parameter: curb weight (Table 10). Brief commentary is provided for each parameter: curb weight, drive, motor size, and manufacturer suggested retail price (MSRP), detailing the significance and implications of the regression results.

Curb weight is a significant parameter with a p-value of 0.0102 (Figure 75). This is expected, as vehicle weight influences dynamometer resistance (Fuel Economy and Energy Loss, s. 1.1.2). Dynamometer resistance is also influenced by drag coefficients, which were not provided, and may offer an explanation for smaller vehicles such as the Honda Fit or Chevrolet Spark as minor outliers. Another explanation is the controller aggressiveness with respect to regenerative breaking or non-uniform critical capacity control values. An enlarged version of Figure 75, which includes vehicle names, is included in Appendix E – AER for 2014 Vehicles.

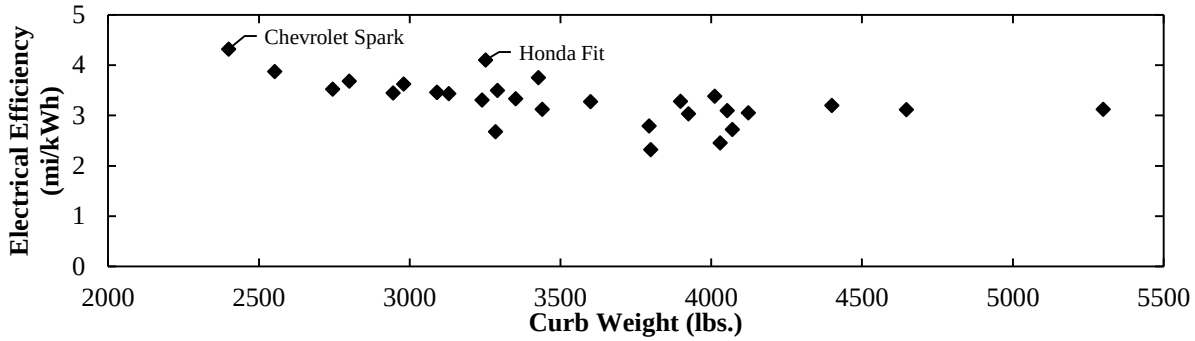

Figure 75: Decreasing efficiency with increasing weight

Drive location is insignificant with a p-value of 0.1806. While front-wheel drive is regarded as more efficient, it is attributed to a decrease in component weight [109]. Therefore, any efficiency gains associated with drive classification are encompassed in the curb weight parameter.

Motor size is insignificant with a p-value of 0.4251. While smaller engines equipped with a turbocharger are more efficient than their larger counterparts [110], the trend is not present within electric motors. Work presented by Zulkifli et al. suggests that size does not influence motor efficiency [111].

MSRP is on the verge of significance with a p-value of 0.0596. However additional analysis with the removal of luxury vehicles (i.e. MSRP exceeding $70,000) yields a regression coefficient of -9.1×10^{-6} with $p = 0.2460$, presenting strong evidence against the relationship. Luxury vehicles, by definition, are limited in number and therefore weigh the regression in favor of correlation. A comforting observation is MSRP exhibits a negative relationship, indicating that if the regression were significant a luxury car is less efficient than a more affordable vehicle.

The electrical efficiency regression results can be related to AER and produce an empirical model through substitution (Eq. 21 – 22). This transformation is preferred over a traditional regression (i.e. $y = b_0 + b_1x_1 + b_2x_2 + b_3x_1x_2$), as it does not assume erroneous relationships (i.e. with the traditional model, a non-zero b_0 would suggest an electric vehicle can travel a constant distance without the aid of a battery pack).

$$\frac{AER}{capacity} = b_1 * weight + b_2 \quad \text{(Eq. 21)}$$

$$AER = capacity(b_1 * weight + b_2) \quad \text{(Eq. 22)}$$

The proposed empirical model was characterized using the normalized vehicle battery capacities (Table 11 & Table 12). There is a high correlation between the model predicted and production vehicle values.

Table 11: Model analysis of variance (ANOVA) table

Variable	Degrees of Freedom	Sum of Squares	Mean Square	F Test	Significance
	df	SS	MS	F	P
Regression	2	257,030	128,515	2,176	$2x10^{-31}$
Residual	29	1,712	59		
Total	31	258,743			

Table 12: Model regression coefficients

Variable	Coefficient	Std. Error	t-Stat	P-Value
Capacity (kWh)	3.141306	0.101947	30.81299	$1x10^{-23}$
Wt.*Capacity (lbs.*kWh)	0.000590	0.000823	0.71665	0.479319

The overall regression ($p = 2x10^{-31}$) and battery capacity coefficient ($p = 1x10^{-23}$) are highly significant. The weight*capacity term displays a p-value of 0.479, indicating that although curb weight is a strong indicator of electrical efficiency, it is insignificant when relative to battery capacity in estimating electrified vehicle all-electric range. Comparing the model R^2 with the capacity-only R^2 statistic (0.9717), it is expected that the weight term would provide little significance (Table 13).

Table 13: Capacity & weight model vs. capacity only comparative regression statistics

Statistic	Model Value	Capacity-Only
R^2	0.9967	0.9717
Adjusted R^2	0.9587	0.9717

The model predicted all-electric ranges are plotted against the reported production vehicle values in Figure 76. There is consistent agreement between the predicted and produced values. An enlarged version of Figure 76, which includes vehicle names, is included in Appendix E – AER for 2014 Vehicles.

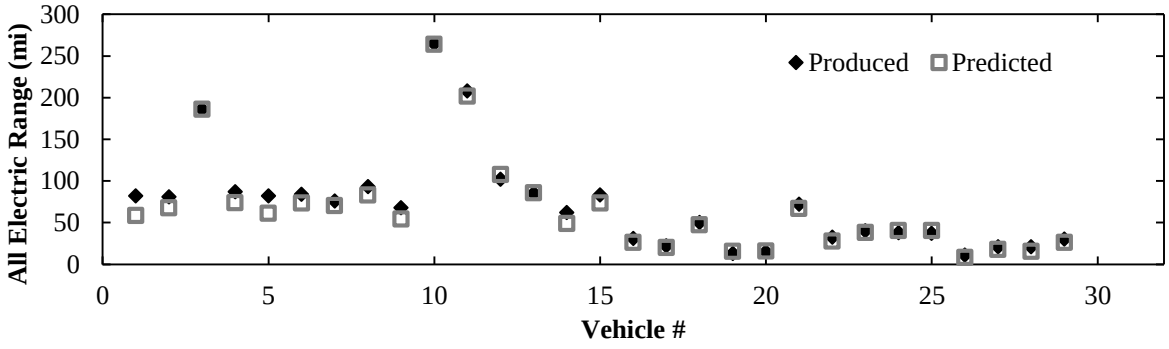

Figure 76: Model predictions vs. produced vehicle all-electric ranges

5 Discussion & Impact on Vehicle Design

It is of interest to determine the significance of modeling the hysteresis effect for the purposes of vehicle design. In this work it is assumed that *the Thevenin model results are representative of cell behavior* which implies that *any difference between the simulated model results can be attributed to the hysteresis effect*. Observations which validate these assumptions can be found in Model Validation and Comparison, s. 2.3.

The Thevenin model is non-ideal, and there is prediction error related to current shifts. Additionally, as the frequency of current shifts increases, the Thevenin model has been shown to be unable to capture all hysteresis effects (Model Validation and Comparison, s. 2.3). It has been shown that the accuracy of the Thevenin model can be improved by adding additional R|C elements in series by He et al. who compared many equivalent circuit models for SOC estimation [53]. An excerpt of He et al.'s work, which relates average prediction error and model relative improvement for each successive R|C element, is provided in Table 14.

Table 14: Relative improvement of R|C elements

# R|C Elements	Model Name	Avg. ΔV (measured – modeled)	Relative Improvement $\left(\frac{R\|C_{\#}\Delta V - R\|C_{\#+1}\Delta V}{R\|C_{\#}\Delta V}\right)$
0	Rint	0.3945	-
1	Thevenin	0.0455	88.46%
2	Dual Polarization	0.0429	5.71%

While it is shown that while a single R|C element is a vast improvement to the Rint model, the effectiveness of successive R|C elements is greatly diminished. Adding the first R|C element, or upgrading from the Rint to the Thevenin model, decreases voltage prediction error by 88.46%. However adding the second R|C element, or upgrading from the Thevenin to the Dual Polarization model, decreases voltage prediction error by only 5.71%.

An inspection of the work by Zhang et al. [56], who compares R-$(R|C)_n$ equivalent circuit models in terms of accuracy and convergence time, suggests that it would be desirable to compare the two most similar models with the greatest prediction improvement. Not only does this assist in the ability to fit equivalent circuit parameters, but isolates the model element that can be attributed with improvement if one is detected (i.e. the difference in the simulation results can be attributed to the R|C element).

The Thevenin ECM is different than the Rint ECM results, indicating that the hysteresis effect does influence vehicle simulations (Simulation Results, s. 3). Furthermore, it does not influence simulations uniformly. In a smooth, low acceleration, drive cycle (UDDS) the impact was small – with a difference in electrical consumption of 2.05 Wh mi^{-1}. In a sustained power demand or aggressive drive cycle (HWFET or US06) the impact was large – with a difference in electrical consumption 31.13 – 34.61 Wh mi^{-1}. Therefore the importance of utilizing more advanced,

hysteresis inclusive, battery models is dependent on the complexity and magnitude of current demands.

A factor that is not easily shown by the simulation results is that the importance of modeling the hysteresis effect is also SOC dependent. As the cell discharges, the magnitude of hysteresis gradually increases as shown in Figure 77. This trend can also be seen in Figure 56 (s. 2.2.3) which indicates the Thevenin hysteresis modeling components, resistor R_2 and capacitor C_1, have increased influence at lower SOCs. This has increased significance for plug-in hybrid vehicles which operate at low SOCs for extended periods during charge sustaining operation. It may also be applicable to vehicle controllers and related coulomb counting operations.

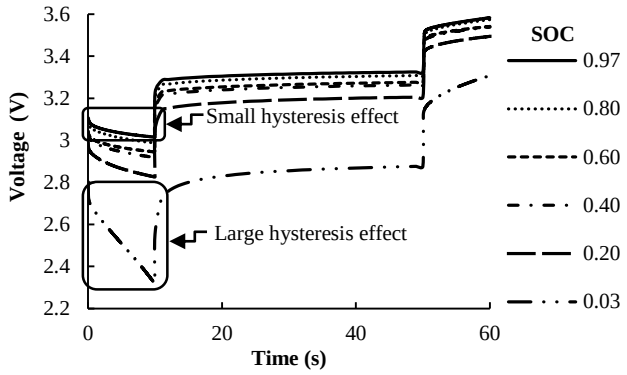

Figure 77: Commercial $LiFePO_4$ battery HPPC voltage response at different SOCs

Applying the EPA fuel economy weighting of the UDDS and HWFET drive cycles yields an average electrical consumption increase of 15.136 Wh mi^{-1}. In the context of the average 2014 electrified vehicle electrical efficiency of 3.225 mi kWh^{-1} (Effect of Electrical Losses on Range, s. 4), a decrease in electrical consumption of 15.136 Wh mi^{-1} during the simulation stage would estimate an electrical efficiency of 3.391 mi kWh^{-1}, or a 5.1% increase from the actual value!

The importance of using the Thevenin over the Rint model depends on the drive cycle. For "stop and go" traffic with low current demands, the Rint model provides comparable results. However, for high acceleration traffic or high current demands, the Thevenin model provides increased accuracy. The Rint model is estimated to over-predict all-electric range by over 5% when compared to the Thevenin model in the context of 2014 electrified vehicles.

6 Conclusions

The Thevenin equivalent circuit model was imported into Autonomie vehicle modeling software. It was used, in combination with the Rint model, to estimate the impact of the lithium-ion battery hysteresis effect on simulated vehicles. The creation of an Autonomie based Thevenin equivalent circuit model was completed in three independent processes: collection of commercial battery data, equivalent circuit model characterization, and software import.

The UDDS and US06 current profiles were generated as a byproduct of previous work, which modified Autonomie Rint model initialization file parameters to estimate the effect of temperature on electric vehicle range [95]. A commercial lithium iron phosphate (LFP) battery was cycled with these simulated drive cycle current profiles and a scaled hybrid pulse power characterization (HPPC) test profile (Experimental, s. 2).

The Rint and Thevenin models were characterized using the scaled HPPC test profile using a generalized reduced gradient (GRG) algorithm. Trapezoidal approximation for small time steps was used for the integral term within the Thevenin model to relate the current across the resistor and capacitor elements to the total current (Thevenin Model, s. 1.3.1). The "sum of absolute differences" method was used in place of the popular "sum of squares" method to decrease model prediction error (Circuit Parameter Characterization, s. 2.2.2).

The stepwise Thevenin model was then imported into Autonomie vehicle modeling software (Appendix B – Thevenin Simulink Model). Reference files were created that enabled Autonomie to operate the new model, previously unavailable within the workspace. Initialization files, representative of the characterized parameters, were then created for both the Rint and Thevenin equivalent circuit models (Appendix C – Rint Autonomie Code & Appendix B – Thevenin Simulink Model). This fulfilled all requirements to model the hysteresis effect within Autonomie software.

Simulations were performed using a generic battery electric vehicle (Appendix A – Simulated BEV Powertrain). The only modification to the vehicle defaults were the aforementioned changes to the energy storage system (ess) to utilize the Rint and Thevenin models and related initialization files. This composed two otherwise identical vehicles with different battery models. These vehicles were used to complete simulation trials of the UDDS, HWFET, and US06 drive cycles (Simulation Results, s. 3)

The Thevenin model predicts an increased electrical consumption of 2.05, 31.13, and 34.61 Wh mi^{-1} across the simulated drive cycles UDDS, HWFET, and US06 respectively. Additional analysis was performed to relate the effects of increased electrical consumption to modern electrified vehicles (Effect of Electrical Losses on Range, s. 4). The increase in electrical consumption is relative to the complexity of the drive cycle current demand, and directly related to the modeled hysteresis effect. Accurate modeling of the hysteresis effect is of interest to

automotive engineers where high current profiles are present, such as high way or aggressive driving, or high accuracy is required, such as coulomb counting or SOC estimation (Discussion & Impact on Vehicle Design, s. 5)

7 Recommendations

The following recommendations are suggested with reference to future researchers or innovators who wish to continue this work: expand characterized Thevenin model parameters to include a range of temperatures, characterize model parameters with drive cycle current profiles in place of the hybrid pulse power characterization (HPPC) test, and to implement more advanced equivalent circuit models into the Autonomie workspace.

Expanding the characterized Thevenin parameters is the easiest of these tasks, as no modifications to the source code are required. Although this work does not consider thermal effects and assumes a constant temperature of 23 °C, indexes were written with consideration to future work and it will be relatively simple to add thermal indexing to the existing model. As temperature has been shown to influence electrical consumption, it would be an interesting study to determine the effects of temperature on vehicle range with reference to hysteresis effects [95].

By characterizing model parameters with drive cycle current profiles instead of the HPPC test, additional insight may be gained regarding model nature. For example, if the Thevenin and Rint model parameters were characterized using a current profile representative of the HWFET drive cycle instead of the HPPC test, it would be expected that their simulation results would align more closely. Furthermore, it would be an interesting study to determine how closely the HPPC derived parameters align with the drive cycle current derived parameters. This analysis was originally intended to be included in this work, but was omitted due to complications regarding the SOC parsing of drive cycle data. It is strongly recommended that the drive cycle trials be collected in 10% SOC increments rather than full discharge cycles. The latter introduces non-uniform current profiles for each SOC interval, and renders parameter characterization impossible.

While the hysteresis effect was shown to be significant in vehicle simulation by use of the Thevenin model in this work, the extent to which it is significant was not. More complex battery models which include additional resistor-capacitor (R|C) elements have been shown to be better estimators of voltage than the Thevenin model (Discussion & Impact on Vehicle Design, s. 5).While it is expected that the increase in model accuracy will have limited influence on simulation results based on prior work [53] [56], this has not been proven within the context of a comprehensive vehicle model.

A recommendation that is related to, but tangential, to this work is to incorporate electrochemical impedance spectroscopy (EIS) into the characterization of model parameters alongside the hybrid pulse power characterization (HPPC) test. While the HPPC test is sufficient for relatively simple models, such as the Rint and Thevenin models, it becomes difficult to distinguish different electrochemical phenomena. With EIS, it is possible to isolate and identify these phenomena with alternating current, but it becomes difficult to infer the extent they influence a voltage response under direct current applications [58]. Therefore each method provides

validation for the shortcomings of the other: alternating current (EIS) provides insight to phenomena otherwise invisible to HPPC, and direct current (HPPC) provides justification regarding the existence of the phenomena and their significance. As low frequency alternating current approximates direct current, it is suspected that witnessed phenomena at low frequencies pose greater significance relative to high frequencies [101].

References

[1] Queen's Printer for Ontario, "Ontario Paves Way for Electric Vehicles," 18 June 2010. [Online]. Available: http://news.ontario.ca/mto/en/2010/06/ontario-paves-the-way-for-electric-vehicles.html. [Accessed 17 March 2014].

[2] E. Loveday, "Quebec to Offer Plug-In Vehicles Rebates of up to $8000," 11 April 2011. [Online]. Available: http://green.autoblog.com/2011/04/11/quebec-offer-plug-in-vehicle-rebates-8000-dollars/. [Accessed 17 March 2014].

[3] British Columbia Press, "Clean Energy Vehicle Program," 5 November 2011. [Online]. Available: http://www.livesmartbc.ca/incentives/transportation/. [Accessed 17 March 2014].

[4] California Center for Sustainable Energy, "Clean Vehicle Rebate Project," 2014. [Online]. Available: http://energycenter.org/programs/clean_vehicle_rebate_project. [Accessed 17 March 2014].

[5] Edmunds, "China Announces Plan to Substidize EVs and Plug-In Hybrids in Five Major Cities," 1 June 2010. [Online]. Available: http://www.edmunds.com/whats-hot/. [Accessed 17 March 2014].

[6] P. Hudson, "£5,000 grant to buy plug-in electric cars," 28 Feb 2010. [Online]. Available: http://www.telegraph.co.uk/motoring/green-motoring/7316351/5000-grant-to-buy-plug-in-electric-cars.html. [Accessed 17 March 2014].

[7] J. Blau, "Berlin Plugs In Electric Mobility Strategy," 3 May 2010. [Online]. Available: http://www.dw.de/berlin-plugs-in-electric-mobility-strategy/a-5533192-1. [Accessed 17 March 2014].

[8] J. Cobb, "Top 6 Plug-In Vehicle Adopting Countries," 16 January 2014. [Online]. Available: http://www.hybridcars.com/top-6-plug-in-car-adopting-countries/. [Accessed 17 March 2014].

[9] PNGV, "Partnership for a New Generation of Vehicles, assessment of program goals, activities, and priorities: hearing before the Subcommittee on Energy and Environment of the Committee on Science, U.S. House of Representatives, One Hundred Fourth Congress," 30 July 1996. [Online]. Available: https://openlibrary.org/books/OL736165M/Partnership_for_a_New_Generation_of_Vehicles_(PNGV). [Accessed 2 December 2014].

[10] Board on Energy and Enviromental Systems, Division on Engineering and Physical Sciences, Transportation Research Board and National Research Council, "Review of the Research Program of the Partnership for a New Generation of Vehicles, Seventh Report," National Academy Press, Washington, D.C., 2001.

[11] R. A. Kost, "New Concept Cars Demonstrate Clean, Efficient Transportation Technologies," April 2001. [Online]. Available: www1.eere.energy.gov/vehiclesandfuels/pdfs/success/pngv3_23_01.pdf. [Accessed 15 January 2014].

[12] A. Little, "What can we learn from Bush's FreedomCar Plan?," 23 February 2003. [Online]. Available: http://grist.org/article/tough/. [Accessed 1 January 2014].

[13] Department of Energy, "Fiscal Year 2010 Budget-In-Brief," U.S. Department of Energy, Washington, D.C., 2009.

[14] Environmental Protection Agency, "New Fuel Economy and Environment Labels for a New Generation of Vehicles," May 2011. [Online]. Available: http://www.epa.gov/carlabel/420f11017.pdf. [Accessed 16 January 2014].

[15] Environmental Protection Agency, "A New Generation of Labels for a New Generation of Vehicles," Environmental Protection Agency, 30 July 2013. [Online]. Available: http://www.epa.gov/carlabel/index.htm. [Accessed 16 January 2014].

[16] EPA, "Fuel Economy," U.S. Department of Energy, 1 March 2015. [Online]. Available: http://www.fueleconomy.gov/. [Accessed 1 April 2015].

[17] Environmental Protection Agency, "U.S. Government Publishing Office," 1 July 2012. [Online]. Available: http://www.gpo.gov/fdsys/granule/CFR-2012-title40-vol34/CFR-2012-title40-vol34-part1066. [Accessed 27 May 2015].

[18] UNITED STATES ENVIRONMENTAL PROTECTION AGENCY, "Determination and Use of Vehicle Road-Load Force and Dynamometer Settings," Department of Energy, Ann Arbor, 2015.

[19] National Resources Canada, "Fuel Consumption Testing," Government of Canada, 10 March 2015. [Online]. Available: http://www.nrcan.gc.ca/energy/efficiency/transportation/cars-light-trucks/buying/7491. [Accessed 5 July 2015].

[20] U.S. Environmental Protection Agency, "Dynameter Drive Schedules," 6 February 2013. [Online]. Available: http://www.epa.gov/nvfel/testing/dynamometer.htm#vehcycles. [Accessed 15 January 2014].

[21] Pollution Probe, CAA, "Primer on Automotive Fuel Efficiency and Emissions," Pollution Probe, Toronto, 2009.

[22] R. V. Gopal and A. Rousseau, "System Analysis Using Multiple Expert Tools," *SAE International*, vol. 01, p. 0754, 2011.

[23] N. Lutsey, "A Technical Analysis of Model Year 2011 US Automotive Industry," *Transportation Research Part D*, vol. 17, pp. 361-369, 2012.

[24] U.S. Department of Energy, "Engine Energy Use: Where Does the Energy Go?," U.S. Department of Energy, 9 January 2012. [Online]. Available: http://www1.eere.energy.gov/vehiclesandfuels/facts/m/2012_fotw709.html. [Accessed 10 January 2004].

[25] Thermal Demon Co., "Prius Presentation," [Online]. Available: http://www.thermal.demon.co.uk/Prius%20Presentation%202/Slide%208a.htm. [Accessed 2 December 2014].

[26] M. Kopac and L. Kokturk, "Determination of optimum speed of an internal combustion engine by exergy analysis," *International Journal of Exergy*, vol. 2, no. 1, pp. 40 - 54, 2005.

[27] K. Rajashekara, "Power Electronics and Control for Hybrid and Fuel Cell Vehicles," in *Handbook of Automotive Power Electronics and Motor Drives*, Boca Raton, CRC Press, 2005, p. 347.

[28] I. Husain, Electric and Hybrid Vehicles Design Fundamentals, Boca Raton: CRC Press, 2003.

[29] visaotecnica, visaotecnica, 07 January 2011. [Online]. Available: http://f1visaotecnica.files.wordpress.com/2011/07/mapa.jpg. [Accessed 10 January 2014].

[30] Q. Zhang, X. Liu, S. Chu, S. Dong and Y. Yu, "Hybrid Switched Reluctance Motor and Drives Applied on a Hybrid Electric Car," in *Electric Vehicles - Modelling and Simulations*, InTech, 2011.

[31] EVmuseum, "EV Museum," EV Museum, September 2014. [Online]. Available: http://evmuseum.com/EV1_images.html. [Accessed 3 December 2014].

[32] C. Paglee, "Why battery electric vehicles will beat fuel cells," Green Autoblog, 5 August 2014. [Online]. Available: http://green.autoblog.com/2014/08/05/why-battery-electric-vehicles-will-beat-fuel-cells/. [Accessed 15 December 2014].

[33] A. Ingram, "Toyota Accelerates Switch To Lithium-Ion Batteries, Still Lags Others," Green Car Reports, 20 May 2013. [Online]. Available: http://www.greencarreports.com/news/1084281_toyota-accelerates-switch-to-lithium-ion-batteries-still-lags-others. [Accessed 15 December 2014].

[34] J.-M. Tarascon and M. Armand, "Issues and challenges facing rechargeable lithium batteries," *Nature,* no. 414, pp. 359-367, 2001.

[35] U.S. Department of Energy, "Alternative Fuels Data Center - Fuel Properties Comparison," [Online]. Available: http://www.afdc.energy.gov/fuels/fuel_comparison_chart.pdf. [Accessed 11 December 2014].

[36] C. Mikolajczak, M. Kahn, K. White and R. T. Long, "Lithium-Ion Batteries Hazard and Use Assessment," The Fire Protection Research Foundation, Quincy, 2011.

[37] M. Thiessen, "Lightweight Energy Storage," National Geographic, 10 December 2010. [Online]. Available: http://news.nationalgeographic.com/news/energy/2010/12/photogalleries/101210-bolivia-salt-flats-pictures-lithium-batteries-energy-climate/#/energy-lithium-salt-desert-bolivia-battery_30245_600x450.jpg. [Accessed 13 November 2013].

[38] International Standard, "Lumos," 2003-2012. [Online]. Available: http://www.cnlumos.com/lumos/Battery%20Knowledge/Battery%20Standards/IEC%2061960-2003.pdf. [Accessed 12 November 2013].

[39] The Boston Consulting Group, "Boston Consulting Group Documents," 2010. [Online]. Available: http://www.bcg.com/documents/file36615.pdf. [Accessed 3 March 2014].

[40] M. N. Obrovac, L. Christensen, B. L. Li and J. R. Dan, "Alloy Design for Lithium-Ion Battery Anodes," *Journal of The Electrochemical Society*, vol. 154, no. 9, pp. A849-A855, 2007.

[41] J. O. Besenhard, J. Yang and M. Winter, "Will advanced lithium-alloy anodes have a chance in lithium-ion batteries?," *Journal of Power Sources,* vol. 68, pp. 87-90, 1997.

[42] J. Dahn, "Why Do Li-ion Batteries Die? and how to improve the situation?," Dalhousie University, Waterloo, 2013.

[43] G. Cherkashinin, K. Nikolowski, H. Ehrenberg, S. Jacke, L. Dimesso and W. Jaegermann, "The stability of the SEI layer, surface composition and the oxidation state of transition metals at the electrolyte–cathode interface impacted by the electrochemical cycling: X-ray photoelectron spectroscopy investigation," *Physical Chemistry Chemical Physics,* no. 35, p. 12325, 2012.

[44] E. P. Roth, C. C. Crafts, D. H. Doughty and J. McBreen, "Advanced Technology Development Program for Lithium-Ion Batteries: Thermal Abuse Performance of 18650 Li-Ion Cells," Sandia, Albuquerque, 2004.

[45] NASA, "Limitations of Internal Protective Devices in High-Voltage/High-Capacity Batteries Using Lithium-Ion Cylindrical Commercial Cells," 09 2002. [Online]. Available: http://www.nasa.gov/pdf/345992main_NESC%20TB%2009-02_Li%20Ion%20Battery%20Limitatations.pdf. [Accessed 14 November 2013].

[46] IBT Power Ltd., "Lithium Ion Technical Data," IBT Power, 2012. [Online]. Available: http://www.ibt-power.com/Battery_packs/Li_Ion/Lithium_ion_tech.html. [Accessed 22 October 2013].

[47] S. Blanco, "Chevy Volt replacement battery cost varies wildly, up to $34,000," autobloggreen, 10 January 2014. [Online]. Available: http://green.autoblog.com/2014/01/10/chevy-volt-battery-replacement-cost-34000/. [Accessed 4 December 2014].

[48] L. Cheah and J. Heywood, "The Cost of Vehicle Electrification: A Literature Review," 8 April 2010. [Online]. Available: http://web.mit.edu/sloan-auto-lab/research/beforeh2/files/PHEV%20costs.pdf. [Accessed 4 December 2014].

[49] Argonne Nation Laboratory, "Autonomie," U.S. Department of Energy, [Online]. Available: http://www.autonomie.net/overview/index.html. [Accessed 26 October 2014].

[50] K. Young, C. Wang, L. Y. Wang and K. Strunz, "Electric Vehicle Technologies," in *Electric Vehicle Integration into Modern Power Networks*, New York, Springer Scientific, 2013, pp. 1-43.

[51] R. Rao, S. Vrudhula and D. N. Rakhmatov, "Battery Modeling for Energy Aware System Design," *Computer,* vol. 36, no. 12, pp. 77-87, 2003.

[52] A. Seaman, T.-S. Dao and J. McPhee, "A Survey of Mathematics-Based Equivalent-Circuit and Electrochemical Battery Models for Hybrid and Electric Vehicle Simulation," *Journal of Power Sources,* vol. 256, pp. 410-423, 2014.

[53] H. He, R. Xiong and J. Fan, "Evaluation of Lithium-Ion Battery Equivalent Circuit Models for State of Charge Estimation by an Experimental Approach," *Energies,* vol. 4, pp. 582-598, 2011.

[54] Department of Energy Vehicle Technologies Program, "Battery Test Manual For Plug-In Hybrid Electric Vehicles," The Idaho National Laboratory is a U.S. Department of Energy National Laboratory, Idaho Operations Office, 2008.

[55] H. Wu, S. Yuan and C. Yin, "Online State of Charge Estimation Based o Adaptive Extended Kalman Filter and Linear Parameter-Varying model with Recursive Least Squares Technique," 2013. [Online]. Available: http://engine.lib.uwaterloo.ca/ojs-2.2/index.php/pptvt/article/viewFile/663/236. [Accessed 25 November 2014].

[56] H. Zhang and M.-Y. Chow, "Comprehensive Dynamic Battery Modeling for PHEV Applications," in *Power and Energy Society General Meeting, 2010 IEEE*, Minneapolis, 2010.

[57] E. Samadani, L. Gimenez, W. Scott, S. Farhad, M. Fowler and R. Fraser, "Thermal Behavior of Two Commercial Li-Ion Batteries for Plug-in Hybrid Electric Vehicles," *SAE International,* 2014.

[58] E. Samadani, S. Farhad, W. Scott, M. Mastali, L. Paez, M. Fowler and R. Fraser, "Empirical Modeling of Lithium-ion Batteries Based on Electrochemical Impedance Spectroscopy Tests," *Electrochemica Acta,* vol. 160, pp. 169-177, 2015.

[59] X. Wang, Q. Xiang, B. Liu, L. Wang, T. Luo, D. Chen and G. Shen, "TiO2 modified FeS Nanostructures with Enhanced Electrochemical Performance for Lithium-Ion Batteries," *Nature,* 2013.

[60] V. H. Johnson, "Battery performance models in ADVISOR," *Journal of Power Sources,* vol. 110, pp. 321-329, 2002.

[61] S. S. Zhang, K. Xu and T. R. Jow, "Electrochemical impedance study on the low temperature of Li-ion batteries," *Electrochemica,* vol. 49, pp. 1057-1061, 2004.

[62] H. Ma, S. Chen, L. Niu, S. Zhao, S. Li and D. Li, "Inhibition of Copper Corrosion by Several Schiff Bases in Aerated Halide Solutions," *Journal of Applied Electrochemistry,* vol. 32, pp. 65-72, 2002.

[63] M. Mohamedi, D. Takahashi, I. Itoh and I. Uchida, "Electrochemical Stability of Thin Film LiMn2O4 Cathode in Organic Electrolyte Solutions with Different Compositions at 55 C," *Electrochemica Acta,* vol. 47, no. 21, pp. 3483 - 3489, 2002.

[64] K. Dokko, M. Mohamedi, M. Umeda and I. Uchida, "Kinetic Study of Li-Ion Extraction and Insertion at LiMn2O4 Single Particle Electrodes Using Potential Step and Impedance Methods," *Journal of Electrochemical Society,* vol. 150, no. 4, pp. A424 - A429, 2003.

[65] D. J. Aurbach, "Review of selected electrode–solution interactions which determine the performance of Li and Li ion batteries," *Journal of Power Sources,* vol. 89, no. 2, pp. 206-218, 2000.

[66] J. Newman and W. Tiedemann, "Porous-Electrode Theory with Battery Applications," *AIChE,* vol. 21, pp. 25-41, 1975.

[67] T. F. Fuller, M. Doyle and J. Newman, "Simulation and Optimization of the Dual Lithium Ion Insertation Cell," *Journal of the Electrochemical Society,* vol. 141, pp. 1 - 10, 1994.

[68] C. Y. Wang, W. B. Gu and B. Y. Liaw, "Micro-Macroscopic Coupled Modeling of Batteries and Fuel Cells, Part I: Model Development," *Journal of the Electrochemical Society,* vol. 145, pp. 3407 - 3417, 1998.

[69] C. Y. Wang, W. B. Gu and B. Y. Liaw, "Micro-Macroscopic Coupled Modeling of Batteries and Fuel Cells: Part II: Applications to Ni-Cd and Ni-MH Cells," *Journal of the Electrochemical Society,* vol. 145, pp. 3418 - 3427, 1998.

[70] W. B. Gu and C. Y. Wang, "Thermal and Electrochemical Coupled Modeling of a Lithium-Ion Cell," *Journal of the Electrochemical Society,* vol. 99, pp. 748 - 762, 2000.

[71] P. Ramadass, B. Haran, P. M. Gromadam, R. White and B. N. Popov, "Development of First Principles Capacity Fade Model for Li-Ion Cells," *Journal of the Electrochemical Society,* vol. 151, pp. A196 - A203, 2004.

[72] G. Sikha, B. N. Popov and R. E. White, "Effect of Porosity on the Capacity Fade of a Lithium-Ion Battery," *Journal of the Electrochemical Society,* vol. 151, pp. A1104 - A1114, 2004.

[73] G. Sikha, R. E. White and B. N. Popov, "A Mathematical Model for a Lithium-Ion Battery/Electrochemical Capacitor Hybrid System," *Journal of The Electrochemical Society,,* no. A1682-A1693, p. 152, 2005.

[74] K. Smith, C. D. Rahn and C. Y. Wang, "Control Oriented 1D Electrochemical Model of Lithium Ion Battery," *Energy Convers. Manage.,* vol. 48, pp. 2565 - 2578, 2007.

[75] B. S. Haran, B. N. Popov and R. E. White, "Determination of the Hydrogen Diffusion Coefficient in Metal Hydrides by Impedance Spectoscopy," *Journal of Power Sources,* vol. 75, pp. 56 - 63, 1998.

[76] T. D. Finley, "Battery Degradation Modeling for Vehicle Applications," The University of Waterloo, Waterloo, 2014.

[77] D. Dees and Argonne National Laboratory, "Electrochemistry Cell Model," Argonne National Labs, Washington D.C., 2009.

[78] M. Ebner, F. Marone, M. Stampanoni and V. Wood, "Visualization of Quantification of Electrochemical and Mechanical Degradation in Li Ion Batteries," *Science,* vol. 342, no. 6159, pp. 716-720, 2013.

[79] J. C. Forman, S. Dashash, J. Stein and H. Fathy, "Reduction of an Electrochemistry-Based Li-Ion Battery Health Degradation Model via Constraint Linearization and Pade Approximation," in *ASME 2010 Dynamic Systems and Control Conference, Volume 2*, Cambridge, Massachusetts, USA, 2010.

[80] M. Farkhondeh and C. Delacourt, "Mathematical Modeling of Commercial LiFePO4 Electrodes Based on Variable Solid-State Diffusivity," *Journal of the Electrochemical Society,* vol. 159, no. 2, pp. A177-A192, 2012.

[81] M. Farkhondeh, M. Safari, M. Pritzker, M. Fowler, T. Han, J. Wang and C. Delacourt, "Full-Range Simulation of a Commercial LiFePO4 Electrode Accounting for Bulk and Surface Effects: A Comparative Analysis," *Journal of the Electrochemical Society,* vol. 161, no. 3, pp. A201-A212, 2014.

[82] M. Safari, M. Farkhondeh, M. Pritzker, M. Fowler, T. Han and S.-k. Chen, "Simulations of lithium iron phosphate lithiation/delithiation: Limitations of the core-shell model," *Electrochemica Acta,* 2013.

[83] M. M. Majadabadi, S. Farhad, M. Farkhondeh, R. A. Fraser and M. Fowler, "Simplified electrochemical multi-particle model for LiFePO4 cathodes in lithium-ion batteries," *Journal of Power Sources,* 2014.

[84] M. Farkhondeh, M. Pritzker, M. Fowler, M. Safari and C. Delacourt, "Mesoscopic modeling of Li insertion in phaseseparating electrode materials: application to lithium iron phosphate," *Royal Society of Chemistry,* vol. 16, pp. 22555-22565, 2014.

[85] Z. Mao, F. Mohammad, M. Pritzker, M. Fowler, Z. Chen and M. Safari, "Model-Based Prediction of Composition of an Unknown Blended Lithium-Ion Battery Cathode," *Journal of the Electrochemical Society,* vol. 162, no. 4, pp. A716-A721, 2015.

[86] D. Kray and D. U. Sauer, "Neuro-Methoden zur Prognose und Fehler-erkennung durch Analyse vor Daten aus Monitoring-Systemen," in *Internationales Sonnenforum*, Koln, 1998.

[87] M. Stoll, "Ein Schatzverfahren uber den inneren Zustand geschlossener Bleiakkumulatoren," *VDI Fortschritt-Berichte,* vol. 21, no. 167, 1994.

[88] C. Ehret, S. Piller, W. Schroer and A. Jossen, "State of charge determination for lead-acid batteries in PV-applications," in *16th European Photovoltaic Solar Energy Conference*, Glasgow, 2000.

[89] S. Pillar, M. Perrin and A. Jossen, "Methods for state-of-charge determination and their applications," *Journal of Power Sources,* vol. 96, pp. 113-120, 2001.

[90] J. Alzieu, H. Smimite and C. Glaize, "Improvement of intelligent battery controller: state-of-charge indicator and associated functions," *Journal of Power Sources,* vol. 67, pp. 157-161, 1997.

[91] N. Kim, A. Rousseau and E. Rask, "Autonomie model validation with test data for 2010 Toyota Prius," *SAE International,* vol. 1, no. 1040, 2012.

[92] Autonomie, "Validation," Argonne National Laboratory, 2013. [Online]. Available: http://www.autonomie.net/overview/papers_validation.html. [Accessed 2 January 2014].

[93] C. J. Murray, "Automakers Opting for Model-Based Design," *Design News,* 5 November 2010.

[94] Autonomie, "Vehicle Modeling Approaches," Argonne National Labs, 2013. [Online]. Available: http://www.autonomie.net/references/vehicle_mods_25.html. [Accessed 31 Decemeber 2013].

[95] J. Lo, "Effect of Temperature on Lithium-Iron Phosphate Battery Performance and Plug-in Hybrid Electric Vehicle Range," University of Waterloo, Waterloo, 2013.

[96] G. L. Paez, *Personal Discussion,* Waterloo, 2014.

[97] Maccor, *Maccor Battery & Test Equipment, 4200 Series Startup,* Tulsa: Maccor, 2012.

[98] Cincinnati Sub-Zero, *Installation Operation Maintenance Manual MicroClimate - Series,* Cincinnati: Sub-Zero, 2011.

[99] National Instruments, "LabView Design Software," 2014. [Online]. Available: ni.com/labview. [Accessed 26 October 2014].

[100] D. Jay and F. Nicholas, Applied Statistics for Engineers and Scientists, Belmont, CA: Thomson, 2005.

[101] W. Scott, "Comparison of Equivalent Circuit Model Parameters Derived from AC and DC Sources," in *64th Canadian Chemical Engineering Conference*, Niagara Falls, 2014.

[102] G. M. Bhutto, B. Bak-Jensen and P. Mahat, "Modeling of the CIGRE Low Voltage Test Distribution Network and the Development of Appropriate Controllers," *International Journal of Smart Grid and Clean Energy,* pp. 184 - 191, 2012.

[103] W. Zhang, D. Dong, I. Cvetkovic, F. C. Lee and D. Boroyevich, "Lithium-based Energy Storage Management for Dc Distributed Renewable Energy System," *IEEE,* pp. 3270 - 3277, 2011.

[104] J. Smart and S. Schey, "Battery Electric Vehicle Driving and Charging Behavior," *SAE International ,* vol. 1, no. 1, pp. 27-33, 2012.

[105] B. Lunz, Z. Yan, J. B. Gerschler and D. U. Sauer, "Influence of Plug-in Hybrid Electric Vehicle Charging Strategies on Charging and Battery Degradation Costs," *Energy Policy,* vol. 46, pp. 511 - 519, 2012.

[106] R. T. Doucette and M. D. McCulloh, "Modeling the prospects of plug-in hybrid electric vehicles to reduce CO2 emissions," *Applied Energy,* vol. 88, pp. 2315 - 2323, 2011.

[107] D. Wu, K. T. Chau, C. Liu, S. Gao and F. Li, "Transient Stability Analysis of SMES for Smart Grid With Vehicle-to-Grid Operation," *IEEE TRANSACTIONS ON APPLIED SUPERCONDUCTIVITY,* vol. 22, no. 3, 2012.

[108] D. Good, "Download Fuel Economy Data - 2014 Data File," EPA, Ann Arbor, 2014.

[109] J. Kenwright, "Driving Wheels - Front, Rear or All-Wheel Drive?," Car Sales, 15 April 2010. [Online]. Available: http://www.carpoint.com.au/advice/2010/driving-wheels--front-rear-or-allwheel-drive-7382.

[110] L. Webster, "Top 5 Turbocharger Tech Innovations," Hearst Communications, Inc., 30 September 2009. [Online]. Available: http://www.popularmechanics.com/cars/how-to/a12765/4306310/.

[111] S. A. Zulkifli, S. Mohd, N. Saad and R. A. Aziz, "Influence of Motor Size and Efficiency on Acceleration, Fuel Economy, and Emissions of Split-Parallel Hybrid Electric Vehicle," in *2013 IEEE Symposium on Industrial Electronics & Applications*, Kuching, Malaysia, 2013.

[112] W. Scott, "Thermal Behavior of Two Commercial Li-ion Batteries for Plug-in Hybrid Electric Vehicles," in *SAE World Congress*, Detroit, 2014.

[113] P. Ellsworth, W. Scott, M. Fowler, R. Fraser, B. Gaffney and V. Daniel, "Internal Resistance Optimization Utilizing “Just in Time” Control," *SAE International,* 2015.

[114] E. Samadani, L. G. Paez, W. Scott, S. Farhad, M. Fowler and R. Fraser, "Thermal Behavior of Two Commercial Li-Ion Batteries for Plug-in Hybrid Electric Vehicles," *SAE International,* 2014.

Appendix A – Simulated BEV Powertrain

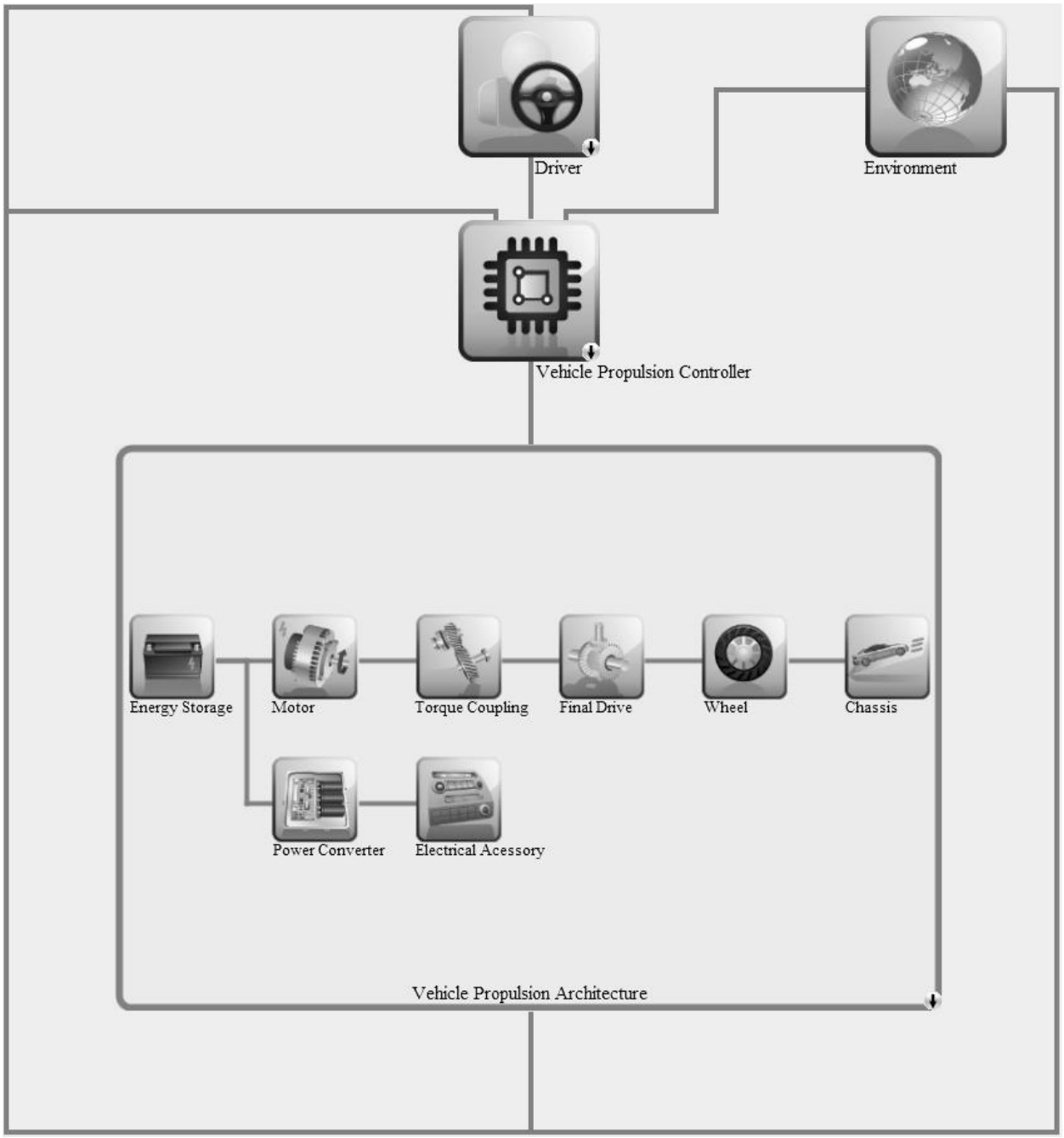

P. Train Element	Component	File Type	File Name
Energy Storage	Controller	Model	ess_ctrl_Thevenin_map ess_ctrl_generic_map
	Plant	Model	Thevenin Model - WWS Battery Model with Open Circuit Voltage, Charge and Discharge resistance
		Initialization	ess_plant_li_LFP_A123_UWAFT.m
		Pre-Processing	ess_plant_preproc.m
		Post Processing	ess_postprocess, ess_state_scalar_postprocess, ess_state_signal_postprocess, ess_summary_postprocess
Motor	Controller	Configuration	ctrl_with_cstr_cmd
	Constraint B.	Model	mot_ctrl_cstr_map_Pelec_funTW_volt_in
	Command B.	Model	mot_ctrl_cmd_map_Pelec_funTW_volt_in_no_trs
	Plant	Model	mot_plant_map_Pelec_funTW_volt_in
		Initialization	mot_plant_id_62_62.m
		Scaling	mot_plant_pwr_scale.m
		Pre-Processing	mot_plant_preproc_init.m, mot_plant_preproc.m
		Post Processing	mot_postprocess, mot_state_scalar_postprocess, mot_state_signal_postprocess, mot_summary_postprocess
Torque Coupling	Plant	Model	tc_plant_map_trqloss_funTW
		Initialization	tc_plant_16.m
		Post Processing	tc_postprocess, tc_state_scalar_postprocess, tc_state_signal_postprocess, tc_summary_postprocess
Final Drive	Plant	Model	fd_plant_map_trqloss_funTW
		Initialization	fd_plant_444_accord.m
		Post Processing	fd_postprocess, fd_state_scalar_postprocess, fd_state_signal_postprocess, fd_summary_postprocess
Wheel	Controller	Model	whl_ctrl_regen
	Plant	Model	Wheel Plant
		Initialization	whl_plant_0317_P195_65_R15.m
		Pre-Processing	whl_plant_preproc.m
		Post Processing	whl_postprocess, whl_state_scalar_postprocess, whl_state_signal_postprocess, whl_summary_postprocess
Chassis	Plant	Model	chas_plant_veh_equation_losses
		Initialization	chas_plant_990_225_03_midsize.m
		Post Processing	chas_postprocess, chas_state_scalar_equation_losses_postprocess, chas_state_signal_postprocess, chas_summary_postprocess
Power Converter	Plant	Model	Power Converter with voltage input and voltage output and constant efficiency
		Initialization	pc_plant_095_12.m
		Post Processing	pc_post_process, pc_state_scalar_postprocess, pc_state_signal_postprocess, pc_summary_post_process
Elec. Accessory	Plant	Model	accelec_plant_const_pwrloss_volt_in
		Initialization	accelec_plant_200.m
		Post Processing	accelec_postprocess, accelec_state_scalar_postprocess, accelec_state_signal_postprocess, accelec_summary_postprocess

Appendix B – Thevenin Simulink Model

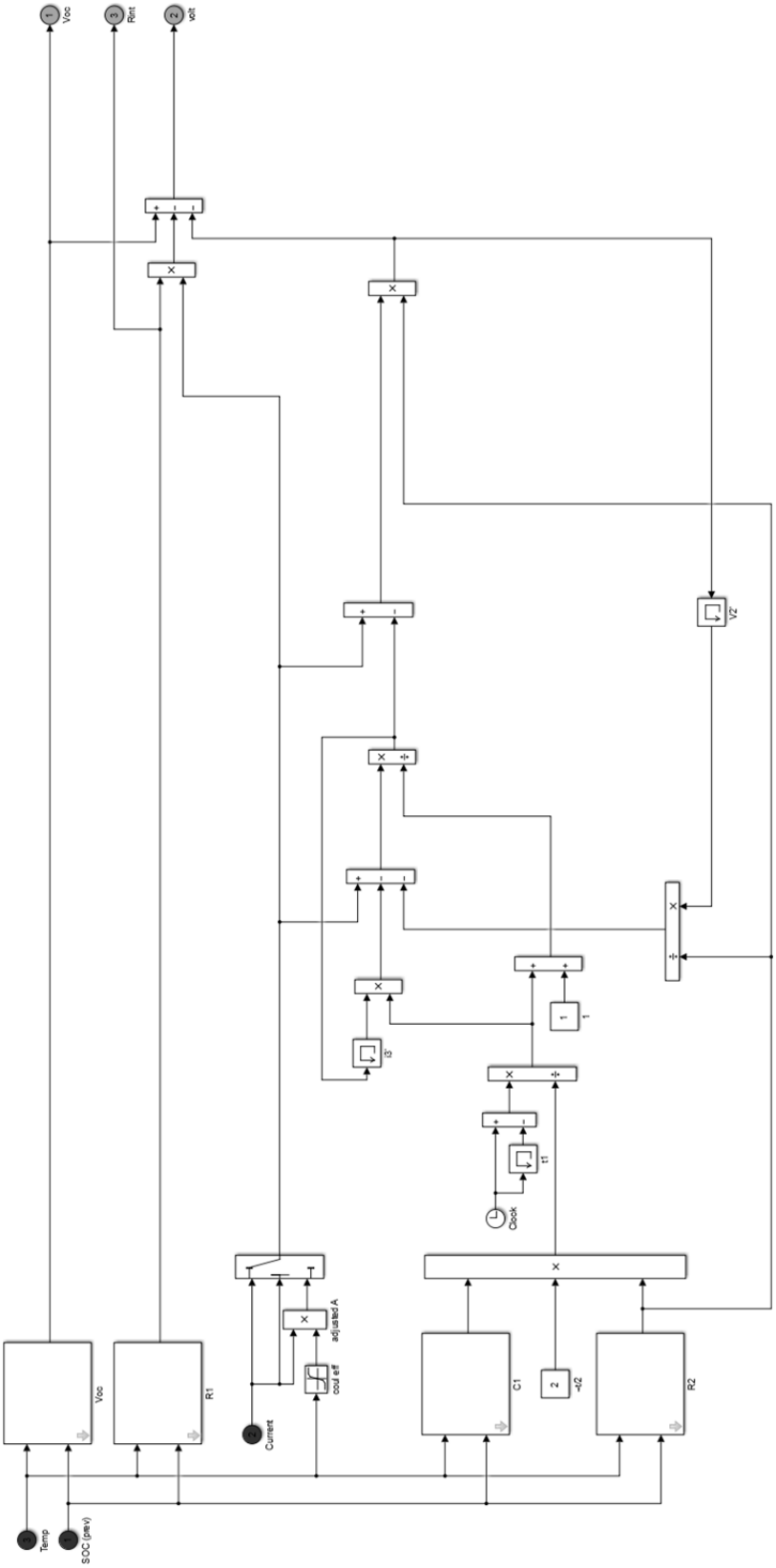

ess/plant/ess_plant_Thevenin_map.a_model

To be viewed with equation 13 s 2.2.1.2

Appendix C – Rint Autonomie Code

```
%% File description
% Name:        ess_plant_li_LFP_A123_UWAFT
% Author:      William Scott
% Model:       ess_plant_generic_map  (Rint)
% Technology:  Li-ion
% Vehicle Type:Light, Heavy

%%%%%%%%%%%%%%%%%%%%%%%%%%%%%%%%%%
%%%%%%%%%% Disclaimer %%%%%%%%%%%%
%%%%%%%%%%%%%%%%%%%%%%%%%%%%%%%%%%

%The following code is truncated to include the fitted parameters only.
%The truncated code is composed of initialization file defaults.
%Truncation was performed to protect the integrity of the source and to preserve space.

ess.plant.init.design_num_module_parallel    = 1;
ess.plant.init.soc_init                      = 0.7;
ess.plant.init.element_per_module            = 96;
ess.plant.init.num_module                    = 1;
ess.plant.init.design_num_cell_series        = ess.plant.init.num_module *
                                               ess.plant.init.element_per_module;
ess.plant.init.volt_nom                      = 3.20;
ess.plant.init.volt_min                      = 2.00;
ess.plant.init.volt_max                      = 3.65;
ess.plant.init.packaging_factor              = 1.25;
ess.plant.init.mass_module                   =
                                               198/ess.plant.init.packaging_factor/(ess.plant.init.
                                               num_module*ess.plant.init.design_num_module_parallel
                                               );
ess.plant.init.mass_cell                     =
                                               ess.plant.init.mass_module/ess.plant.init.element_pe
                                               r_module;
ess.plant.init.soc_min                       = 0.1;
ess.plant.init.soc_max                       = 0.9;

% LOSS AND EFFICIENCY parameters
ess.plant.init.soc_index                     = [0 : .1 : 1];
ess.plant.init.temp_index                    = [20 25 30];
ess.plant.init.cap_max.idx1_temp             = ess.plant.init.temp_index;
ess.plant.init.cap_max.map                   = [15 15 15];
ess.plant.init.eff_coulomb.idx1_temp         = ess.plant.init.temp_index;
ess.plant.init.eff_coulomb.map               = [1 1 1];

% cell's open-circuit (a.k.a. no-load) voltage, indexed by ess.plant.init.soc_index
ess.plant.init.voc.idx1_temp                 = ess.plant.init.temp_index;
ess.plant.init.voc.idx2_soc                  = ess.plant.init.soc_index;
ess.plant.init.voc.map                       =
[3.041 3.207   3.243   3.274   3.293   3.294   3.2965 3.314   3.336   3.338   3.347;
 3.041 3.207   3.243   3.274   3.293   3.294   3.2965  3.314   3.336   3.338   3.347;
 3.041 3.207   3.243   3.274   3.293   3.294   3.2965  3.314   3.336   3.338   3.347]; % V

% cell's resistance to being discharged, indexed by ess.plant.init.soc_index
ess.plant.init.rint_dis.idx1_temp            = ess.plant.init.temp_index;
ess.plant.init.rint_dis.idx2_soc             = ess.plant.init.soc_index;
ess.plant.init.rint_dis.map                  =
[0.00622 0.00411 0.00373 0.00358 0.00340 0.00335 0.00322 0.00312 0.00301 0.00291 0.00285;
 0.00622 0.00411 0.00373 0.00358 0.00340 0.00335 0.00322 0.00312 0.00301 0.00291 0.00285;
 0.00622 0.00411 0.00373 0.00358 0.00340 0.00335 0.00322 0.00312 0.00301 0.00291 0.00285]; % ohm

% cell's resistance to being charged, indexed by ess.plant.init.soc_index
ess.plant.init.rint_chg.idx1_temp            = ess.plant.init.temp_index;
ess.plant.init.rint_chg.idx2_soc             = ess.plant.init.soc_index;
ess.plant.init.rint_chg.map                  =
[0.00213 0.00123 0.00101 0.00090 0.00093 0.00097 0.00107 0.00106 0.00115 0.00128 0.00135;
 0.00213 0.00123 0.00101 0.00090 0.00093 0.00097 0.00107 0.00106 0.00115 0.00128 0.00135;
 0.00213 0.00123 0.00101 0.00090 0.00093 0.00097 0.00107 0.00106 0.00115 0.00128 0.00135]; % ohm
```

Appendix D – Thevenin Autonomie Code

```
%% File description
% Name:        ess_plant_li_LFP_A123_UWAFT
% Author:      William Scott
% Model:       Thevenin - WWS (Thevenin)
% Technology:  Li-ion
% Vehicle Type:Light, Heavy

%% File content
ess.plant.init.design_num_module_parallel    = 1;
ess.plant.init.soc_init                      = 0.7;
ess.plant.init.element_per_module            = 96;
ess.plant.init.num_module                    = 1;
ess.plant.init.design_num_cell_series        = ess.plant.init.num_module *
                                               ess.plant.init.element_per_module;
ess.plant.init.volt_nom                      = 3.20;
ess.plant.init.volt_min                      = 2.00;
ess.plant.init.volt_max                      = 3.65;
ess.plant.init.packaging_factor              = 1.25;
ess.plant.init.mass_module                   =
                                               198/ess.plant.init.packaging_factor/(ess.plant.init.
                                               num_module*ess.plant.init.design_num_module_parallel
                                               );
ess.plant.init.mass_cell                     =
                                               ess.plant.init.mass_module/ess.plant.init.element_pe
                                               r_module;
ess.plant.init.soc_min                       = 0.1;
ess.plant.init.soc_max                       = 0.9;

% LOSS AND EFFICIENCY parameters
ess.plant.init.soc_index                     = [0 : .1 : 1];
ess.plant.init.temp_index                    = [20 25 30];
ess.plant.init.cap_max.idx1_temp             = ess.plant.init.temp_index;
ess.plant.init.cap_max.map                   = [15 15 15];
ess.plant.init.eff_coulomb.idx1_temp         = ess.plant.init.temp_index;
ess.plant.init.eff_coulomb.map               = [1 1 1];

% cell's open-circuit (a.k.a. no-load) voltage, indexed by ess.plant.init.soc_index
ess.plant.init.voc.idx1_temp                 = ess.plant.init.temp_index;
ess.plant.init.voc.idx2_soc                  = ess.plant.init.soc_index;
ess.plant.init.voc.map                       =
[3.041  3.207   3.243   3.274   3.293   3.294   3.2965  3.314   3.336   3.338   3.347;
 3.041  3.207   3.243   3.274   3.293   3.294   3.2965  3.314   3.336   3.338   3.347;
 3.041  3.207   3.243   3.274   3.293   3.294   3.2965  3.314   3.336   3.338   3.347]; % V

% cell's R1, indexed by ess.plant.init.soc_index
ess.plant.init.r1.idx1_temp                  = ess.plant.init.temp_index;
ess.plant.init.r1.idx2_soc                   = ess.plant.init.soc_index;
ess.plant.init.r1.map                        =
[0.00321 0.00276 0.00271 0.00268 0.00272 0.00249 0.00249 0.00250 0.00249 0.00240 0.00241;
 0.00321 0.00276 0.00271 0.00268 0.00272 0.00249 0.00249 0.00250 0.00249 0.00240 0.00241;
 0.00321 0.00276 0.00271 0.00268 0.00272 0.00249 0.00249 0.00250 0.00249 0.00240 0.00241]; % ohm

% cell's R2, indexed by ess.plant.init.soc_index
ess.plant.init.r2.idx1_temp                  = ess.plant.init.temp_index;
ess.plant.init.r2.idx2_soc                   = ess.plant.init.soc_index;
ess.plant.init.r2.map                        =
[0.02176 0.00426 0.00517 0.00519 0.00541 0.00196 0.00197 0.00285 0.00289 0.00208 0.00232;
 0.02176 0.00426 0.00517 0.00519 0.00541 0.00196 0.00197 0.00285 0.00289 0.00208 0.00232;
 0.02176 0.00426 0.00517 0.00519 0.00541 0.00196 0.00197 0.00285 0.00289 0.00208 0.00232]; % ohm

% cell's C1, indexed by ess.plant.init.soc_index
ess.plant.init.c1.idx1_temp                  = ess.plant.init.temp_index;
ess.plant.init.c1.idx2_soc                   = ess.plant.init.soc_index;
ess.plant.init.c1.map                        =
[4680.02 9620.50 13733.3 15899.6 17166.3 18002.1 18223.4 18580.8 18469.8 18218.1 17997.0;
 4680.02 9620.50 13733.3 15899.6 17166.3 18002.1 18223.4 18580.8 18469.8 18218.1 17997.0;
 4680.02 9620.50 13733.3 15899.6 17166.3 18002.1 18223.4 18580.8 18469.8 18218.1 17997.0987]; % F
```

```
% Max current and power when charging/discharging
ess.plant.init.curr_chg_max                 = -max((ess.plant.init.volt_max-
                                            ess.plant.init.voc.map)./ess.plant.init.r1.map);
ess.plant.init.curr_dis_max                 = max((ess.plant.init.voc.map-
                                            ess.plant.init.volt_min)./ess.plant.init.r1.map);

%check the ess.plant.init.pwr_chg & ess.plant.init.pwr_dis because they're a vector
ess.plant.init.pwr_chg.idx1_soc             = ess.plant.init.soc_index;
ess.plant.init.pwr_dis.idx1_soc             = ess.plant.init.soc_index;
ess.plant.init.pwr_chg.map                  = -max((ess.plant.init.volt_max-
                                            ess.plant.init.voc.map).*ess.plant.init.volt_max./es
                                            s.plant.init.r1.map);%per cell
ess.plant.init.pwr_dis.map                  = max((ess.plant.init.voc.map-
                                            ess.plant.init.volt_min).*ess.plant.init.volt_min./e
                                            ss.plant.init.r1.map);%per cell
ess.plant.init.pwr_chg.map                  =
                                            ess.plant.init.pwr_chg.map.*double(ess.plant.init.so
                                            c_index <= ess.plant.init.soc_max);
ess.plant.init.pwr_dis.map                  = ess.plant.init.pwr_dis.map.*
                                            double(ess.plant.init.soc_index >=
                                            ess.plant.init.soc_min);
ess.plant.init.pwr_chg_at_min_soc           =
                                            interp1(ess.plant.init.soc_index,ess.plant.init.pwr_
                                            chg.map,ess.plant.init.soc_min); % (0->1) Power at
                                            which battery is charged when SOC is at its minimum
ess.plant.init.pwr_dis_at_max_soc           =
                                            interp1(ess.plant.init.soc_index,ess.plant.init.pwr_
                                            dis.map,ess.plant.init.soc_max); % (0->1) Power at
                                            which battery is discharged when SOC is at its
                                            maximum
ess.plant.init.pwr_chg_max                  = -max(max((ess.plant.init.volt_max-
                                            ess.plant.init.voc.map).*ess.plant.init.volt_max./es
                                            s.plant.init.r1.map));%per cell
ess.plant.init.pwr_dis_max                  = max(max((ess.plant.init.voc.map-
                                            ess.plant.init.volt_min).*ess.plant.init.volt_min./e
                                            ss.plant.init.r1.map));%per cell

% battery thermal model
ess.plant.init.therm_on                     = 0; % 0=no ess thermal calculations, 1=do calc's
ess.plant.init.therm_cp_module              = 521;
ess.plant.init.temp_reg                     = 35;
ess.plant.init.dia                          = 0.0322;
ess.plant.init.length                       = 0.374;
ess.plant.init.area_module                  = pi*ess.plant.init.dia*ess.plant.init.length;
ess.plant.init.flow_air_mod                 = 0.01;
ess.plant.init.therm_flow_area_module       = 2*0.00317*ess.plant.init.length;
ess.plant.init.case_thk                     = .1/1000;
ess.plant.init.mod_case_th_cond             = 0.20;
ess.plant.init.speed_air                    =
                                            ess.plant.init.flow_air_mod/(1.16*ess.plant.init.the
                                            rm_flow_area_module);  % m/s  ave velocity of
                                            cooling air
ess.plant.init.therm_air_htcoef             = 30*(ess.plant.init.speed_air/5)^0.8;
ess.plant.init.therm_res_on                 =
                                            ((1/ess.plant.init.therm_air_htcoef)+(ess.plant.init
                                            .case_thk/ess.plant.init.mod_case_th_cond))/ess.plan
                                            t.init.area_module;
ess.plant.init.therm_res_off                =
                                            ((1/4)+(ess.plant.init.case_thk/ess.plant.init.mod_c
                                            ase_th_cond))/ess.plant.init.area_module;% K/W  tot
                                            thermal res key off (cold soak)
ess.plant.init.flow_air_mod                 = max(ess.plant.init.flow_air_mod,0.001);
ess.plant.init.therm_res_on                 =
                                            min(ess.plant.init.therm_res_on,ess.plant.init.therm
                                            _res_off);

% Battery density
ess.plant.init.pwr_dis_nom                  = max((ess.plant.init.volt_nom-
                                            ess.plant.init.volt_min).*ess.plant.init.volt_min./e
                                            ss.plant.init.r1.map);%per cell
```

```
ess.plant.init.pwr_density                  =
                                            ess.plant.init.pwr_dis_nom/ess.plant.init.mass_cell;
ess.plant.init.energy_density               =
                                            (ess.plant.init.volt_nom*ess.plant.init.cap_max.map)
                                            /ess.plant.init.mass_cell;

%Values should only be used to calculate the number of cells
ess.plant.init.num_cell_series              = ess.plant.init.design_num_cell_series;
ess.plant.init.num_module_parallel          = ess.plant.init.design_num_module_parallel;
ess.plant.init.num_cell                     =
                                            ess.plant.init.num_module_parallel.*ess.plant.init.n
                                            um_cell_series;
ess.plant.init.energy                       =
                                            max(ess.plant.init.cap_max.map).*ess.plant.init.volt
                                            _nom;
```

Appendix E – AER for 2014 Vehicles

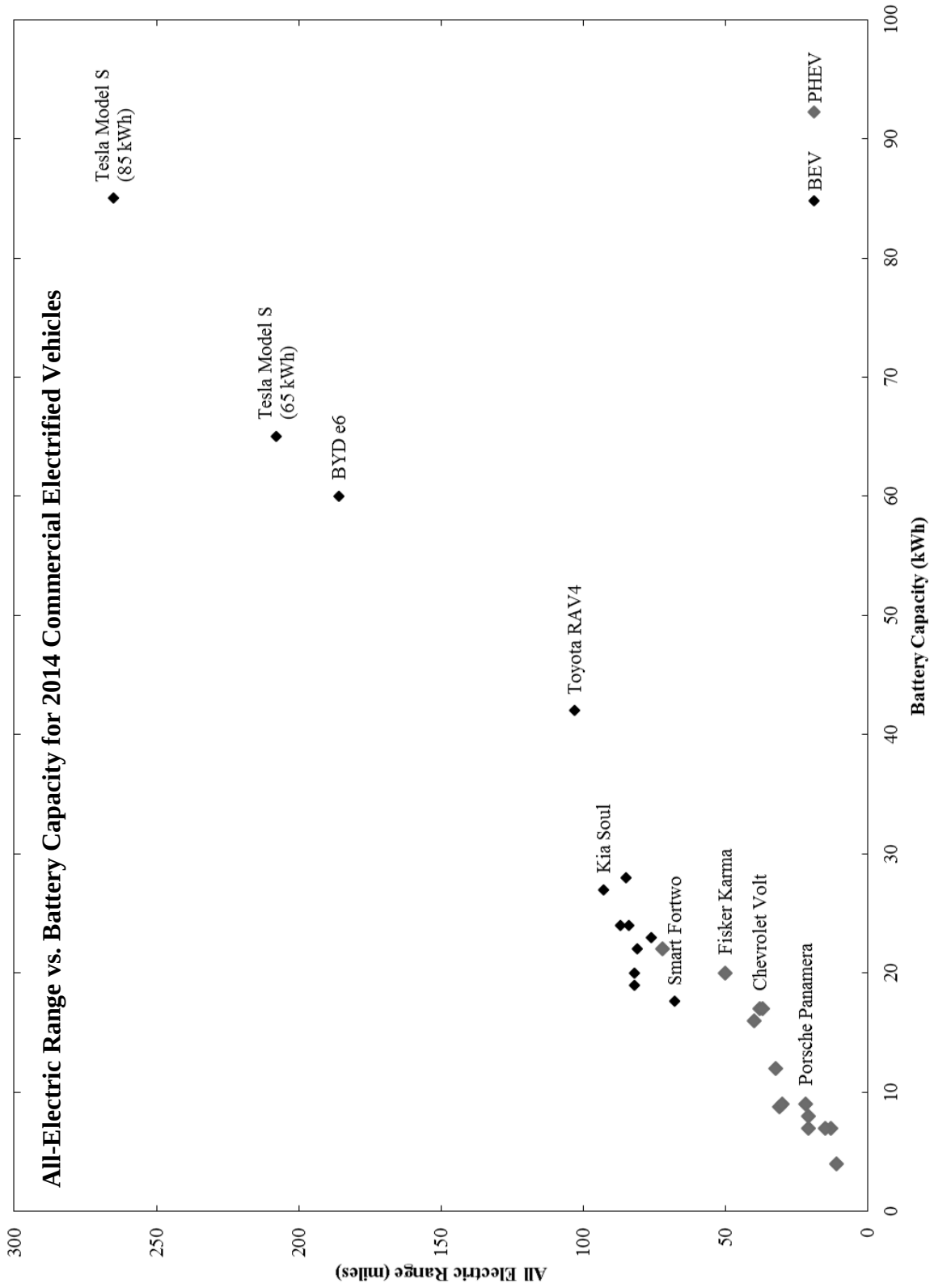

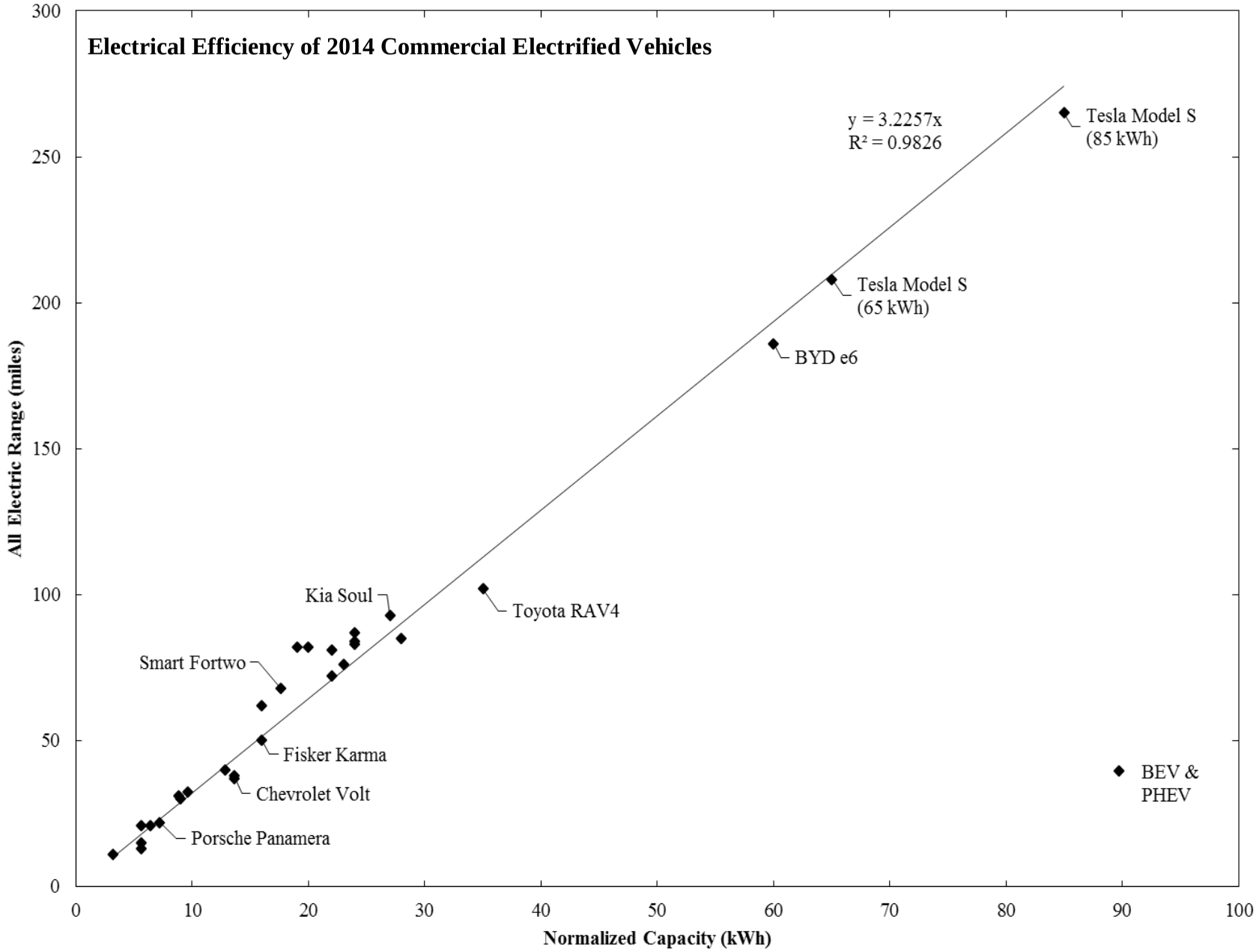
Electrical Efficiency of 2014 Commercial Electrified Vehicles
y = 3.2257x
R² = 0.9826
Tesla Model S (85 kWh)
Tesla Model S (65 kWh)
BYD e6
Toyota RAV4
Kia Soul
Smart Fortwo
Fisker Karma
Chevrolet Volt
Porsche Panamera
BEV & PHEV
All Electric Range (miles)
Normalized Capacity (kWh)
0
50
100
150
200
250
300
0
10
20
30
40
50
60
70
80
90
100

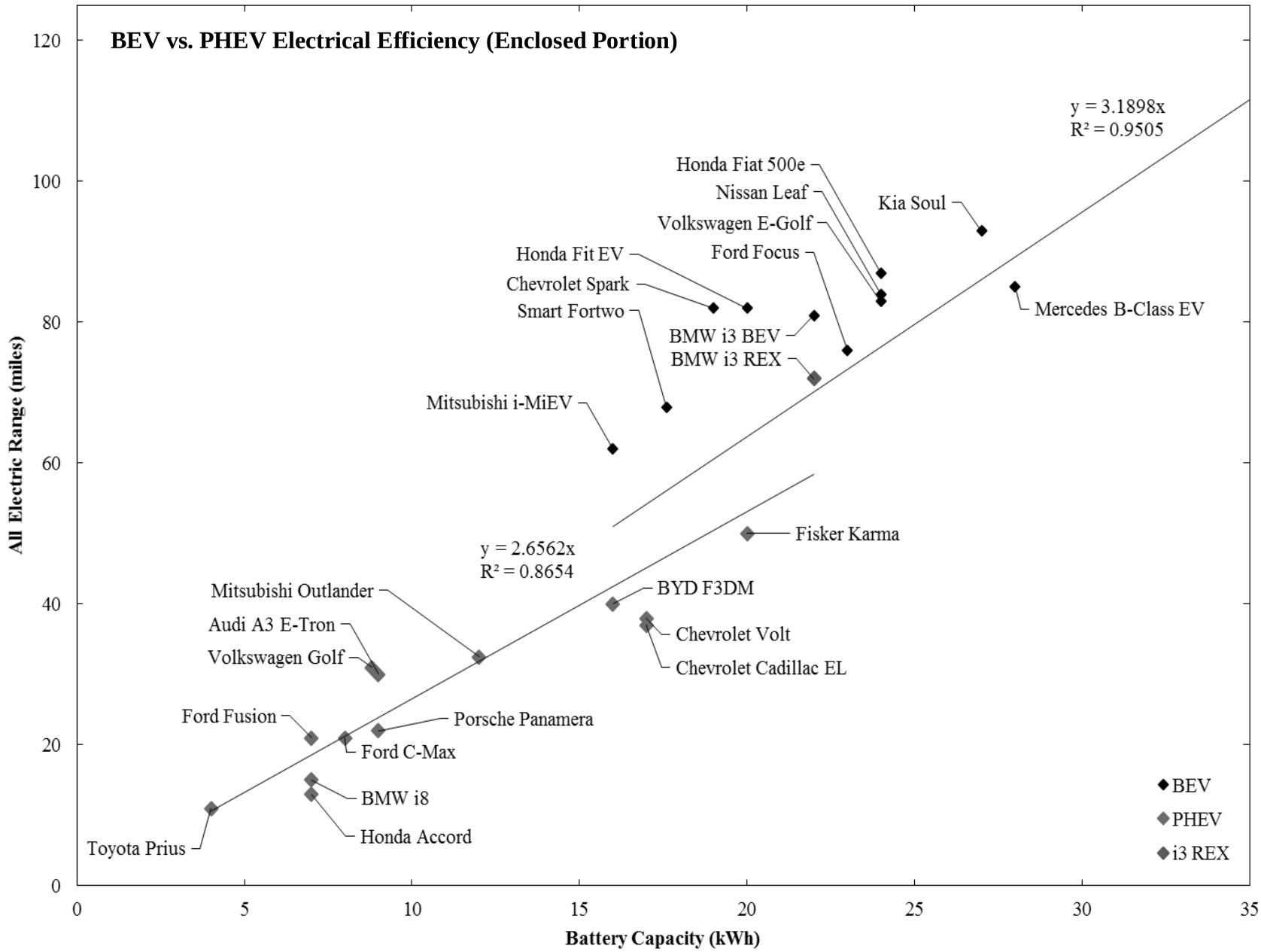
BEV vs. PHEV Electrical Efficiency (Enclosed Portion)
All Electric Range (miles)
Battery Capacity (kWh)
y = 3.1898x
R² = 0.9505
y = 2.6562x
R² = 0.8654
Honda Fiat 500e
Nissan Leaf
Volkswagen E-Golf
Kia Soul
Honda Fit EV
Ford Focus
Chevrolet Spark
Smart Fortwo
Mercedes B-Class EV
BMW i3 BEV
BMW i3 REX
Mitsubishi i-MiEV
Fisker Karma
Mitsubishi Outlander
BYD F3DM
Audi A3 E-Tron
Chevrolet Volt
Volkswagen Golf
Chevrolet Cadillac EL
Ford Fusion
Porsche Panamera
Ford C-Max
BMW i8
Honda Accord
Toyota Prius
BEV
PHEV
i3 REX

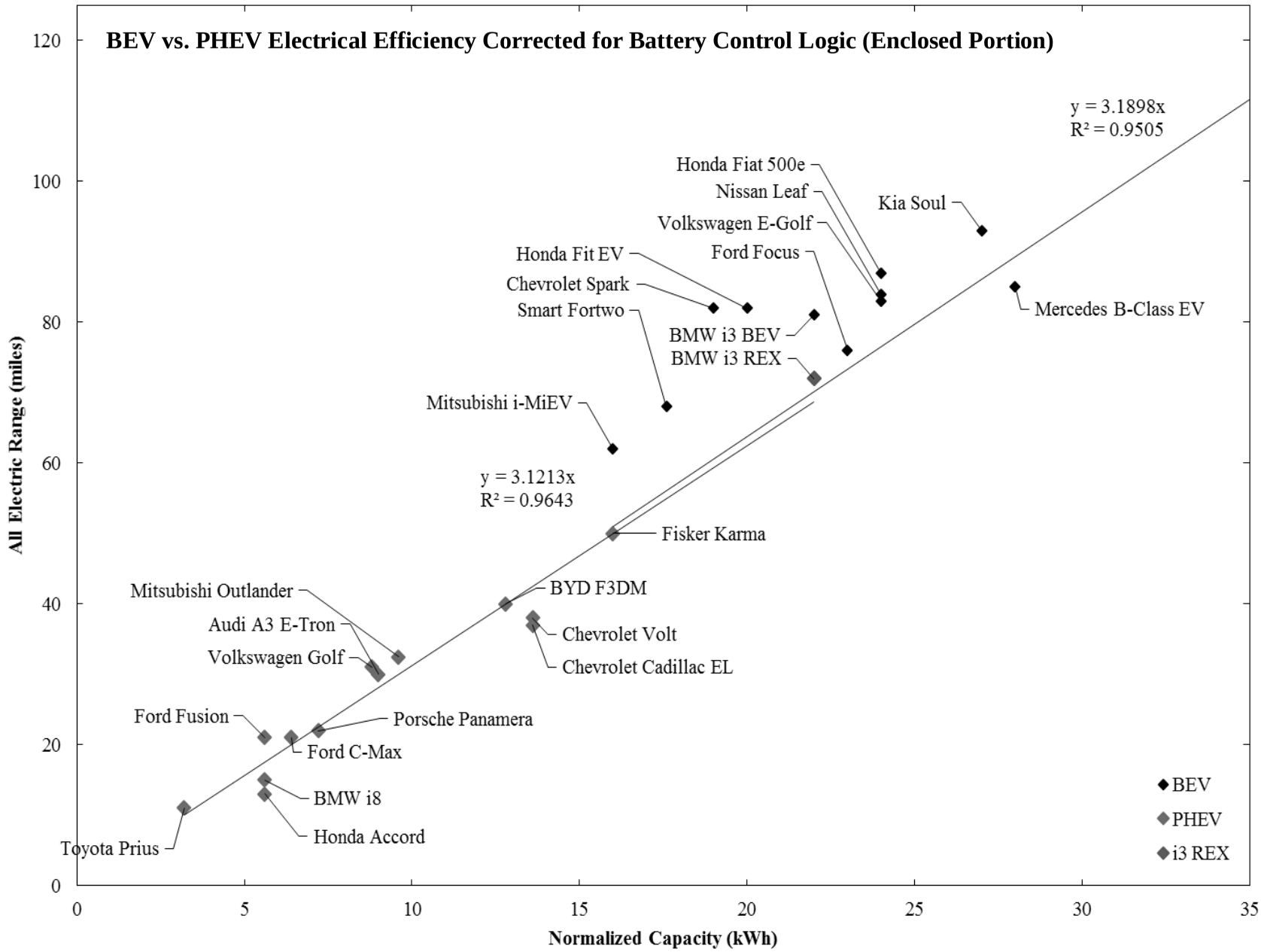
BEV vs. PHEV Electrical Efficiency Corrected for Battery Control Logic (Enclosed Portion)
All Electric Range (miles)
Normalized Capacity (kWh)
y = 3.1898x
R² = 0.9505
y = 3.1213x
R² = 0.9643
Honda Fiat 500e
Nissan Leaf
Volkswagen E-Golf
Kia Soul
Honda Fit EV
Ford Focus
Chevrolet Spark
Smart Fortwo
Mercedes B-Class EV
BMW i3 BEV
BMW i3 REX
Mitsubishi i-MiEV
Fisker Karma
Mitsubishi Outlander
BYD F3DM
Audi A3 E-Tron
Chevrolet Volt
Volkswagen Golf
Chevrolet Cadillac EL
Ford Fusion
Porsche Panamera
Ford C-Max
BMW i8
Honda Accord
Toyota Prius
BEV
PHEV
i3 REX

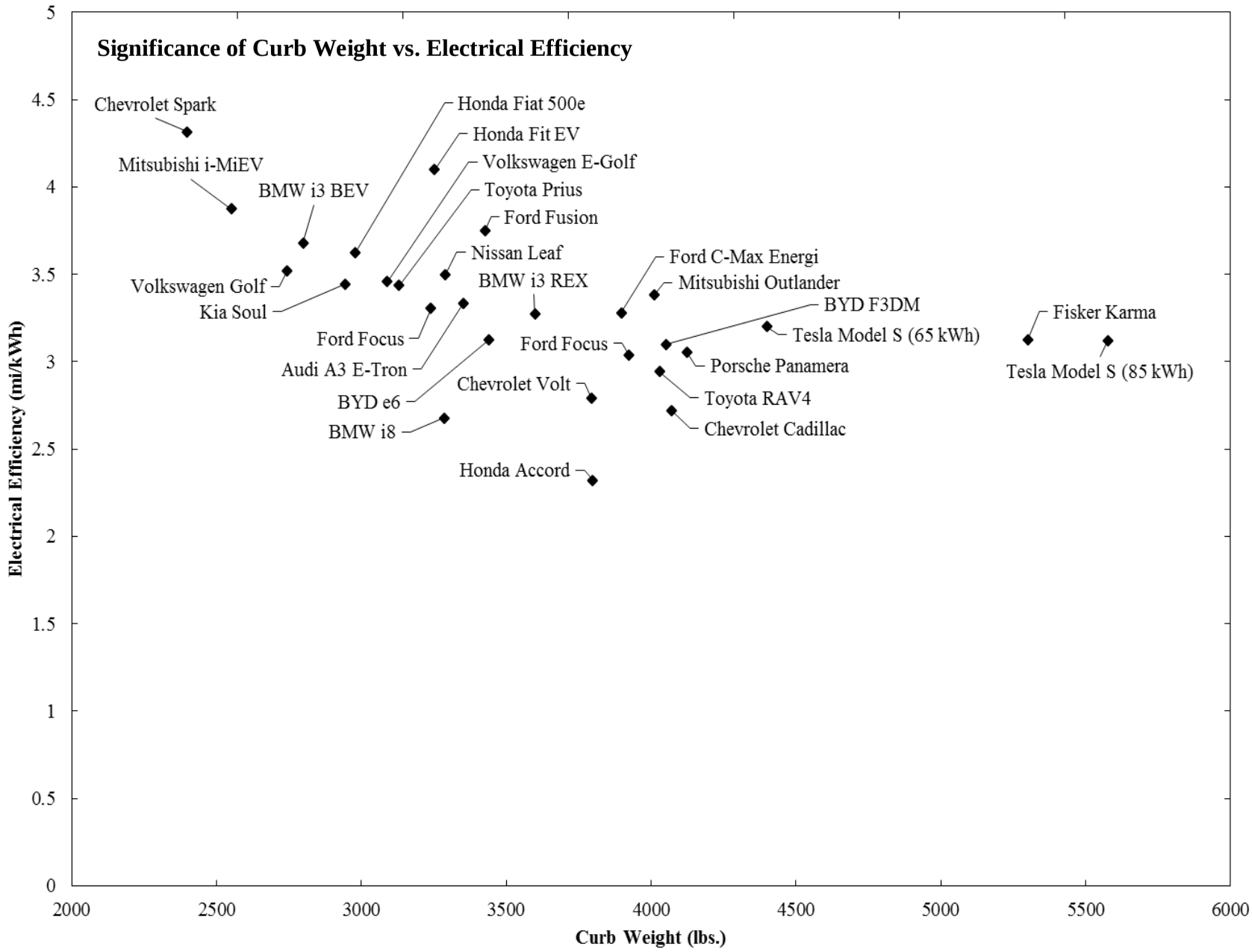
Significance of Curb Weight vs. Electrical Efficiency
Electrical Efficiency (mi/kWh)
Curb Weight (lbs.)
0
0.5
1
1.5
2
2.5
3
3.5
4
4.5
5
2000
2500
3000
3500
4000
4500
5000
5500
6000
Chevrolet Spark
Mitsubishi i-MiEV
BMW i3 BEV
Volkswagen Golf
Kia Soul
Honda Fiat 500e
Honda Fit EV
Volkswagen E-Golf
Toyota Prius
Ford Fusion
Nissan Leaf
BMW i3 REX
Ford Focus
Audi A3 E-Tron
BYD e6
BMW i8
Honda Accord
Chevrolet Volt
Ford Focus
Ford C-Max Energi
Mitsubishi Outlander
BYD F3DM
Tesla Model S (65 kWh)
Porsche Panamera
Toyota RAV4
Chevrolet Cadillac
Fisker Karma
Tesla Model S (85 kWh)

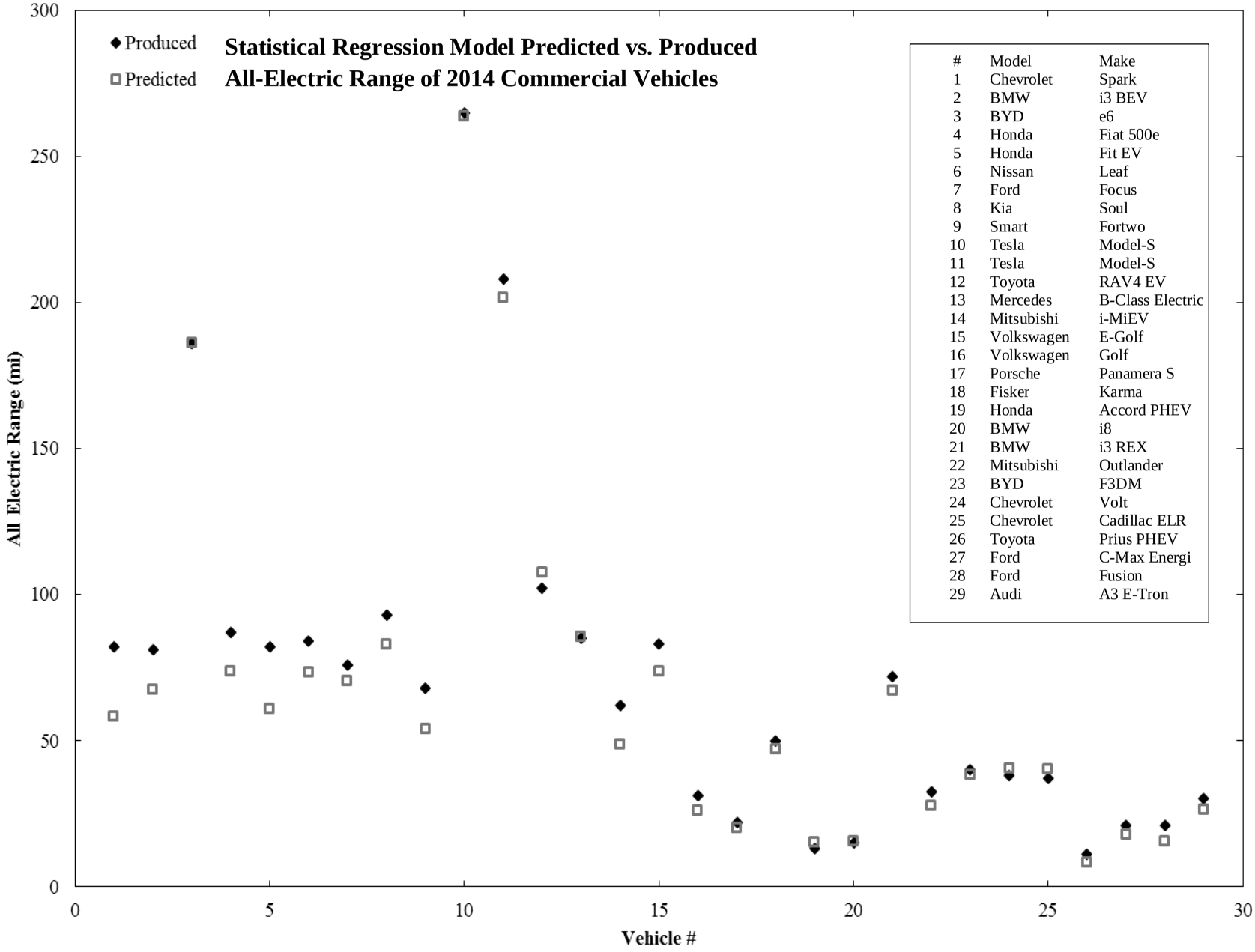
Produced
Predicted
Statistical Regression Model Predicted vs. Produced
All-Electric Range of 2014 Commercial Vehicles
All Electric Range (mi)
Vehicle #
0
50
100
150
200
250
300
0
5
10
15
20
25
30
Model Make
1 Chevrolet Spark
2 BMW i3 BEV
3 BYD e6
4 Honda Fiat 500e
5 Honda Fit EV
6 Nissan Leaf
7 Ford Focus
8 Kia Soul
9 Smart Fortwo
10 Tesla Model-S
11 Tesla Model-S
12 Toyota RAV4 EV
13 Mercedes B-Class Electric
14 Mitsubishi i-MiEV
15 Volkswagen E-Golf
16 Volkswagen Golf
17 Porsche Panamera S
18 Fisker Karma
19 Honda Accord PHEV
20 BMW i8
21 BMW i3 REX
22 Mitsubishi Outlander
23 BYD F3DM
24 Chevrolet Volt
25 Chevrolet Cadillac ELR
26 Toyota Prius PHEV
27 Ford C-Max Energi
28 Ford Fusion
29 Audi A3 E-Tron

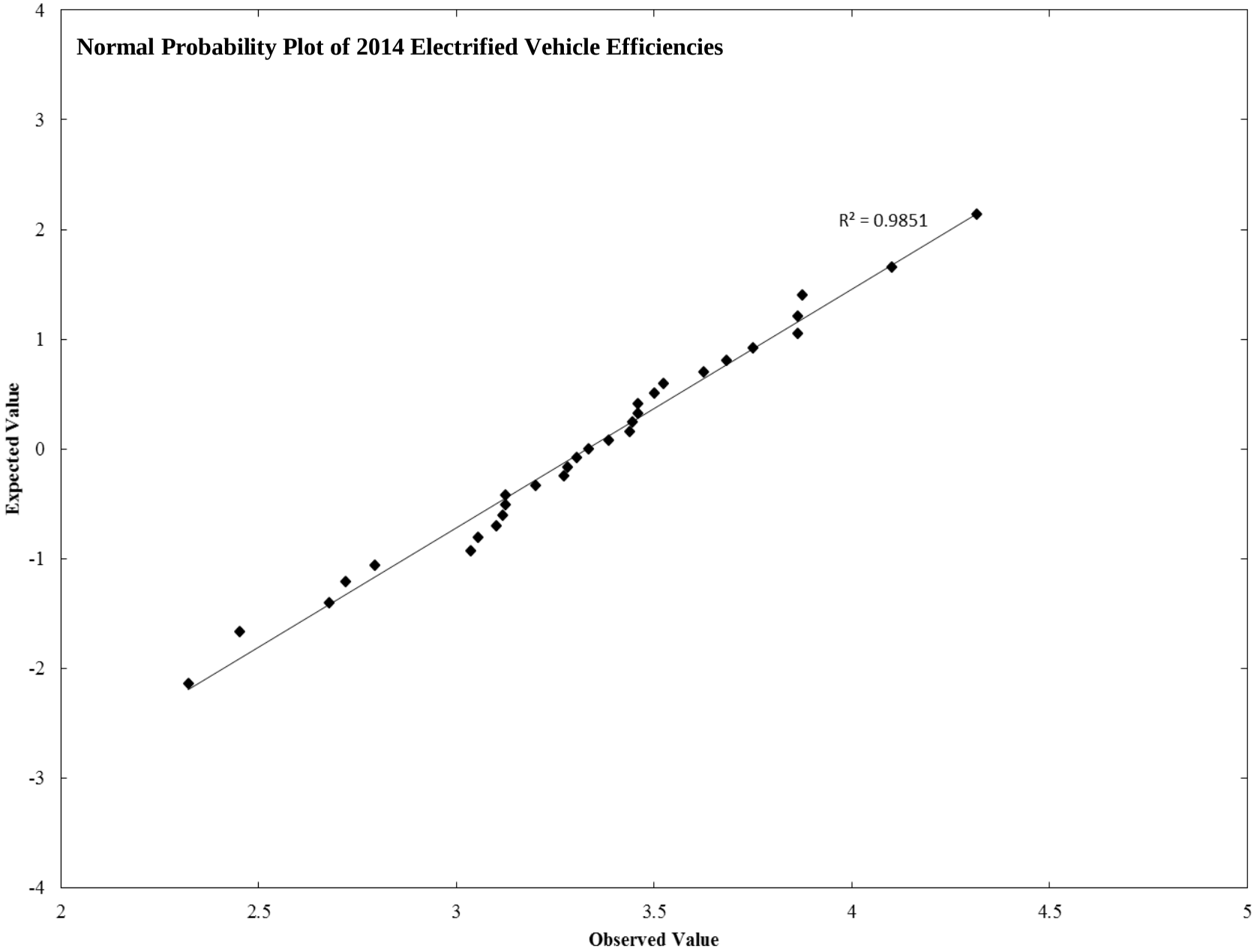
Normal Probability Plot of 2014 Electrified Vehicle Efficiencies
R² = 0.9851
Expected Value
Observed Value
4
3
2
1
0
-1
-2
-3
-4
2
2.5
3
3.5
4
4.5
5

Appendix F – HPPC Sample Data & Fit

HPPC @ 95% SOC & 23 ℃

Data Entry						Model							Solver			Circuit Elements	
Test Time,s	Step Time, s	Capacity, %	Current, A	Voltage, V	MD	V_{model}	V_{OC}	V_1	V_2	i_1*	i_2	i_3	Dif.	Weight	Objective	R_1	0.002378
18820.63	0.05	0.971	117.587	3.099	D	3.061	3.341	0.280	0.000	117.587	0.000	117.587	0.038	0.000	**0.187**	R_2	0.001904
18820.64	0.06	0.971	116.415	3.094	D	3.064	3.341	0.277	0.000	116.415	0.034	116.381	0.030	0.000		C_1	18174.18
18820.65	0.07	0.972	116.437	3.092	D	3.064	3.341	0.277	0.000	116.437	0.067	116.370	0.028	0.000			
18820.66	0.08	0.972	116.464	3.090	D	3.064	3.341	0.277	0.000	116.464	0.101	116.363	0.026	0.000			
18820.67	0.09	0.972	116.440	3.088	D	3.064	3.341	0.277	0.000	116.440	0.135	116.305	0.024	0.000			
18820.68	0.10	0.973	116.448	3.087	D	3.064	3.341	0.277	0.000	116.448	0.168	116.280	0.023	0.000			
18820.69	0.11	0.973	116.453	3.085	D	3.064	3.341	0.277	0.000	116.453	0.202	116.251	0.021	0.000			
18820.70	0.12	0.973	116.461	3.084	D	3.064	3.341	0.277	0.000	116.461	0.236	116.225	0.020	0.000			
18820.71	0.13	0.974	116.448	3.085	D	3.064	3.341	0.277	0.001	116.448	0.269	116.179	0.021	0.000			
18820.72	0.14	0.974	116.453	3.084	D	3.064	3.341	0.277	0.001	116.453	0.303	116.150	0.020	0.000			
18820.73	0.15	0.974	116.446	3.083	D	3.063	3.341	0.277	0.001	116.446	0.336	116.110	0.020	0.000			
18820.74	0.16	0.975	116.446	3.082	D	3.063	3.341	0.277	0.001	116.446	0.370	116.076	0.019	0.000			
18820.75	0.17	0.975	116.455	3.081	D	3.063	3.341	0.277	0.001	116.455	0.403	116.052	0.018	0.000			
18820.76	0.18	0.975	116.446	3.081	D	3.063	3.341	0.277	0.001	116.446	0.437	116.009	0.018	0.000			
18820.77	0.19	0.976	116.457	3.080	D	3.063	3.341	0.277	0.001	116.457	0.470	115.987	0.017	0.000			
18820.78	0.20	0.976	116.450	3.079	D	3.063	3.341	0.277	0.001	116.450	0.504	115.946	0.016	0.000			
18820.79	0.21	0.976	116.448	3.079	D	3.063	3.341	0.277	0.001	116.448	0.537	115.911	0.016	0.000			
18820.80	0.22	0.977	116.444	3.078	D	3.063	3.341	0.277	0.001	116.444	0.571	115.873	0.015	0.000			
18820.81	0.23	0.977	116.446	3.078	D	3.063	3.341	0.277	0.001	116.446	0.604	115.842	0.015	0.000			
18820.82	0.24	0.977	116.450	3.077	D	3.063	3.341	0.277	0.001	116.450	0.638	115.812	0.014	0.000			
18820.83	0.25	0.978	116.451	3.077	D	3.063	3.341	0.277	0.001	116.451	0.671	115.780	0.014	0.000			
18820.84	0.26	0.978	116.450	3.076	D	3.063	3.341	0.277	0.001	116.450	0.705	115.745	0.013	0.000			
18820.85	0.27	0.978	116.446	3.076	D	3.063	3.341	0.277	0.001	116.446	0.738	115.708	0.013	0.000			
18820.86	0.28	0.978	116.444	3.075	D	3.063	3.341	0.277	0.001	116.444	0.772	115.672	0.012	0.000			
18820.87	0.29	0.979	116.455	3.075	D	3.063	3.341	0.277	0.002	116.455	0.805	115.650	0.012	0.000			
18820.88	0.30	0.979	116.444	3.074	D	3.063	3.341	0.277	0.002	116.444	0.839	115.605	0.011	0.000			
18820.89	0.31	0.979	116.450	3.074	D	3.062	3.341	0.277	0.002	116.450	0.872	115.578	0.012	0.000			
18820.90	0.32	0.980	116.442	3.074	D	3.062	3.341	0.277	0.002	116.442	0.905	115.537	0.012	0.000			
18820.91	0.33	0.980	116.444	3.073	D	3.062	3.341	0.277	0.002	116.444	0.939	115.505	0.011	0.000			
18820.92	0.34	0.980	116.450	3.073	D	3.062	3.341	0.277	0.002	116.450	0.972	115.478	0.011	0.000			
18820.93	0.35	0.981	116.444	3.073	D	3.062	3.341	0.277	0.002	116.444	1.006	115.438	0.011	0.000			
18820.94	0.36	0.981	116.455	3.072	D	3.062	3.341	0.277	0.002	116.455	1.039	115.416	0.010	0.000			
18820.95	0.37	0.981	116.446	3.072	D	3.062	3.341	0.277	0.002	116.446	1.072	115.374	0.010	0.000			
18820.96	0.38	0.982	116.451	3.072	D	3.062	3.341	0.277	0.002	116.451	1.106	115.345	0.010	0.000			
18820.97	0.39	0.982	116.444	3.071	D	3.062	3.341	0.277	0.002	116.444	1.139	115.305	0.009	0.000			
18820.98	0.40	0.982	116.444	3.071	D	3.062	3.341	0.277	0.002	116.444	1.172	115.272	0.009	0.000			
18820.99	0.41	0.983	116.457	3.071	D	3.062	3.341	0.277	0.002	116.457	1.206	115.251	0.009	0.000			
18821.00	0.42	0.983	116.444	3.071	D	3.062	3.341	0.277	0.002	116.444	1.239	115.205	0.009	0.000			
18821.01	0.43	0.983	116.450	3.070	D	3.062	3.341	0.277	0.002	116.450	1.272	115.178	0.008	0.000			
18821.02	0.44	0.984	116.448	3.070	D	3.062	3.341	0.277	0.002	116.448	1.305	115.143	0.008	0.000			
18821.03	0.45	0.984	116.451	3.070	D	3.062	3.341	0.277	0.003	116.451	1.339	115.112	0.008	0.000			
18821.04	0.46	0.984	116.448	3.070	D	3.061	3.341	0.277	0.003	116.448	1.372	115.076	0.009	0.000			
18821.05	0.47	0.985	116.453	3.069	D	3.061	3.341	0.277	0.003	116.453	1.405	115.048	0.008	0.000			
18821.06	0.48	0.985	116.448	3.069	D	3.061	3.341	0.277	0.003	116.448	1.439	115.009	0.008	0.000			
18821.07	0.49	0.985	116.455	3.069	D	3.061	3.341	0.277	0.003	116.455	1.472	114.983	0.008	0.000			
18821.08	0.50	0.986	116.451	3.069	D	3.061	3.341	0.277	0.003	116.451	1.505	114.946	0.008	0.000			
18821.09	0.51	0.986	116.446	3.068	D	3.061	3.341	0.277	0.003	116.446	1.538	114.908	0.007	0.000			
18821.10	0.52	0.986	116.450	3.068	D	3.061	3.341	0.277	0.003	116.450	1.571	114.879	0.007	0.000			
18821.11	0.53	0.987	116.451	3.068	D	3.061	3.341	0.277	0.003	116.451	1.605	114.846	0.007	0.000			
18821.12	0.54	0.987	116.450	3.068	D	3.061	3.341	0.277	0.003	116.450	1.638	114.812	0.007	0.000			
18821.13	0.55	0.987	116.448	3.068	D	3.061	3.341	0.277	0.003	116.448	1.671	114.777	0.007	0.000			
18821.14	0.56	0.988	116.450	3.067	D	3.061	3.341	0.277	0.003	116.450	1.704	114.746	0.006	0.000			
18821.15	0.57	0.988	116.457	3.067	D	3.061	3.341	0.277	0.003	116.457	1.737	114.720	0.006	0.000			
18821.16	0.58	0.988	116.444	3.067	D	3.061	3.341	0.277	0.003	116.444	1.771	114.673	0.006	0.000			
18821.17	0.59	0.989	116.453	3.067	D	3.061	3.341	0.277	0.003	116.453	1.804	114.649	0.006	0.000			
18821.18	0.60	0.989	116.448	3.066	D	3.061	3.341	0.277	0.003	116.448	1.837	114.611	0.005	0.000			
18821.19	0.61	0.989	116.446	3.066	D	3.061	3.341	0.277	0.004	116.446	1.870	114.576	0.005	0.000			
18821.20	0.62	0.989	116.446	3.066	D	3.060	3.341	0.277	0.004	116.446	1.903	114.543	0.006	0.000			
18821.21	0.63	0.990	116.451	3.066	D	3.060	3.341	0.277	0.004	116.451	1.936	114.515	0.006	0.000			
18821.22	0.64	0.990	116.451	3.065	D	3.060	3.341	0.277	0.004	116.451	1.969	114.482	0.005	0.000			
18821.23	0.65	0.990	116.448	3.065	D	3.060	3.341	0.277	0.004	116.448	2.002	114.446	0.005	0.000			
18821.24	0.66	0.991	116.446	3.065	D	3.060	3.341	0.277	0.004	116.446	2.035	114.411	0.005	0.000			
18821.25	0.67	0.991	116.457	3.065	D	3.060	3.341	0.277	0.004	116.457	2.068	114.389	0.005	0.000			
18821.26	0.68	0.991	116.450	3.065	D	3.060	3.341	0.277	0.004	116.450	2.102	114.348	0.005	0.000			
18821.27	0.69	0.992	116.450	3.065	D	3.060	3.341	0.277	0.004	116.450	2.135	114.315	0.005	0.000			
18821.28	0.70	0.992	116.451	3.064	D	3.060	3.341	0.277	0.004	116.451	2.168	114.283	0.004	0.000			
18821.29	0.71	0.992	116.451	3.064	D	3.060	3.341	0.277	0.004	116.451	2.201	114.250	0.004	0.000			
18821.30	0.72	0.993	116.455	3.064	D	3.060	3.341	0.277	0.004	116.455	2.234	114.221	0.004	0.000			
18821.31	0.73	0.993	116.448	3.064	D	3.060	3.341	0.277	0.004	116.448	2.267	114.181	0.004	0.000			
18821.32	0.74	0.993	116.448	3.064	D	3.060	3.341	0.277	0.004	116.448	2.300	114.148	0.004	0.000			
18821.33	0.75	0.994	116.455	3.063	D	3.060	3.341	0.277	0.004	116.455	2.333	114.122	0.003	0.000			
18821.34	0.76	0.994	116.440	3.063	D	3.060	3.341	0.277	0.005	116.440	2.366	114.074	0.003	0.000			

Model						
V_{model}	V_{OC}	V_1	V_2	i_1*	i_2	i_3
=H4-I4-J4	3.341	=K4*$S$3	=L4*$S$4	=IF(F4="D",D4,-D4)	=K4-M4	=K4
=H5-I5-J5	=H4	=K5*$S$3	=L5*$S$4	=IF(F5="D",D5,-D5)	=K5-M5	=(K5*$S$4-(A5-A4)/(2*$S$5)*M4-J4)/((A5-A4)/(2*$S$5)+$S$4)
=H6-I6-J6	=H5	=K6*$S$3	=L6*$S$4	=IF(F6="D",D6,-D6)	=K6-M6	=(K6*$S$4-(A6-A5)/(2*$S$5)*M5-J5)/((A6-A5)/(2*$S$5)+$S$4)
=H7-I7-J7	=H6	=K7*$S$3	=L7*$S$4	=IF(F7="D",D7,-D7)	=K7-M7	=(K7*$S$4-(A7-A6)/(2*$S$5)*M6-J6)/((A7-A6)/(2*$S$5)+$S$4)
=H8-I8-J8	=H7	=K8*$S$3	=L8*$S$4	=IF(F8="D",D8,-D8)	=K8-M8	=(K8*$S$4-(A8-A7)/(2*$S$5)*M7-J7)/((A8-A7)/(2*$S$5)+$S$4)
=H9-I9-J9	=H8	=K9*$S$3	=L9*$S$4	=IF(F9="D",D9,-D9)	=K9-M9	=(K9*$S$4-(A9-A8)/(2*$S$5)*M8-J8)/((A9-A8)/(2*$S$5)+$S$4)
=H10-I10-J10	=H9	=K10*$S$3	=L10*$S$4	=IF(F10="D",D10,-D10)	=K10-M10	=(K10*$S$4-(A10-A9)/(2*$S$5)*M9-J9)/((A10-A9)/(2*$S$5)+$S$4)
=H11-I11-J11	=H10	=K11*$S$3	=L11*$S$4	=IF(F11="D",D11,-D11)	=K11-M11	=(K11*$S$4-(A11-A10)/(2*$S$5)*M10-J10)/((A11-A10)/(2*$S$5)+$S$4)
=H12-I12-J12	=H11	=K12*$S$3	=L12*$S$4	=IF(F12="D",D12,-D12)	=K12-M12	=(K12*$S$4-(A12-A11)/(2*$S$5)*M11-J11)/((A12-A11)/(2*$S$5)+$S$4)
=H13-I13-J13	=H12	=K13*$S$3	=L13*$S$4	=IF(F13="D",D13,-D13)	=K13-M13	=(K13*$S$4-(A13-A12)/(2*$S$5)*M12-J12)/((A13-A12)/(2*$S$5)+$S$4)
=H14-I14-J14	=H13	=K14*$S$3	=L14*$S$4	=IF(F14="D",D14,-D14)	=K14-M14	=(K14*$S$4-(A14-A13)/(2*$S$5)*M13-J13)/((A14-A13)/(2*$S$5)+$S$4)
=H15-I15-J15	=H14	=K15*$S$3	=L15*$S$4	=IF(F15="D",D15,-D15)	=K15-M15	=(K15*$S$4-(A15-A14)/(2*$S$5)*M14-J14)/((A15-A14)/(2*$S$5)+$S$4)
=H16-I16-J16	=H15	=K16*$S$3	=L16*$S$4	=IF(F16="D",D16,-D16)	=K16-M16	=(K16*$S$4-(A16-A15)/(2*$S$5)*M15-J15)/((A16-A15)/(2*$S$5)+$S$4)
=H17-I17-J17	=H16	=K17*$S$3	=L17*$S$4	=IF(F17="D",D17,-D17)	=K17-M17	=(K17*$S$4-(A17-A16)/(2*$S$5)*M16-J16)/((A17-A16)/(2*$S$5)+$S$4)
=H18-I18-J18	=H17	=K18*$S$3	=L18*$S$4	=IF(F18="D",D18,-D18)	=K18-M18	=(K18*$S$4-(A18-A17)/(2*$S$5)*M17-J17)/((A18-A17)/(2*$S$5)+$S$4)
=H19-I19-J19	=H18	=K19*$S$3	=L19*$S$4	=IF(F19="D",D19,-D19)	=K19-M19	=(K19*$S$4-(A19-A18)/(2*$S$5)*M18-J18)/((A19-A18)/(2*$S$5)+$S$4)
=H20-I20-J20	=H19	=K20*$S$3	=L20*$S$4	=IF(F20="D",D20,-D20)	=K20-M20	=(K20*$S$4-(A20-A19)/(2*$S$5)*M19-J19)/((A20-A19)/(2*$S$5)+$S$4)
=H21-I21-J21	=H20	=K21*$S$3	=L21*$S$4	=IF(F21="D",D21,-D21)	=K21-M21	=(K21*$S$4-(A21-A20)/(2*$S$5)*M20-J20)/((A21-A20)/(2*$S$5)+$S$4)
=H22-I22-J22	=H21	=K22*$S$3	=L22*$S$4	=IF(F22="D",D22,-D22)	=K22-M22	=(K22*$S$4-(A22-A21)/(2*$S$5)*M21-J21)/((A22-A21)/(2*$S$5)+$S$4)
=H23-I23-J23	=H22	=K23*$S$3	=L23*$S$4	=IF(F23="D",D23,-D23)	=K23-M23	=(K23*$S$4-(A23-A22)/(2*$S$5)*M22-J22)/((A23-A22)/(2*$S$5)+$S$4)
=H24-I24-J24	=H23	=K24*$S$3	=L24*$S$4	=IF(F24="D",D24,-D24)	=K24-M24	=(K24*$S$4-(A24-A23)/(2*$S$5)*M23-J23)/((A24-A23)/(2*$S$5)+$S$4)
=H25-I25-J25	=H24	=K25*$S$3	=L25*$S$4	=IF(F25="D",D25,-D25)	=K25-M25	=(K25*$S$4-(A25-A24)/(2*$S$5)*M24-J24)/((A25-A24)/(2*$S$5)+$S$4)
=H26-I26-J26	=H25	=K26*$S$3	=L26*$S$4	=IF(F26="D",D26,-D26)	=K26-M26	=(K26*$S$4-(A26-A25)/(2*$S$5)*M25-J25)/((A26-A25)/(2*$S$5)+$S$4)
=H27-I27-J27	=H26	=K27*$S$3	=L27*$S$4	=IF(F27="D",D27,-D27)	=K27-M27	=(K27*$S$4-(A27-A26)/(2*$S$5)*M26-J26)/((A27-A26)/(2*$S$5)+$S$4)
=H28-I28-J28	=H27	=K28*$S$3	=L28*$S$4	=IF(F28="D",D28,-D28)	=K28-M28	=(K28*$S$4-(A28-A27)/(2*$S$5)*M27-J27)/((A28-A27)/(2*$S$5)+$S$4)
=H29-I29-J29	=H28	=K29*$S$3	=L29*$S$4	=IF(F29="D",D29,-D29)	=K29-M29	=(K29*$S$4-(A29-A28)/(2*$S$5)*M28-J28)/((A29-A28)/(2*$S$5)+$S$4)
=H30-I30-J30	=H29	=K30*$S$3	=L30*$S$4	=IF(F30="D",D30,-D30)	=K30-M30	=(K30*$S$4-(A30-A29)/(2*$S$5)*M29-J29)/((A30-A29)/(2*$S$5)+$S$4)
=H31-I31-J31	=H30	=K31*$S$3	=L31*$S$4	=IF(F31="D",D31,-D31)	=K31-M31	=(K31*$S$4-(A31-A30)/(2*$S$5)*M30-J30)/((A31-A30)/(2*$S$5)+$S$4)
=H32-I32-J32	=H31	=K32*$S$3	=L32*$S$4	=IF(F32="D",D32,-D32)	=K32-M32	=(K32*$S$4-(A32-A31)/(2*$S$5)*M31-J31)/((A32-A31)/(2*$S$5)+$S$4)
=H33-I33-J33	=H32	=K33*$S$3	=L33*$S$4	=IF(F33="D",D33,-D33)	=K33-M33	=(K33*$S$4-(A33-A32)/(2*$S$5)*M32-J32)/((A33-A32)/(2*$S$5)+$S$4)
=H34-I34-J34	=H33	=K34*$S$3	=L34*$S$4	=IF(F34="D",D34,-D34)	=K34-M34	=(K34*$S$4-(A34-A33)/(2*$S$5)*M33-J33)/((A34-A33)/(2*$S$5)+$S$4)
=H35-I35-J35	=H34	=K35*$S$3	=L35*$S$4	=IF(F35="D",D35,-D35)	=K35-M35	=(K35*$S$4-(A35-A34)/(2*$S$5)*M34-J34)/((A35-A34)/(2*$S$5)+$S$4)
=H36-I36-J36	=H35	=K36*$S$3	=L36*$S$4	=IF(F36="D",D36,-D36)	=K36-M36	=(K36*$S$4-(A36-A35)/(2*$S$5)*M35-J35)/((A36-A35)/(2*$S$5)+$S$4)
=H37-I37-J37	=H36	=K37*$S$3	=L37*$S$4	=IF(F37="D",D37,-D37)	=K37-M37	=(K37*$S$4-(A37-A36)/(2*$S$5)*M36-J36)/((A37-A36)/(2*$S$5)+$S$4)
=H38-I38-J38	=H37	=K38*$S$3	=L38*$S$4	=IF(F38="D",D38,-D38)	=K38-M38	=(K38*$S$4-(A38-A37)/(2*$S$5)*M37-J37)/((A38-A37)/(2*$S$5)+$S$4)
=H39-I39-J39	=H38	=K39*$S$3	=L39*$S$4	=IF(F39="D",D39,-D39)	=K39-M39	=(K39*$S$4-(A39-A38)/(2*$S$5)*M38-J38)/((A39-A38)/(2*$S$5)+$S$4)
=H40-I40-J40	=H39	=K40*$S$3	=L40*$S$4	=IF(F40="D",D40,-D40)	=K40-M40	=(K40*$S$4-(A40-A39)/(2*$S$5)*M39-J39)/((A40-A39)/(2*$S$5)+$S$4)
=H41-I41-J41	=H40	=K41*$S$3	=L41*$S$4	=IF(F41="D",D41,-D41)	=K41-M41	=(K41*$S$4-(A41-A40)/(2*$S$5)*M40-J40)/((A41-A40)/(2*$S$5)+$S$4)
=H42-I42-J42	=H41	=K42*$S$3	=L42*$S$4	=IF(F42="D",D42,-D42)	=K42-M42	=(K42*$S$4-(A42-A41)/(2*$S$5)*M41-J41)/((A42-A41)/(2*$S$5)+$S$4)
=H43-I43-J43	=H42	=K43*$S$3	=L43*$S$4	=IF(F43="D",D43,-D43)	=K43-M43	=(K43*$S$4-(A43-A42)/(2*$S$5)*M42-J42)/((A43-A42)/(2*$S$5)+$S$4)
=H44-I44-J44	=H43	=K44*$S$3	=L44*$S$4	=IF(F44="D",D44,-D44)	=K44-M44	=(K44*$S$4-(A44-A43)/(2*$S$5)*M43-J43)/((A44-A43)/(2*$S$5)+$S$4)
=H45-I45-J45	=H44	=K45*$S$3	=L45*$S$4	=IF(F45="D",D45,-D45)	=K45-M45	=(K45*$S$4-(A45-A44)/(2*$S$5)*M44-J44)/((A45-A44)/(2*$S$5)+$S$4)
=H46-I46-J46	=H45	=K46*$S$3	=L46*$S$4	=IF(F46="D",D46,-D46)	=K46-M46	=(K46*$S$4-(A46-A45)/(2*$S$5)*M45-J45)/((A46-A45)/(2*$S$5)+$S$4)
=H47-I47-J47	=H46	=K47*$S$3	=L47*$S$4	=IF(F47="D",D47,-D47)	=K47-M47	=(K47*$S$4-(A47-A46)/(2*$S$5)*M46-J46)/((A47-A46)/(2*$S$5)+$S$4)
=H48-I48-J48	=H47	=K48*$S$3	=L48*$S$4	=IF(F48="D",D48,-D48)	=K48-M48	=(K48*$S$4-(A48-A47)/(2*$S$5)*M47-J47)/((A48-A47)/(2*$S$5)+$S$4)
=H49-I49-J49	=H48	=K49*$S$3	=L49*$S$4	=IF(F49="D",D49,-D49)	=K49-M49	=(K49*$S$4-(A49-A48)/(2*$S$5)*M48-J48)/((A49-A48)/(2*$S$5)+$S$4)
=H50-I50-J50	=H49	=K50*$S$3	=L50*$S$4	=IF(F50="D",D50,-D50)	=K50-M50	=(K50*$S$4-(A50-A49)/(2*$S$5)*M49-J49)/((A50-A49)/(2*$S$5)+$S$4)
=H51-I51-J51	=H50	=K51*$S$3	=L51*$S$4	=IF(F51="D",D51,-D51)	=K51-M51	=(K51*$S$4-(A51-A50)/(2*$S$5)*M50-J50)/((A51-A50)/(2*$S$5)+$S$4)
=H52-I52-J52	=H51	=K52*$S$3	=L52*$S$4	=IF(F52="D",D52,-D52)	=K52-M52	=(K52*$S$4-(A52-A51)/(2*$S$5)*M51-J51)/((A52-A51)/(2*$S$5)+$S$4)
=H53-I53-J53	=H52	=K53*$S$3	=L53*$S$4	=IF(F53="D",D53,-D53)	=K53-M53	=(K53*$S$4-(A53-A52)/(2*$S$5)*M52-J52)/((A53-A52)/(2*$S$5)+$S$4)
=H54-I54-J54	=H53	=K54*$S$3	=L54*$S$4	=IF(F54="D",D54,-D54)	=K54-M54	=(K54*$S$4-(A54-A53)/(2*$S$5)*M53-J53)/((A54-A53)/(2*$S$5)+$S$4)
=H55-I55-J55	=H54	=K55*$S$3	=L55*$S$4	=IF(F55="D",D55,-D55)	=K55-M55	=(K55*$S$4-(A55-A54)/(2*$S$5)*M54-J54)/((A55-A54)/(2*$S$5)+$S$4)
=H56-I56-J56	=H55	=K56*$S$3	=L56*$S$4	=IF(F56="D",D56,-D56)	=K56-M56	=(K56*$S$4-(A56-A55)/(2*$S$5)*M55-J55)/((A56-A55)/(2*$S$5)+$S$4)
=H57-I57-J57	=H56	=K57*$S$3	=L57*$S$4	=IF(F57="D",D57,-D57)	=K57-M57	=(K57*$S$4-(A57-A56)/(2*$S$5)*M56-J56)/((A57-A56)/(2*$S$5)+$S$4)
=H58-I58-J58	=H57	=K58*$S$3	=L58*$S$4	=IF(F58="D",D58,-D58)	=K58-M58	=(K58*$S$4-(A58-A57)/(2*$S$5)*M57-J57)/((A58-A57)/(2*$S$5)+$S$4)
=H59-I59-J59	=H58	=K59*$S$3	=L59*$S$4	=IF(F59="D",D59,-D59)	=K59-M59	=(K59*$S$4-(A59-A58)/(2*$S$5)*M58-J58)/((A59-A58)/(2*$S$5)+$S$4)
=H60-I60-J60	=H59	=K60*$S$3	=L60*$S$4	=IF(F60="D",D60,-D60)	=K60-M60	=(K60*$S$4-(A60-A59)/(2*$S$5)*M59-J59)/((A60-A59)/(2*$S$5)+$S$4)
=H61-I61-J61	=H60	=K61*$S$3	=L61*$S$4	=IF(F61="D",D61,-D61)	=K61-M61	=(K61*$S$4-(A61-A60)/(2*$S$5)*M60-J60)/((A61-A60)/(2*$S$5)+$S$4)
=H62-I62-J62	=H61	=K62*$S$3	=L62*$S$4	=IF(F62="D",D62,-D62)	=K62-M62	=(K62*$S$4-(A62-A61)/(2*$S$5)*M61-J61)/((A62-A61)/(2*$S$5)+$S$4)
=H63-I63-J63	=H62	=K63*$S$3	=L63*$S$4	=IF(F63="D",D63,-D63)	=K63-M63	=(K63*$S$4-(A63-A62)/(2*$S$5)*M62-J62)/((A63-A62)/(2*$S$5)+$S$4)
=H64-I64-J64	=H63	=K64*$S$3	=L64*$S$4	=IF(F64="D",D64,-D64)	=K64-M64	=(K64*$S$4-(A64-A63)/(2*$S$5)*M63-J63)/((A64-A63)/(2*$S$5)+$S$4)
=H65-I65-J65	=H64	=K65*$S$3	=L65*$S$4	=IF(F65="D",D65,-D65)	=K65-M65	=(K65*$S$4-(A65-A64)/(2*$S$5)*M64-J64)/((A65-A64)/(2*$S$5)+$S$4)

Solver		
Dif.	Weight	Objective
=ABS(G4-E4)	=ABS((A4-A5)*N4)	**=SUM(O:O)**
=ABS(G5-E5)	=ABS((A5-A6)*N5)	
=ABS(G6-E6)	=ABS((A6-A7)*N6)	
=ABS(G7-E7)	=ABS((A7-A8)*N7)	
=ABS(G8-E8)	=ABS((A8-A9)*N8)	
=ABS(G9-E9)	=ABS((A9-A10)*N9)	
=ABS(G10-E10)	=ABS((A10-A11)*N10)	
=ABS(G11-E11)	=ABS((A11-A12)*N11)	
=ABS(G12-E12)	=ABS((A12-A13)*N12)	
=ABS(G13-E13)	=ABS((A13-A14)*N13)	
=ABS(G14-E14)	=ABS((A14-A15)*N14)	
=ABS(G15-E15)	=ABS((A15-A16)*N15)	
=ABS(G16-E16)	=ABS((A16-A17)*N16)	
=ABS(G17-E17)	=ABS((A17-A18)*N17)	
=ABS(G18-E18)	=ABS((A18-A19)*N18)	
=ABS(G19-E19)	=ABS((A19-A20)*N19)	
=ABS(G20-E20)	=ABS((A20-A21)*N20)	
=ABS(G21-E21)	=ABS((A21-A22)*N21)	
=ABS(G22-E22)	=ABS((A22-A23)*N22)	
=ABS(G23-E23)	=ABS((A23-A24)*N23)	
=ABS(G24-E24)	=ABS((A24-A25)*N24)	
=ABS(G25-E25)	=ABS((A25-A26)*N25)	
=ABS(G26-E26)	=ABS((A26-A27)*N26)	
=ABS(G27-E27)	=ABS((A27-A28)*N27)	
=ABS(G28-E28)	=ABS((A28-A29)*N28)	
=ABS(G29-E29)	=ABS((A29-A30)*N29)	
=ABS(G30-E30)	=ABS((A30-A31)*N30)	
=ABS(G31-E31)	=ABS((A31-A32)*N31)	
=ABS(G32-E32)	=ABS((A32-A33)*N32)	
=ABS(G33-E33)	=ABS((A33-A34)*N33)	
=ABS(G34-E34)	=ABS((A34-A35)*N34)	
=ABS(G35-E35)	=ABS((A35-A36)*N35)	
=ABS(G36-E36)	=ABS((A36-A37)*N36)	
=ABS(G37-E37)	=ABS((A37-A38)*N37)	
=ABS(G38-E38)	=ABS((A38-A39)*N38)	
=ABS(G39-E39)	=ABS((A39-A40)*N39)	
=ABS(G40-E40)	=ABS((A40-A41)*N40)	
=ABS(G41-E41)	=ABS((A41-A42)*N41)	
=ABS(G42-E42)	=ABS((A42-A43)*N42)	
=ABS(G43-E43)	=ABS((A43-A44)*N43)	
=ABS(G44-E44)	=ABS((A44-A45)*N44)	
=ABS(G45-E45)	=ABS((A45-A46)*N45)	
=ABS(G46-E46)	=ABS((A46-A47)*N46)	
=ABS(G47-E47)	=ABS((A47-A48)*N47)	
=ABS(G48-E48)	=ABS((A48-A49)*N48)	
=ABS(G49-E49)	=ABS((A49-A50)*N49)	
=ABS(G50-E50)	=ABS((A50-A51)*N50)	
=ABS(G51-E51)	=ABS((A51-A52)*N51)	
=ABS(G52-E52)	=ABS((A52-A53)*N52)	
=ABS(G53-E53)	=ABS((A53-A54)*N53)	
=ABS(G54-E54)	=ABS((A54-A55)*N54)	
=ABS(G55-E55)	=ABS((A55-A56)*N55)	
=ABS(G56-E56)	=ABS((A56-A57)*N56)	
=ABS(G57-E57)	=ABS((A57-A58)*N57)	
=ABS(G58-E58)	=ABS((A58-A59)*N58)	
=ABS(G59-E59)	=ABS((A59-A60)*N59)	
=ABS(G60-E60)	=ABS((A60-A61)*N60)	
=ABS(G61-E61)	=ABS((A61-A62)*N61)	
=ABS(G62-E62)	=ABS((A62-A63)*N62)	
=ABS(G63-E63)	=ABS((A63-A64)*N63)	
=ABS(G64-E64)	=ABS((A64-A65)*N64)	
=ABS(G65-E65)	=ABS((A65-A66)*N65)	

Circuit Elements	
R_1	0.0023778569498130
R_2	0.0019035949687408
C_1	18174.179783859

Characterize equivalent circuit parameters by minimizing objective function using GRG nonlinear solver

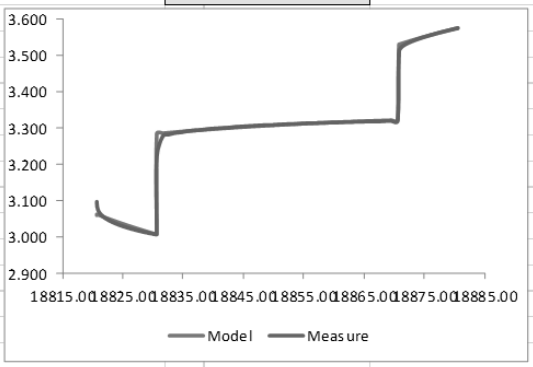

Appendix G – Model Validation

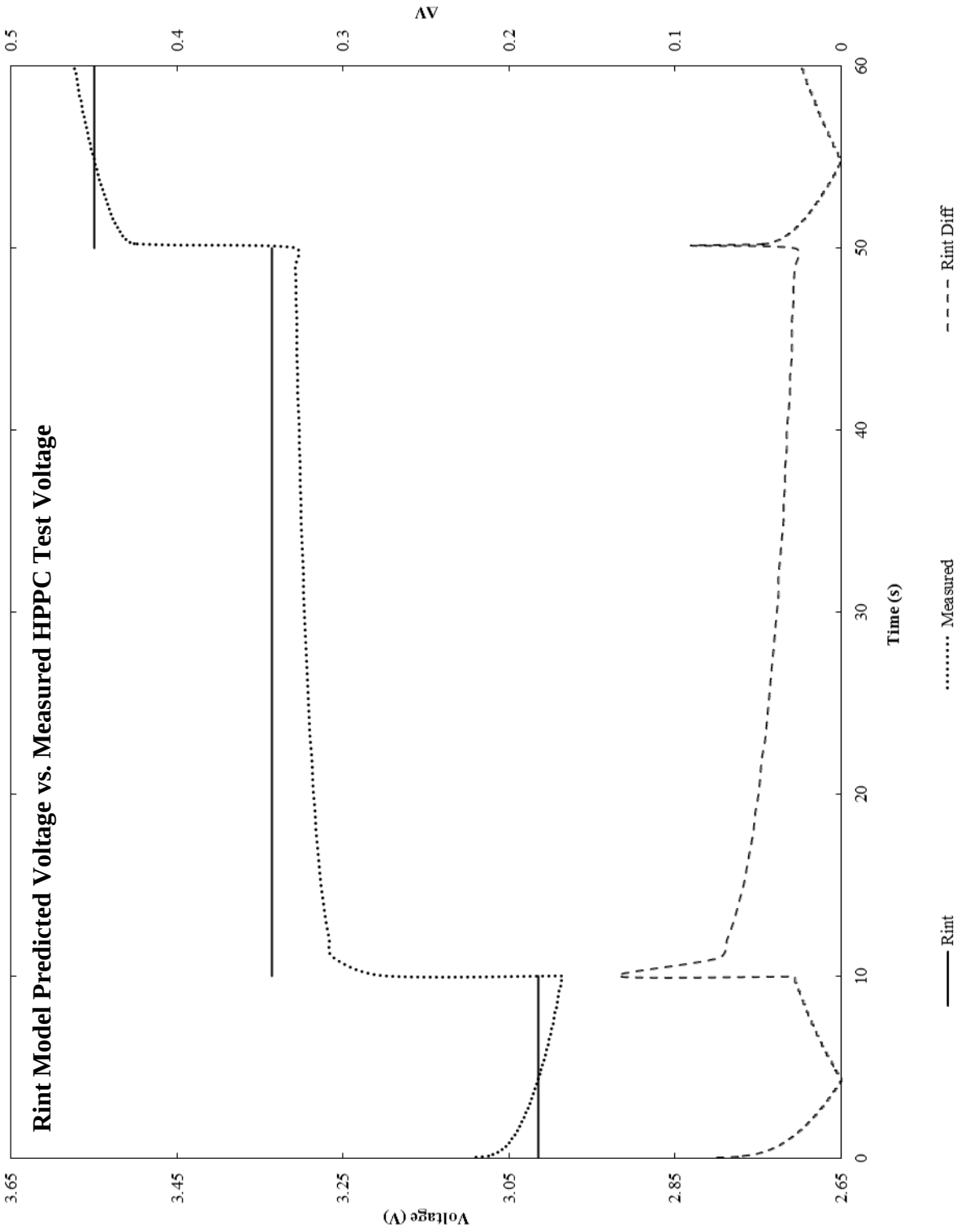

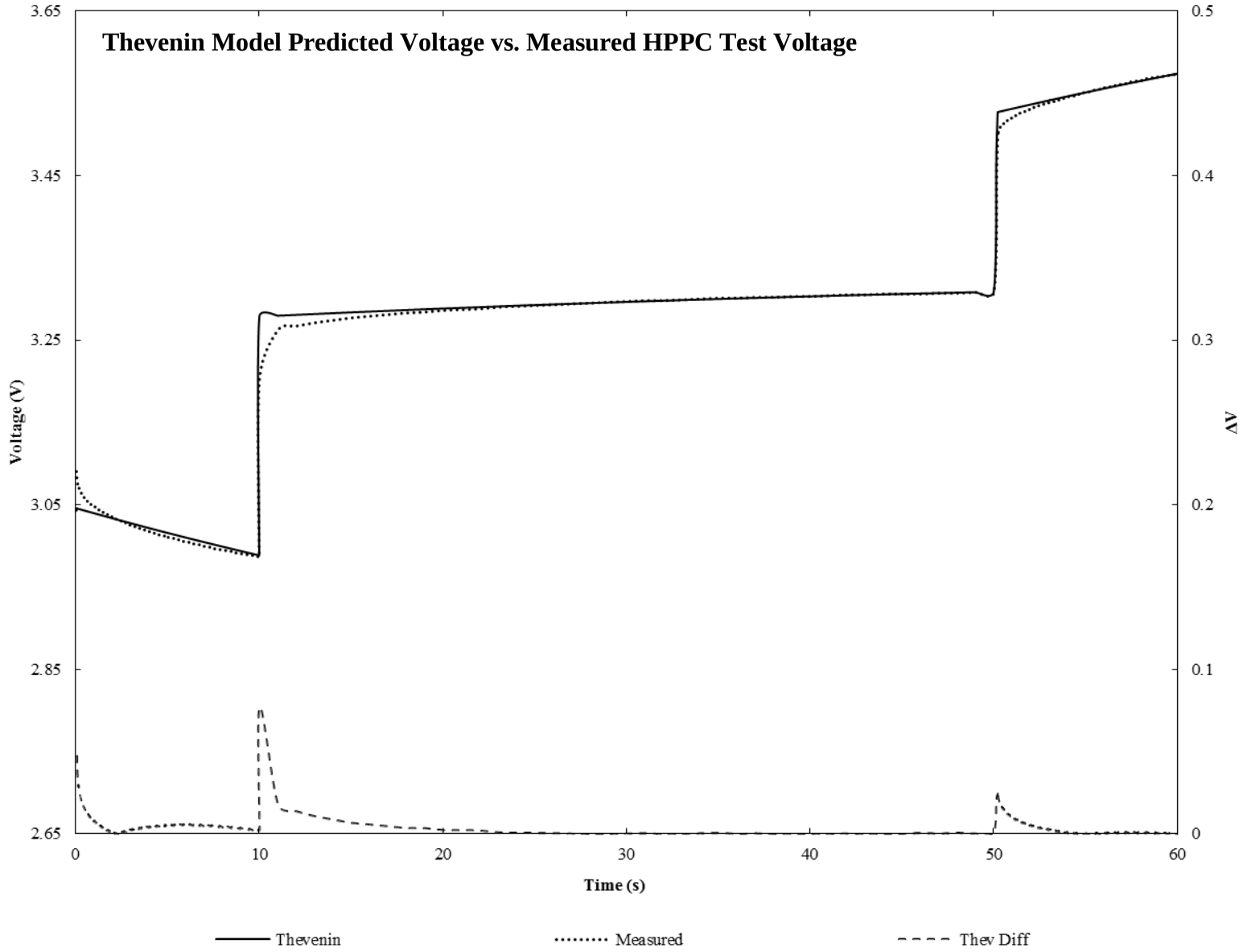
Thevenin Model Predicted Voltage vs. Measured HPPC Test Voltage
Voltage (V)
ΔV
Time (s)
3.65
3.45
3.25
3.05
2.85
2.65
0.5
0.4
0.3
0.2
0.1
0
0
10
20
30
40
50
60
Thevenin
Measured
Thev Diff

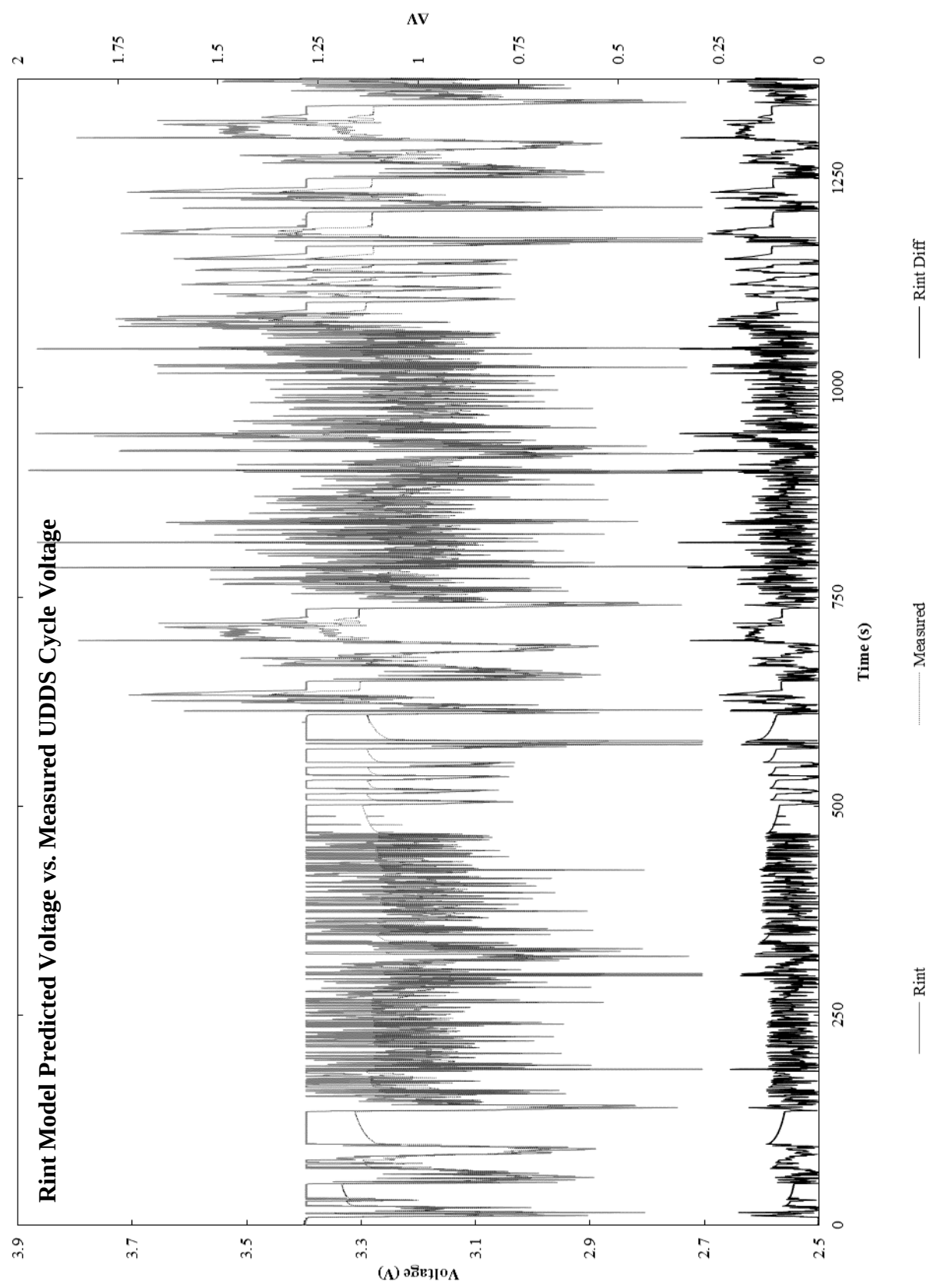
Rint Model Predicted Voltage vs. Measured UDDS Cycle Voltage
Voltage (V)
ΔV
Time (s)
Rint
Measured
Rint Diff
3.9
3.7
3.5
3.3
3.1
2.9
2.7
2.5
2
1.75
1.5
1.25
1
0.75
0.5
0.25
0
0
250
500
750
1000
1250

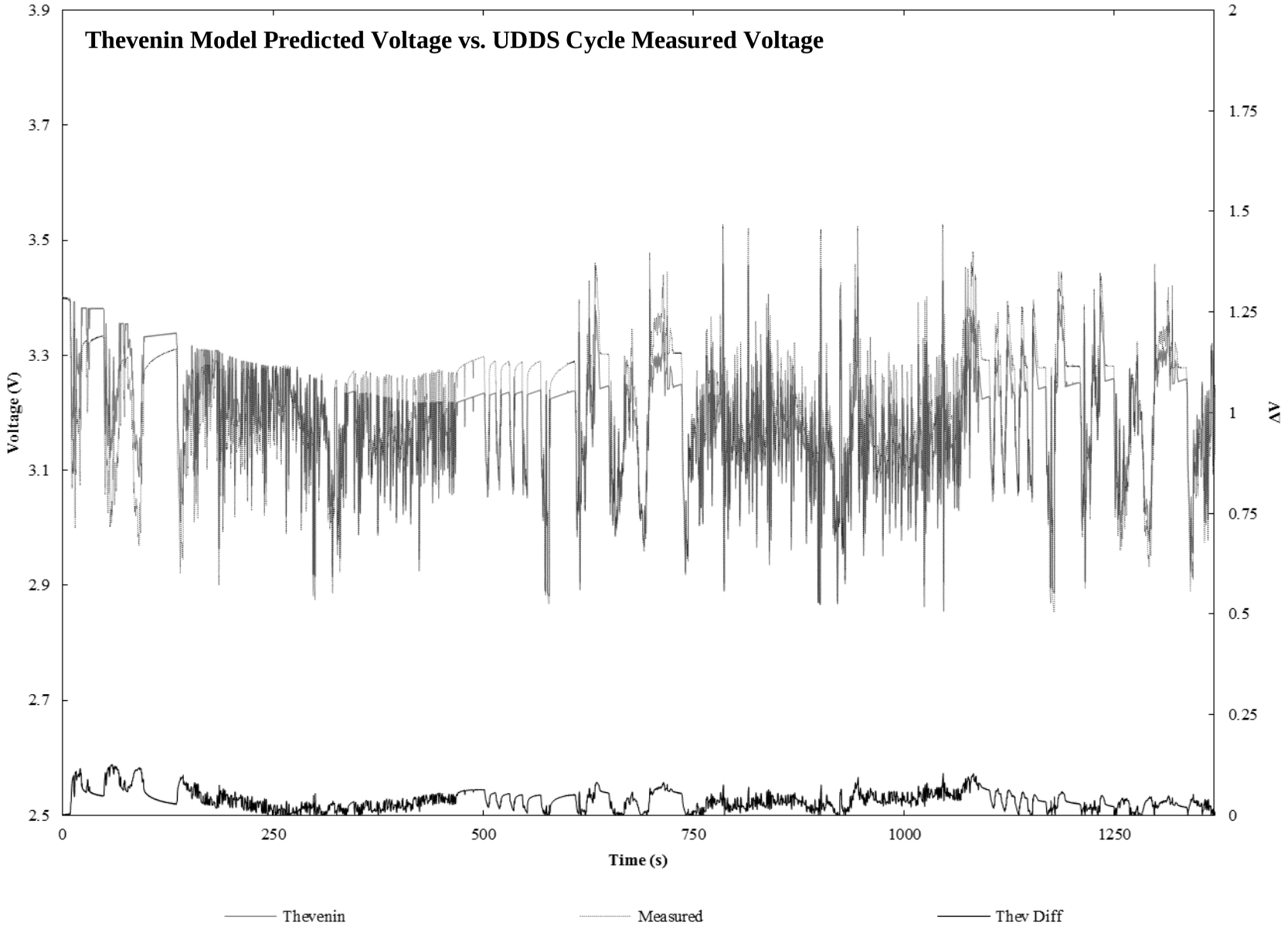
Thevenin Model Predicted Voltage vs. UDDS Cycle Measured Voltage
Voltage (V)
ΔV
Time (s)
3.9
3.7
3.5
3.3
3.1
2.9
2.7
2.5
2
1.75
1.5
1.25
1
0.75
0.5
0.25
0
0
250
500
750
1000
1250
Thevenin
Measured
Thev Diff

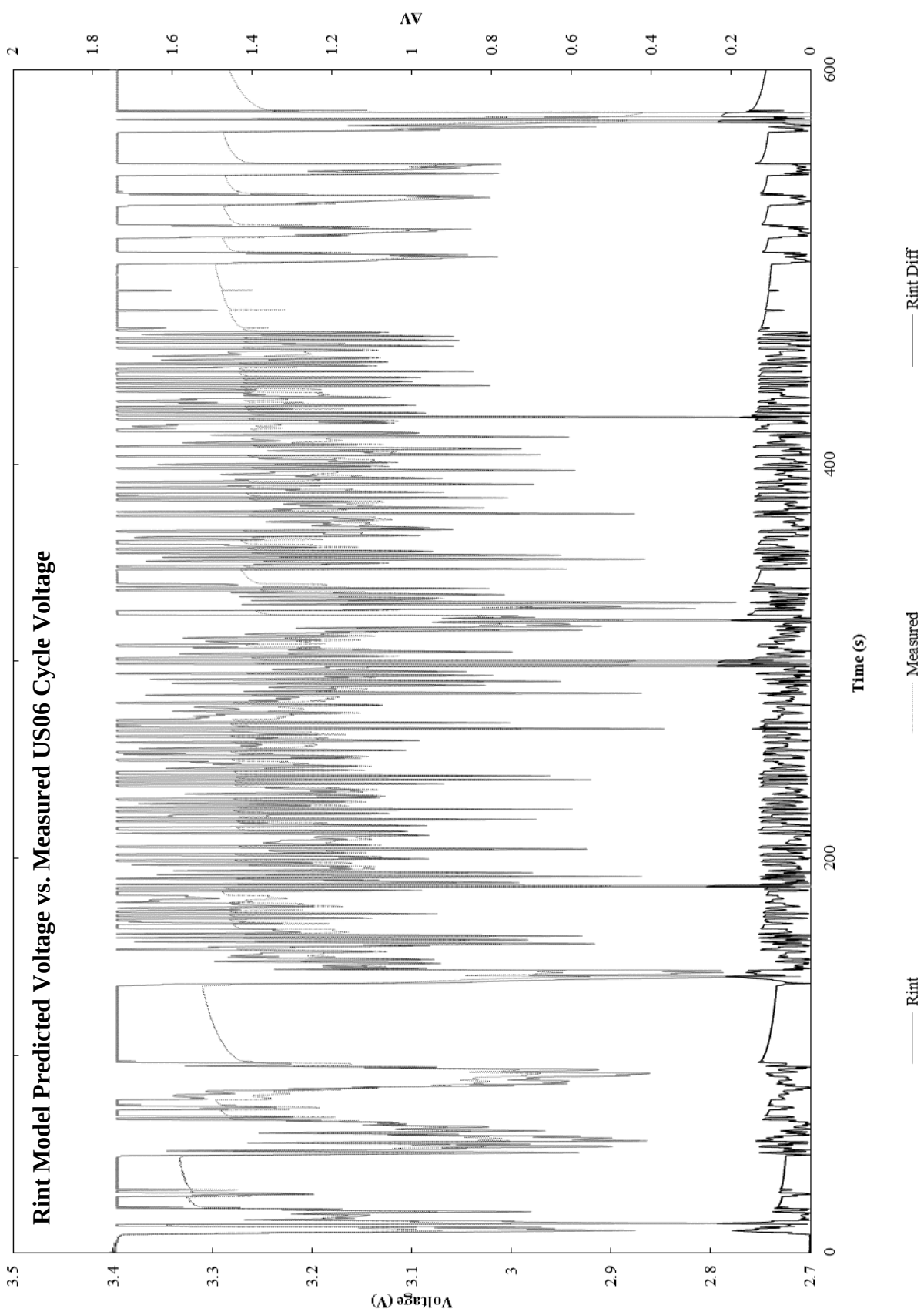
Rint Model Predicted Voltage vs. Measured US06 Cycle Voltage
Voltage (V)
ΔV
Time (s)
Rint
Measured
Rint Diff
3.5
3.4
3.3
3.2
3.1
3
2.9
2.8
2.7
2
1.8
1.6
1.4
1.2
1
0.8
0.6
0.4
0.2
0
0
200
400
600

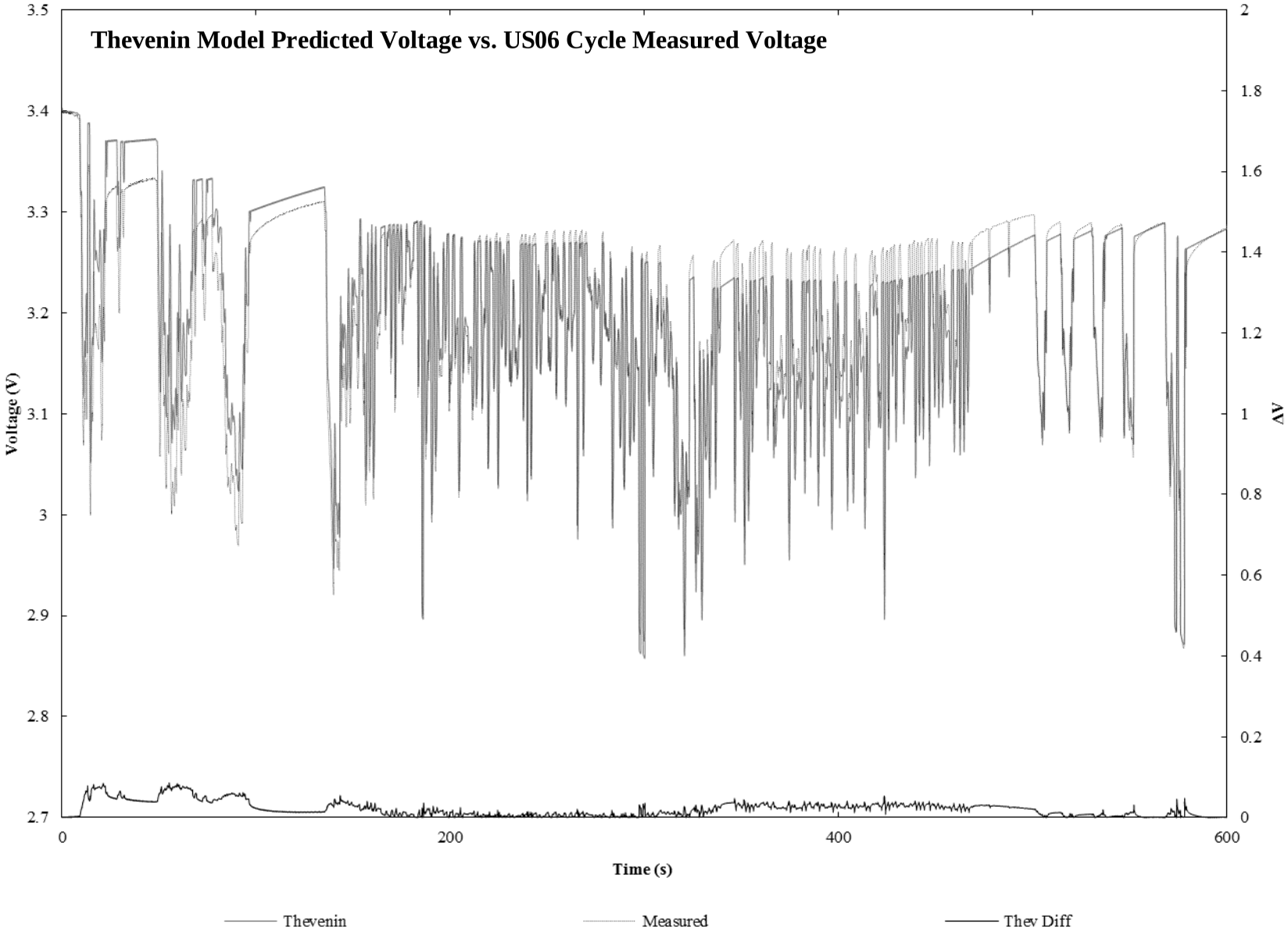
Thevenin Model Predicted Voltage vs. US06 Cycle Measured Voltage
Voltage (V)
ΔV
Time (s)
3.5
3.4
3.3
3.2
3.1
3
2.9
2.8
2.7
2
1.8
1.6
1.4
1.2
1
0.8
0.6
0.4
0.2
0
0
200
400
600
Thevenin
Measured
Thev Diff

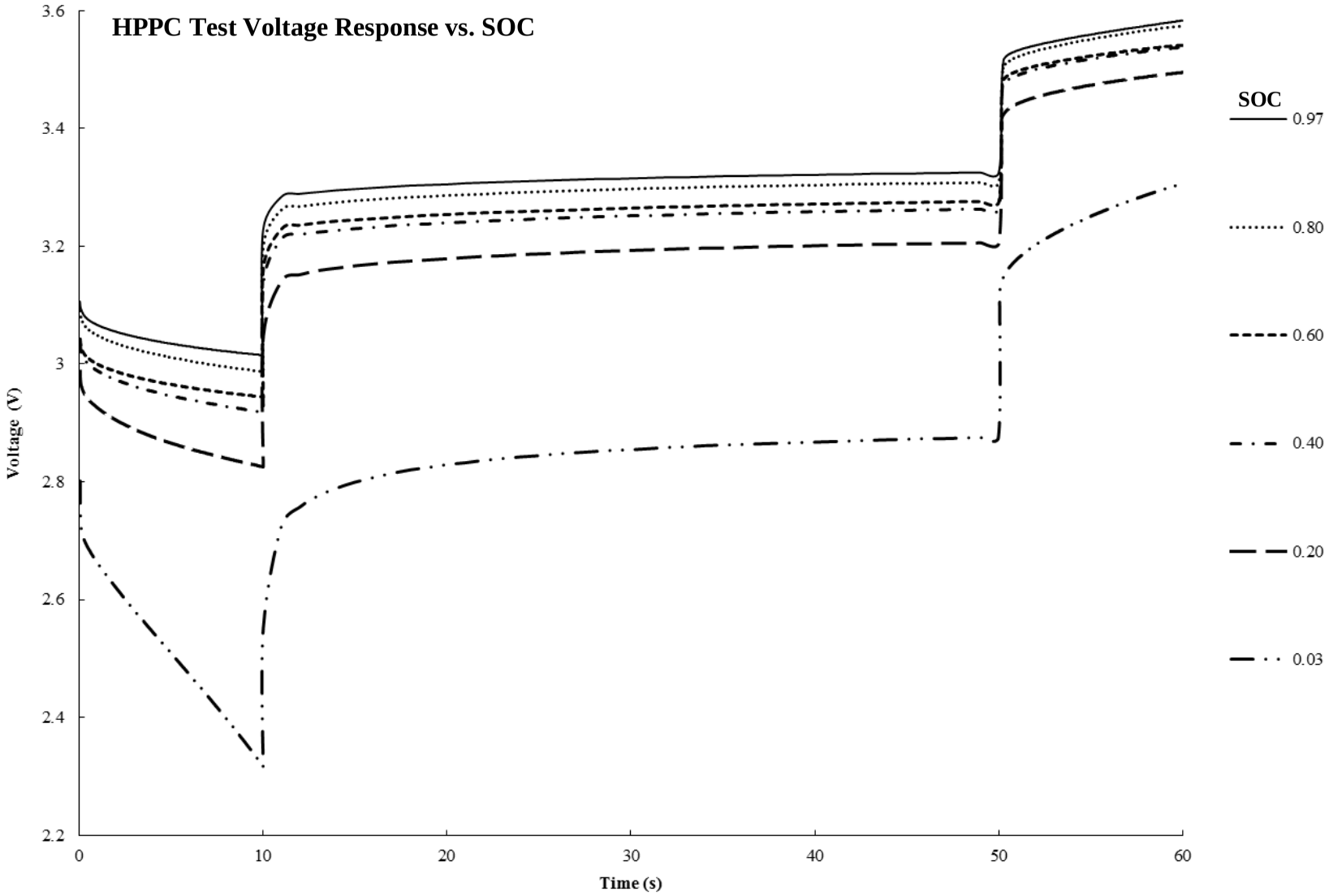
HPPC Test Voltage Response vs. SOC
Voltage (V)
Time (s)
SOC
0.97
0.80
0.60
0.40
0.20
0.03

Appendix H – Related Contributions

Comparison of Equivalent Circuit Model Parameters Derived from AC and DC Sources
64th Canadian Chemical Engineering Conference – October 22, 2014
William Scott

Equivalent Circuit Model (ECM) parameters can be derived through two independent methods, AC and DC current. Direct current, often by Hybrid Pulse Power Characterization (HPPC) test, is often cited by industry. Alternating current, often by Electrochemical Impedance Spectrography (EIS), is the preferred method for academia. This presentation discussed the shortcomings and assumptions of both techniques [101].

Thermal Behavior of Two Commercial Li-ion Batteries for Plug-in Hybrid Electric Vehicles
SAE World Congress – April 9, 2014
William Scott

Detailed thermal modeling of Li-ion batteries is time and resource intensive. However, it is possible to accurately estimate the temperature of pouch cells with heat conductive aluminum casing by a simple linear regression model. This presentation details the accuracy of a regression based modeling approach of two independent lithium-ion batteries within a test rig enclosure simulating the plug-in hybrid vehicle operating conditions [112].

Internal Resistance Optimization Utilizing "Just in Time" Control
SAE International – April 14, 2014
Patrick Ellsworth, William Scott, Michael Fowler, Roydon Fraser, Ben Gaffney, Daniel VanLanen

Inspection of cell internal resistance (Rint) derived by the hybrid pulse power characterization (HPPC) tests indicates that Rint is a function of relative capacity (state of charge, or SOC), thus some SOC ranges are more efficient than others. Therefore energy losses can be minimized by placing charge sustaining operation in a more efficient SOC range. This creates three operational stages; the initial charge depleting stage to an efficient SOC, a charge sustaining stage until a recharge station is within reach, and a final charge depleting stage until arrival.

When coupled with a known drive distance, this three segment Internal Resistance Based (IRB) control strategy increases the extended range electric vehicle (EREV) net battery efficiency from 96.8 to 97.3 % with an associated 14 % decrease in energy losses across the urban domestic drive schedule. Indirect benefits include an increased active SOC range, decreased urban emissions, and decreased waste heat generation, meeting the goals of Advanced Vehicle Technology Competitions [113].

Thermal Behavior of Two Commercial Li-Ion Batteries for Plug-in Hybrid Electric Vehicles
SAE International – April 1, 2014
Ehsan Samadani, Leonardo Gimenez Paez, William Scott, Siamak Farhad, Michael Fowler, Roydon Fraser

In electrified vehicle applications, the heat generated of lithium-ion (Li-ion) cells may significantly affect the vehicle range and state of health (SOH) of the pack. Therefore, a major

design task is creation of a battery thermal management system with suitable control and cooling strategies. To this end, the thermal behavior of Li-ion cells at various temperatures and operating conditions should be quantified. In this paper, two different commercial pouch cells for plug-in hybrid electric vehicles (PHEVs) are studied through comprehensive thermal performance tests.

This study employs a fractional factorial design of experiments to reduce the number of tests required to characterize the behavior of fresh cells while minimizing the effects of ageing. At each test point, the effects of ambient temperature and charge/discharge rate on several types of cell efficiencies and surface heat generation is evaluated. A statistical thermal ramp rate model is suggested which enables fast and accurate determination of cell surface temperature and heat generation where the vehicle is started from cold or warm environments at a range of constant currents over the entire state of charge (SOC) range [114].

Empirical Modeling of Lithium-ion Batteries Based on Electrochemical Impedance Spectroscopy Tests
Electrochemica Acta – April 1, 2015
Ehsan Samadani, Siamak Farhad, William Scott, Mehrdad Mastali, Leonardo Paez, Michael Fowler, Roydon Fraser

An empirical model for commercial lithium-ion batteries is developed based on electrochemical impedance spectroscopy (EIS) tests. An equivalent circuit is established according to EIS test observations at various battery states of charge and temperatures. A Laplace transfer time based model is developed based on the circuit which can predict the battery operating output potential difference in battery electric and plug-in hybrid vehicles at various operating conditions. This model demonstrates up to 6% improvement compared to simple resistance and Thevenin models and is suitable for modeling and on-board controller purposes. Results also show that this model can be used to predict the battery internal resistance obtained from hybrid pulse power characterization (HPPC) tests to within 20 percent, making it suitable for low to medium fidelity powertrain design purposes. In total, this simple battery model can be employed as a real-time model in electrified vehicle battery management systems [58].